



UNIVERSIDAD DE ANTIOQUIA
FACULTAD DE CIENCIAS EXACTAS Y NATURALES
INSTITUTO DE FÍSICA

MAESTRIA EN FÍSICA
2008

Studying Star Formation in Evolving Galaxies Through Simulations of Formation of Large Scale Structure in the Universe

by,
Juan Carlos Muñoz Cuartas

Advisor
Prof. Jorge Ivan Zuluaga

Abstract

We present in this work the results of the study of galaxy formation through the use of cosmological Nbody simulations and semi analytic models. We study the global properties of halos identified in such simulations and propose a modification of the SUBFIND algorithm to identify halo substructure in that simulations. Also we used semi analytic models of galaxy evolution to study galaxy formation in dark matter halos, focusing our effort in to follow the cosmic star formation process. In our results we account the satisfactory implementation of methods in halo identification in Nbody simulations, as well as some indicators of relaxation in such halos. We obtain good results with our algorithm to identify halo substructure and interesting results in our study of star formation in galaxies and the history of the cosmic star formation. We see how our models fit the observational data for $z < 2$, but some considerable discrepancies are found for $z > 2$, part of this discrepancies could be associated with the quality and reliability of observational data for high redshift. Also we found strong dependency of the global star formation on the resolution of the simulations we used to study such process.

Acknowledgements

I have to give thanks a lot of people. All they were related in one or other way with the development of this work. Firstly I have to give thanks to my friend and adviser, porf. Jorge Zuluaga, who allowed me to work in this project considering my way of work, facilitating computational and financial resources for my best work. Also I have to give thanks to the professors of the program of master of physics in the institute by your patience and collaboration in my academic difficulties. I have to give thanks to the evaluators of this work, Prof. Nelson Vera Villamizar and Luis Alberto Sanchez, who patiently collaborated with the evaluation of this work in a record time, and whose comments were fruitful in the improving of the text we present here. Finally I have to give thanks to Jaime Forero at AIP for his comments on this text and his help in the solution of many questions that appeared during the development of this work. Also I have to give thanks to Carlos Vera, who worked with us in different aspects of this project and whose comments and contributions were very important.

Also I have to give thanks to the Facultad de Ciencias Exactas y Naturales, Rectoria, Vicerrectoria General, Group of Computational Physics and Astrophysics and the Regional Center for Simulation and Advanced Computing (CRESCA), all of them in the University of Antioquia (Colombia). The Institute for Computational Cosmology at the University of Durham (UK), and to the International Astronomical Union. All of them gave economical support for some of the participations in international meetings and conferences I attend during the development of this work and the allocation of the best computational resources in the city (or the country!) for the development of this work. Finally, I devote this work to my wife Soneida, who attended all my suffering, by tolerate many long nights of keyboard noise, and by tolerate all my anger along all this time!!!

Contents

1	Introduction	11
1.1	Galaxies in an Evolving Universe	12
1.1.1	First stages of galaxy formation	12
1.1.2	Non-linear collapse and formation of structure	14
1.2	Observations of the Deep Universe	16
1.2.1	WMAP	17
1.2.2	2DF Galaxy Redshift Survey	17
1.2.3	Two Micron All-Sky Survey (2MASS)	18
1.2.4	Sloan Digital Sky Survey (SDSS)	19
1.3	Galaxy Formation	20
2	Theoretical Framework	23
2.1	The Concordance Λ CDM Cosmological Model	23
2.1.1	The Fluid Equation	24
2.1.2	Cosmological Parameters	25
2.1.3	Solution to Friedman's Equations and the Evolution of the Universe	26
2.2	The General Framework for Structure Formation	27
2.3	The Zel'dovich Approximation	29
3	Cosmological Nbody Simulations ...	31
3.1	Description to the Sample	31
3.1.1	Cosmological Initial Conditions	33
3.2	Halo Identification	35
3.3	Halo Substructure	37
3.4	The Method	38
3.4.1	The method for halo identification	39
3.4.2	Results	40
3.5	Physical and Statistical Properties of Halos	42
3.5.1	Density contrast	44
3.5.2	Correlation functions and bias factor	48
3.5.3	Spin Parameter	50

3.5.4	Halo Mass Function	56
3.6	Details of the Code	59
3.7	Conclusions	60
4	Star Formation and Semi Analytic Models ...	65
4.1	Merger Trees	66
4.2	Semi analytic model of galaxy formation	67
4.2.1	Hierarchical Distribution of Galaxies in Halos	67
4.2.2	Baryonic Mass Allocation	69
4.2.3	Radiative Cooling of Hot Gas	69
4.2.4	Supernovae Feedback	70
4.2.5	Star Formation	71
4.2.6	Galaxy Mergers	71
4.2.7	Photometric Evolution	72
4.2.8	Putting Everything Together	73
4.3	Results of our model	73
4.3.1	Global Evolution of Baryons	73
4.3.2	Cold Gas Mass	74
4.3.3	Cooling Rate	75
4.3.4	Reheated Mass by Supernovae Feedback	76
4.3.5	Hot Gas Mass	77
4.3.6	Stellar Mass	78
4.3.7	Global Star Formation	78
4.3.8	Mergers	86
4.4	Conclusions	89

List of Figures

1.1	Time line evolution of the universe	13
1.2	Time evolution of the resolution of Nbody simulations	14
1.3	Subhalo mass distribution of a high resolution simulation	15
1.4	Snapshot from a simulation of a $100 \text{ Mpc} h^{-1}$	16
1.5	WMAP map polarization map	17
1.6	Power Spectra WMAP3	18
1.7	Galaxy correlation function from the 2DF	19
1.8	Stellar mass evolution in a cosmological-gas dynamics simulation . . .	20
1.9	Tully-Fisher relation from a semi-analytic model.	21
2.1	Numerical Integration of Friedman's equation	27
2.2	Growth function	29
3.1	Snapshot from the simulation SFOF03 at $z=4.95$	32
3.2	Snapshot from a simulation at $z=1.91$	32
3.3	Snapshot from a simulation at $z=0$	33
3.4	Grid operation for computing the potential	36
3.5	Flow chart of binding FOF halo	38
3.6	(a) Distribution of the potential energy of particles in a FOF halo identified in a simulation of 320^3 particles. (b) Projection of the halo itself.	39
3.7	(a) Subhalos identified to grow around the potential wells of the distribution. (b) Survivor halos after the evaluation of binding of particles in every subhalo to the left. In this analysis $N_{min} = 16$	41
3.8	Comparison of halo mass distributions for the simulation using only FOF and including subhalos identified at first level of hierarchy of substructure. Doted diagonal line corresponds to a power law of $\gamma = -2.066$	42
3.9	Distribution of subhalos identified as a function of the number of particles/subhalo for different values of the number of nearest neighbors used to the subhalo identification.	42
3.10	Distributions of density contrast of halos at a sequence of redshifts . .	45
3.11	Distributions of density contrast of halos	47

3.12	Fitting to density distributions	48
3.13	Correlation function for dark matter	49
3.14	Correlation function for halos	50
3.15	Ratio $\xi_{hh}(r)/\xi_{dm}(r)$	51
3.16	Up. Distribution of λ values for the history of a galaxy. Down. Values for λ obtained from the merger tree of one of the halos in the SFOF06 simulation. Points are values for λ at every halo at that z , blue dashed line is the arithmetic mean of these values for that redshift while the straight line marks the $\bar{\lambda} = 0.07$ value.	52
3.17	λ distributions for the three simulations at different redshifts $z=0, 0.43, 1.03, 1.91, 3.16$ and 4.94 counted from upper left to upper right panels	53
3.18	Distribution of spin parameters for halos in the three SFOF simulations for different redshifts	54
3.19	Fit of the distribution to the equation 3.21.	55
3.20	Temporal evolution of the parameters of the distribution of spin parameter for dark matter halos.	55
3.21	Mass distribution for the three simulations at different redshifts $z=0, 0.43, 1.03, 1.91, 3.16$ and 4.94 counted from upper left to upper right panels	57
3.22	Distribution of subhalos identified as a function of the number of particles/subhalo for different values of the number of nearest neighbors used to the subhalo identification.	58
3.23	Fit to a power law function to the mass function.	59
3.24	Flow chart of the GalCos halo identification and properties code.	60
4.1	Merger tree for a halo in a Nbody simulation	68
4.2	Cooling function	70
4.3	Cold gas mass	75
4.4	Cooling rate	76
4.5	Ejected mass by SN feedback	77
4.6	Hot gas mass	78
4.7	Stellar mass	79
4.8	Global star formation history	80
4.9	Resolution effects on the Global star formation history	83
4.10	Resolution effects on the Global star formation history	84
4.11	Resolution effects on the Global star formation history	85
4.12	Resolution effects on the Global star formation history	85
4.13	Frequency of mergers with time	86
4.14	Masses of main and satellite galaxies involved in mergers	87
4.15	Mass ration in galaxy mergers	88
4.16	Star formation bursts at major mergers	88

Chapter 1

Introduction

From the beginning of first civilizations, human thinking about the world has located the men at the centre of the universe. Firsts Greek philosophers were able to “design” conceptually complex models of the universe, in which the Earth, and the humanity are in the center of the universe. This complex models were able to explain some phenomena related with the objects occupying the universe. Because the ancient civilizations were not able to develop sophisticated instruments to do deep astronomical observations, the universe was filled only with the things that the man can see at naked eye, the planets Mercury, Venus, Mars, Jupiter, Saturn, the Moon, the Sun, comets and the fixed Stars.

The ideas about the universe evolved through time, until the Copernican revolution, in which the center of the universe was moved to the Sun. This change reveals a really important fact in the development of the ideas about the universe: **we are not the (or at the) center of the universe**. The Copernican revolution, accomplished by all the knowledge produced in this epoch (Galilean production in physics and astronomy, the Kepler’s work on planetary movement, Newtonian revolution in the understanding of the nature, etc.) change completely our vision of the universe, looking at this like a very complex and system, whose secrets must be revealed.

By 1700 Century William Herschel was able to do the first map of the known universe, the Galaxy, the aggregation of stars at which the Sun belongs. This map, revealed a really surprising result, once again, the Sun, and then ourselves, are at the very center of the galaxy. Although there was no philosophical or religious reasons to think this way, the observational work of Herschel (one of the most important astronomers of the history) show this important conclusion.

Next at the beginning of 1900 century, Jacobus Kaptein develops a more complete survey of the sky, trying to do a more complete map that the one performed by Herschel. At 1922 Kaptein published his results and in very concordance with the results obtained by Herschel. Kaptein’s “universe” had the shape of a spheroid, in which the Sun was located not at the center, but actually very near of this point.

By the same time, Harlow Shapley and Edwin Hubble were working in his projects. Shapley was working in independent measurements of the size of the galaxy, whose results, in considerable disagreement with that obtained by Kaptein, gives the idea about the maximum size of the galaxy. Meanwhile Hubble was working in cataloguing galaxies and studying their proper motions. Until 1923 our universe was only filled with the planets in the Solar System, stars in the galaxy and nebulae, diffuse objects that can be observed and resolved only under the telescope. In 1923 Edwin Hubble gives key observational support to demonstrate that many of the so called nebulae were far away from the border of the galaxy, whose size was estimated by Shapley. Then our universe, once again, as in the Copernico's time was changed, and once again, expanded its horizon far, far away. From then galactic astronomy became an important and recent part of the astrophysics, and from them many scientists have worked out many ideas to explain its properties and evolution.

1.1 Galaxies in an Evolving Universe

1.1.1 First stages of galaxy formation

There are two different ways to study galaxy evolution. One can study the evolution of formed galaxies as individual systems, or at least, under interaction with other systems. Commonly this kind of studies is devoted to see how the dynamics, chemistry and morphology of the galaxy changes in short time intervals, without take into account the precedent history of the galaxy.

On the other side, one can study the origin of galaxies, the stages that happened during their evolution from the first steps of formation until the recent state of neighbor galaxies in the present universe. Both approaches are really interesting, and offer many insights about the general behavior of galaxies in the universe, and their are also complementary. In this work we will be interested in the study of the evolution of galaxies from early instants, that is, we will follow the second approach.

When we study the evolution of the global content of galaxies in the universe, in a large sample of the universe, the evolution of galaxies is strongly coupled to the evolution of the universe itself. As we will see in chapter 2, the universe is a dynamic entity, an expanding “scenario” in which the galaxies form, but the expansion of the universe influences strongly the way in which galaxies form and evolve.

While the universe expands, matter from which galaxies forms experiences the effects of cosmic recession that separates it far away, while gravity tries to hold bound lumps of matter that are locally in a no equilibrium state. In both cases the gravitational collapse and the expansion of the universe play a crucial role during the formation and evolution of galaxies. It is then a strong requirement that to understand the process of formation and evolution of galaxies it is needed to understand

the dynamics of the universe.

Fortunately, nearly 90 years after the first modern complete and self-consistent model of the universe was proposed by Einstein, and after many years of ambiguities about what the exact behavior of the universe was, we can speak about a “concordance” model that fits very well with observations and with other cosmic phenomena. We are speaking about the Λ CDM cosmological model, in which the universe is an expanding entity filled with radiation, baryonic matter, dark matter and an exotic dark energy, and whose geometry is flat.

Once the cosmological model has been proved to be successful (almost by now it is) is needed to prove the behavior of matter on it. The evolution of the universe is strongly coupled to its matter content, and also the evolution of its matter content is strongly dependent of the evolution of the universe itself. Then what one can do is try to study simultaneously both process and see how the system evolves, and use the results to compare with observations in order to verify that our theoretical universe is in agreement with the present universe.

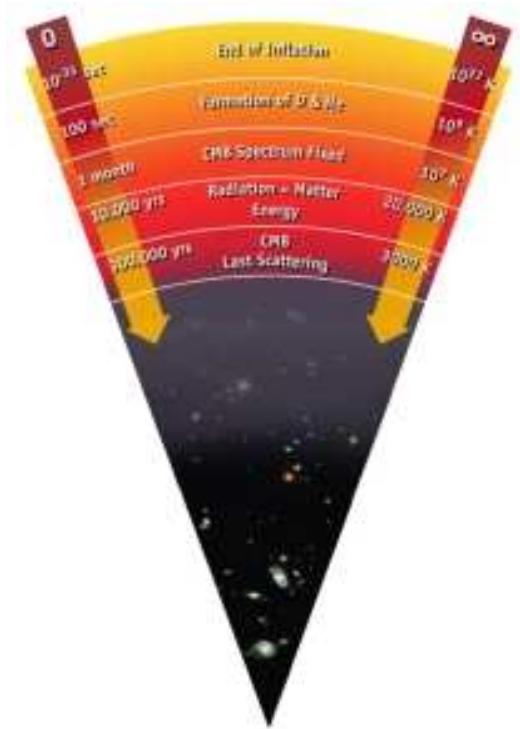


Figure 1.1: Diagram of the time line evolution of the universe

This is a hard work, because it requires a strong investment of physics, astrophysics and observational work, but in some sense, it can be done. In order to do things easy, one can split the problem in two parts, the evolution of the matter in the early the universe, and the evolution of the matter in the universe in the late stages. The

first stage of the evolution of the matter in the universe is more or less well understood. One can start (Avila-Reese 2007) with the description of the behavior of the early universe and the state of the matter within it, one can start then with the hot big bang and the fast expansion of the universe, and next explain the cooling of radiation in matter and then, the cooling of matter and recombination epoch, until finally one can explain the formation of light atoms and the growing of the first dark matter fluctuations. Then, once the first dark matter density fluctuations begin to grow, one can concentrate his attention in to follow the evolution of this process, which can be modelled as a linear collapse process (because the effect of the expansion of the universe is so strong on these stages), that can be followed in an analytic way.

1.1.2 Non-linear collapse and formation of structure

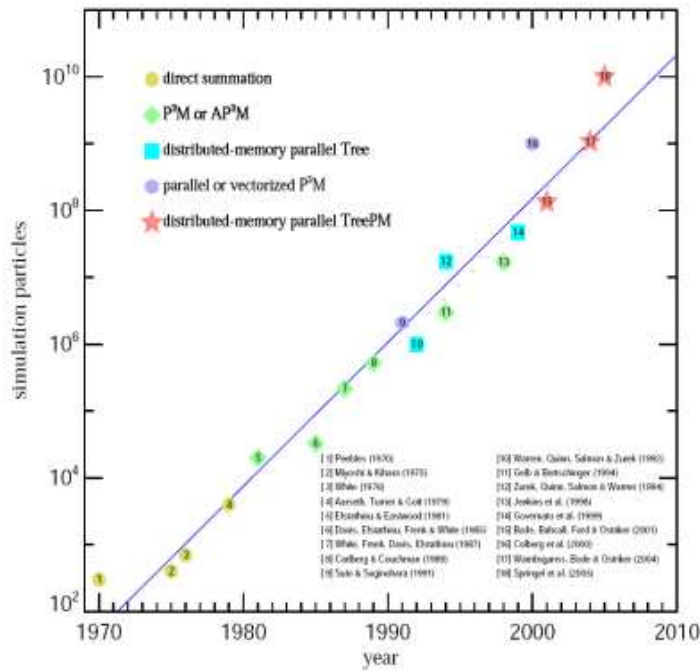


Figure 1.2: Evolution of the increased ability to simulate Nbody systems with higher resolution from first simulations from 1970 to 2004 (Springel et al. 2005)

Once the linear collapse ends, the growing of density fluctuations continues in a non-linear way. It is hard to follow the evolution of the process analytically, then it is simulated starting with appropriated initial conditions. During the last thirty years, simulations of the accretion of matter in well defined structures in the expanding universe has been carried out with relative success.

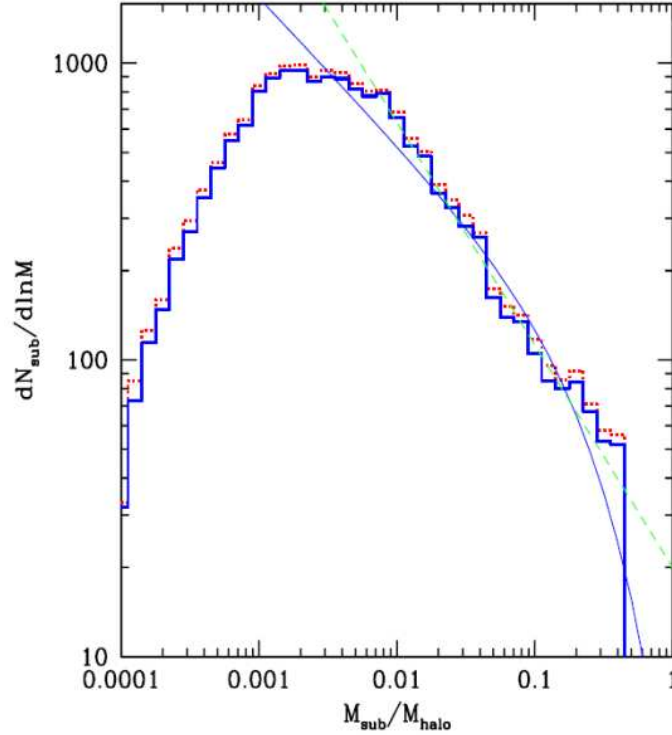


Figure 1.3: Subhalo mass resolution of the 1024^3 particles simulation. (Shaw et al. 2007).

Different theoretical and numerical problems have to be solved in order to obtain these results. On one hand we have to generate the initial conditions for the simulations (Ma & Bertschinger 1995, Sirko 2005). Commonly they are generated from the initial power spectra of galaxy distribution in the early universe, which is not completely known. Another problem widely discussed by several authors (Spergel et al. 2007, Bartolo et al. 2004) is the non-gaussianity of the distribution of the initial density fluctuations, that also must affect the generation of initial conditions. Gaussianity is in principle a consequence of inflation, but still there are authors arguing the possibility to generate a non-Gaussian field for the density perturbations.

One of the most important numerical problems is related to the requirement to have simulations of high enough resolution to follow the evolution of small enough structures until the formation of individual galaxies at low redshifts (Springel et al. 2005, Klypin et al. 1999). This requirement is translated in an increase of memory and computing power. Recently, the simulations has reached a surprising level of resolution. Springel et al. 2005 showed in the Millennium Simulation the results of the increase of the number of particles until 1024^3 particles in a cubic box of side $500 \text{ Mpc} h^{-1}$ and Shaw et al. 2006 achieved a higher resolution simulation of 1024^3 particles in a cubic box of $320 \text{ Mpc} h^{-1}$.

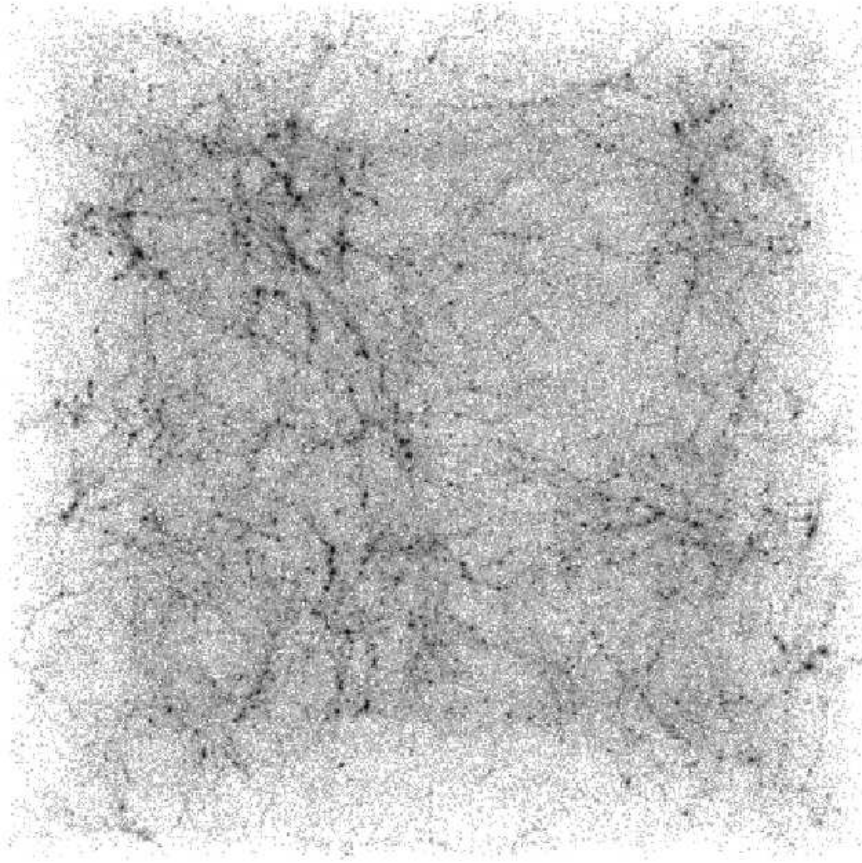


Figure 1.4: Projection of the density field of a Nbody simulation with 170^3 particles in a cubic box of $100\text{Mpc}h^{-1}$

The increase of the resolution in simulations allow us to follow the formation of smaller physical bound structures, such as normal sized and dwarf galaxies, structures that must be identified in simulations to build the complete story of galaxy formation.

1.2 Observations of the Deep Universe

Every theoretical model must be contrasted against observational data that allow us not only to verify the validity of the model, but also to propose other ways in which the model can be modified in order to match the observations. In cosmology and structure formation studies there are several observational projects that offer valuable information about the evolution of the universe and their galaxy content. WMAP, 2DF Galaxy Redshift Survey, the Two Micron All-sky Survey (2MASS), The Sloan Digital Sky Survey (SDSS) are some of the most important projects. In the following sections we present a brief description of these projects and their role

$100\Omega_b h^2$	$\Omega_m h^2$	h	A	τ	n_s	σ_8	Ω_m
2.233	0.1268	0.734	0.801	0.088	0.951	0.744	0.238

Table 1.1: Cosmological parameters for the best fit for the Λ CDM model.(Spergel et al. 2007).

in the study of the history of the universe and galaxy evolution.

1.2.1 WMAP

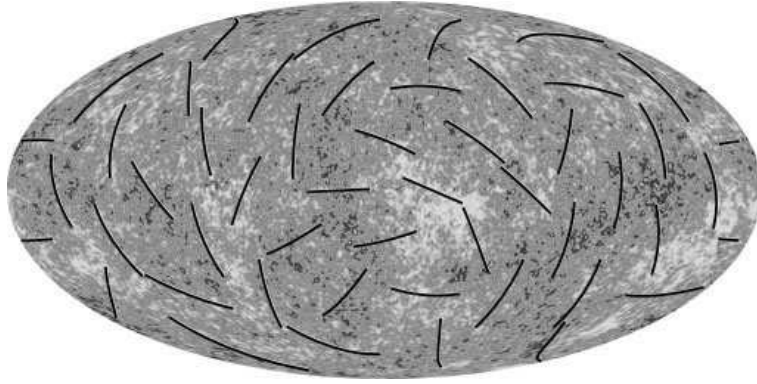


Figure 1.5: WMAP map of the anisotropy of temperature and polarization of the CMB.

The Wilkinson Microwave Anisotropy Probe was launched in June of 2001 as the successor of COBE. The main objective of the mission was to measure at high resolution the anisotropy of the CMB, in order to measure the properties of the density perturbations on the early universe.

Results of the WMAP has become one of the most important observational test of the Λ CDM cosmology. The recent released results of the WMAP, WMAP3 (Spergel et al 2007) has shown other interesting properties of the CMB, such as polarization maps that give us an insight of the formation of the first stars in the very early universe, a process which is able to explain the observed polarization of the CMB. WMAP has measured the high resolution angular spectrum of the radiation field, what has allowed cosmologists to pinpoint with an unprecedented precision the value of the cosmological parameters.

1.2.2 2DF Galaxy Redshift Survey

The 2DF Galaxy Redshift Survey was an effort that covered an area of 1500 square degrees around the North Galactic Pole and South Galactic Pole. Observations were made using pre-studied regions by the APM Galaxy survey with the 3.9mt Anglo

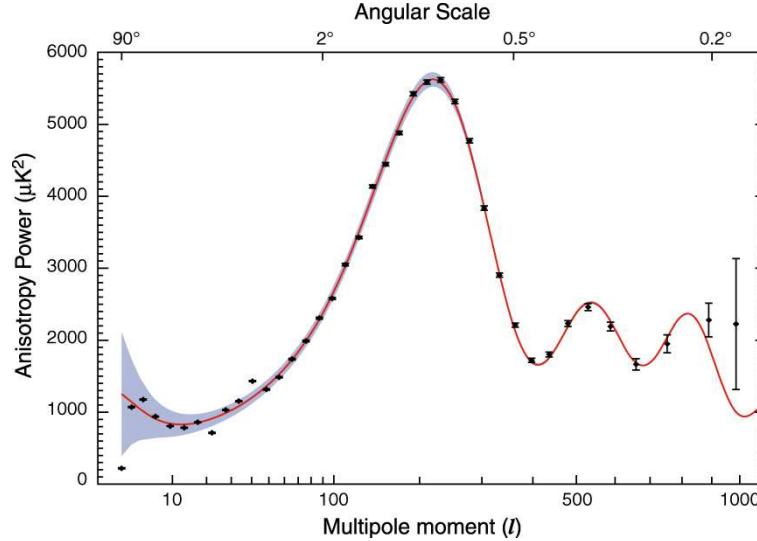


Figure 1.6: Power spectra of the CMB produced in the WMAP3 release. (Spergel et al. 2007).

Australian Telescope and the multispectrometer of optical fiber that allow the simultaneous observation of up to 400 spectra simultaneously. 2DF was one of the first most important galaxy surveys because its results offer spatial information of several extragalactic sources involving the observing and cataloging of objects in a volume of nearly $10^8 \text{Mpc} h^{-1}$.

The survey produced in total observations of 382323 targets including spectra of 245591 objects, the majority of which were galaxies. The limiting magnitude of the observations was approximately 19.5, which is related with a redshift of less than $z=0.3$.

Some of the main goals of this survey were the accurate measurement of the power spectrum of galaxy clustering on scales up to $300 \text{Mpc} h^{-1}$ allowing a precise determination of the mass density in the universe. The observational determination of the galaxy bias, the characterization of the galaxy luminosity function and studies of star formation in galaxies has been also performed with the 2DF results.

1.2.3 Two Micron All-Sky Survey (2MASS)

Although 2MASS is not a large scale survey, it has played an important role in the study of global properties of galaxies in the local universe. 2MASS was a project built from a series of observations of the entire sky from two 1.3m telescopes located at Mt. Hopkins Arizona and CTIO Chile. The project observed the entire sky in infrared, in the bands J($1.25\mu\text{m}$), H($1.65\mu\text{m}$), and K_s($2.7\mu\text{m}$). Their observations allow the detection of many galaxies in the avoidance zone and the study of properties of galaxies at infrared wavebands, in which star formation processes can be observed. This offers a great opportunity to use its data in the study of massive

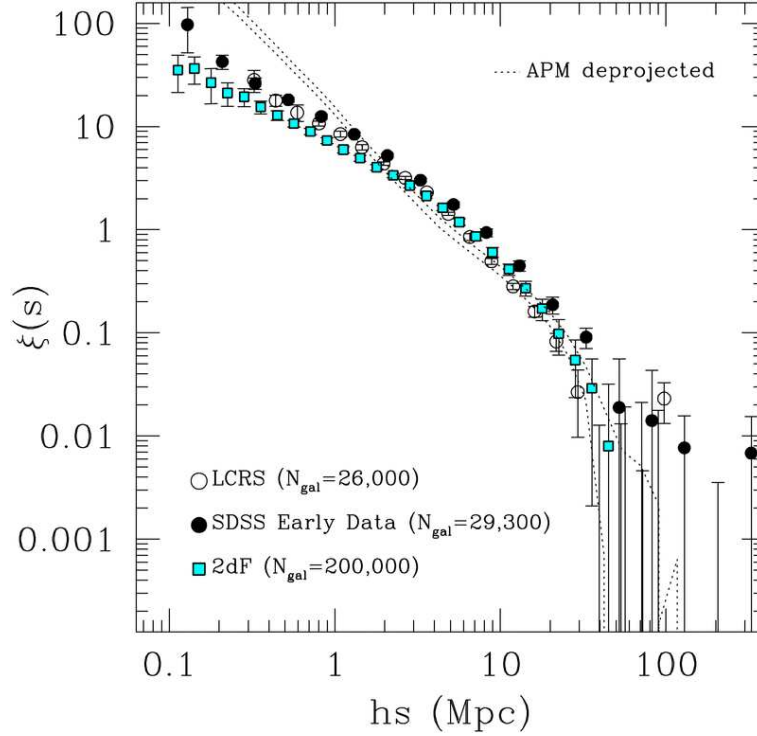


Figure 1.7: Galaxy correlation function produced in the final data release by the 2dF Galaxy Survey.

star formation in galaxies. 2MASS also allows detection of the first brown dwarfs and other stellar populations, which play an important role in the determination of global properties of star formation in galaxies, which play an important role in this work.

1.2.4 Sloan Digital Sky Survey (SDSS)

Finally, but not less important, the Sloan Digital Sky Survey is currently the largest survey of the sky. Started at 2000, the project consists on the observation of the 25% of the sky using the 2.5m telescope at Apache Point, New Mexico. The initial goal was to record observations from 100 million objects and spectra for other 1 million objects.

Observations are made using an array of thirty CCD cameras with 1048×1048 pixels each, and multispectrometer techniques that allow the recollection of 640 spectra at once. Observations are taken in 5 filters, **u**, **g**, **r**, **i** and **z** at 354, 476, 628, 769 and 925 nm respectively

From June 2001 when the first data was released, until June 2007, the SDSS has produced nearly 1,271,680 spectra in a field of observation of 9,583 square degrees, allowing observations of galaxies until redshift $z = 0.4$ and quasars at $z > 5$.

SDSS data has been used to produce interesting results in the study of galaxy correlation function, the bias factor and its dependence with redshift. Most important has been the possibility to study star formation in galaxies and the environmental effects and the AGN activity at different redshifts.

1.3 Galaxy Formation

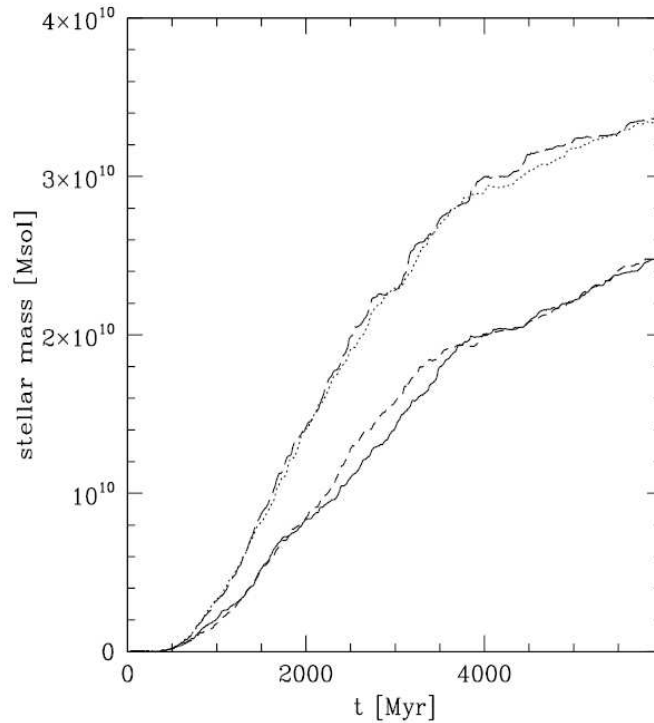


Figure 1.8: Stellar mass evolution in a cosmological hydrodynamical simulation. (Merlin et al. 2007).

Galaxy formation is one of the most challenging problems in astrophysics. A large number of different physical processes must be taken into account in order to describe the evolution of galaxies, some of which are dissipative or non linear, and are not easy to follow in time.

Galaxy formation starts with the collapse of baryonic mass in the potential well of density enhancements of dark matter (Avila-Reese 2007) that are allowed to collapse time before the decoupling. Once the collapse of baryonic matter starts, Jeans unstable hydrogen clouds begin to collapse independently and allow the formation of the first stars in the protogalaxies which will evolve under the effect of the environment through many collision processes. Models of this process has been carried

out by Cole et al. 1994, Merlino & Chiosi 2008, Kang et al. 2005, Domainko et al. 2007, Kauffmann et al. 1999 and others. All of them have used as input results of hydrodynamical simulations or the merger trees of halos as they evolve in nbody simulations, or in realization of the halo mass distribution.

Galaxy evolution has to take in to account the hydrodynamical effects in the evolution of the system, viscosity effects, shock waves, magnetic fields, dynamical heating and so forth. Other physical processes that affect the barionic matter content in the galaxies, like supernova feedback, radiative cooling and heating by UV flux must be also considered. A complete description of the process must also consider the star formation process and the effect of the dynamical evolution of the system, including galaxy collisions, mergers and chemical evolution.

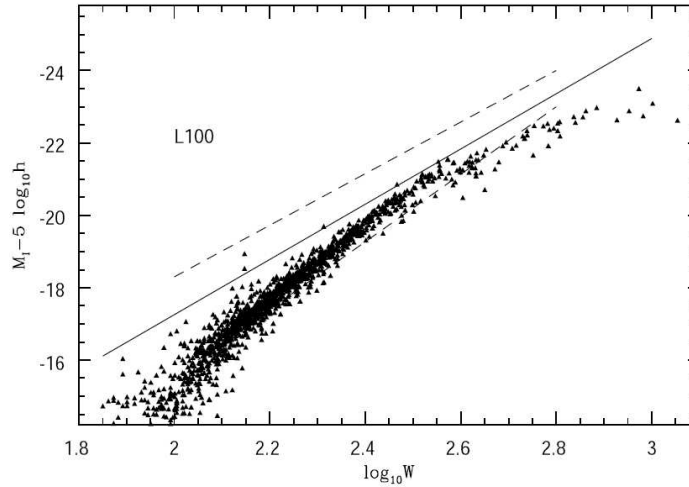


Figure 1.9: Tully-Fisher relation produced using semi-analytic recipes. (Kang et al. 2005).

Early galaxy formation is modeled through two different approaches. The first one is to include gas in the Nbody simulations (Merlin et al. 2007, Yepes et al. 2002, Yepes et al. 1997, Bryan & Norman 1997), and using grid methods or SPH the fluid equations are solved and other physical effects are introduced through approximations. In this way, while the dark matter evolves to form the potential well of the galaxy, baryons evolve to give rise galaxies inside that potential. In a different approach the starting point is the merger tree of the evolution of dark matter halos (Kauffmann et al. 1999, Kang et al. 2005, Nagashima et al. 2008), and using semi-analytical methods to describe approximately the evolution of baryons in the potential well of the dark matter halos. In this case the evolution of baryons will be a function of the potential well of the halo where galaxies form.

Previous works have shown that both methods work well to give approximations in the description of the properties of galaxies in simulations, and although the first

one is the ideal way to study galaxy formation, the second one has proved to work and produce reliable results with a considerably cheaper computational cost. Figure 1.8 shows the results from a gas dynamics simulation (Merlin et al. 2007) of the evolution of galaxies. Figure shows the temporal evolution of the stellar mass content in the simulations which agrees with the expected results and results from other works. On the other side, Figure 1.9 shows the Tully-Fisher diagram generated from the implementation of semi analytic model for galaxy evolution (Kang et al. 2005). We can see here how from this kind of simulations can be obtained not only information about the evolution of the baryonic matter content, but also photometric information about stars formed in the galaxies.

Chapter 2

Theoretical Framework

2.1 The Concordance Λ CDM Cosmological Model

As any theory, cosmology is based in a series of statements, axioms we assume have validity on the entire universe and which give support to the overall theory. That fundamental axioms are commonly based on the experience and are related with the intrinsic and more fundamental properties of the universe.

Currently we can say that cosmology is supported in to two basic axioms:

- The cosmological principle, which states that the universe is homogeneous and isotropic.
- The dynamics and the evolution of the universe is described by general relativity.

Under this two assumptions, we can work out a robust theory that describes the behavior of the universe, and that can be verified observationally.

The first modern model of the universe, we can say, was proposed by Einstein at 1916, when affirming that he found a way to explain the properties of the universe through the use of rules of general relativity. From then, many other models and variants has been presented, many of them based in the Einstein's ideas, or almost working with arguments of general relativity. Currently the accepted cosmological model is the Λ CDM concordance model, whose properties can be derived from fundamental ideas of general relativity and the cosmological principle.

Following ideas of cosmological principle, we can obtain an appropriated metric for the universe, the Robertson-Walker metric:

$$ds^2 = -dt^2 + a^2(t) \left[\frac{dr^2}{1 - kr^2} + r^2(d\theta^2 + \sin^2(\theta)d\phi^2) \right] \quad (2.1)$$

Here $a(t)$ is the scale factor which describes the evolving scale of the universe and k is the so called curvature constant. Using this metric, and the Einstein's equation

$$R^\mu_\nu - \frac{1}{2}g^\mu_\nu R = \frac{8\pi G}{c^2}T^\mu_\nu \quad (2.2)$$

it is possible to describe the evolution of the scale factor using the ordinary differential equations

$$\ddot{a} = -\frac{4\pi Ga}{3} \left(\rho + \frac{3p}{c^2} \right) + \frac{a\Lambda}{3} \quad (2.3)$$

and

$$\left(\frac{\dot{a}}{a} \right)^2 = \frac{8\pi G\rho}{3} - \frac{kc^2}{a} + \frac{\Lambda}{3} \quad (2.4)$$

Which has been called the Friedman-Lemaitre (FL) equations. In these equations ρ is the mass density in the overall sense (that is, rest mass plus any related with its energy), p is the pressure and Λ is the cosmological parameter, first introduced by Einstein as an arbitrary constant in the metric equations but transformed now as a parameter that could describe very novel effects

2.1.1 The Fluid Equation

To solve the FL equations we have to know the relation between ρ and p , (the equation of state) and the time variation of these quantities must be also pinpointed. This is done using the fluid equation, which can be derived from the first law of thermodynamics for an isolated system under a reversible expansion

$$\dot{\rho} + 3\frac{\dot{a}}{a} \left(\rho + \frac{p}{c^2} \right) = 0 \quad (2.5)$$

this equation describes the evolution of a perfect fluid in the expanding universe described by Friedman's equations. We have to stress the fact that the density ρ takes in to account all the contributions to the stress-energy tensor.

Solutions to Friedman's equations can be obtained using the fluid equation and assuming a form for the equation of state that relates ρ and p . In general we can assume

$$p = \sigma \rho c^2 \quad (2.6)$$

being σ a parameter which depend of the dominant matter-energy content. For a matter dominated (also known as dust models) $\sigma = 0$; in a radiation dominated universe (as well as a universe dominated by any relativistic particle as neutrinos) $\sigma = 1/3$; for vacuum energy $\sigma = -1$.

2.1.2 Cosmological Parameters

Here we enumerate some of the most important cosmological parameters. Table (2.1) shows the current values for these parameters and their uncertainties.

The Hubble Constant $H(t)$: The recessional velocity of galaxies is given by the Hubble law as

$$\frac{d\mathbf{r}}{dt} = H\mathbf{r} \quad (2.7)$$

where \mathbf{r} is the physical coordinate. If we work with comoving coordinates \mathbf{x} , then $\mathbf{r} = a\mathbf{x}$, and as $d\mathbf{x}/dt = 0$ we'll have

$$H(t) = \frac{\dot{a}}{a} \quad (2.8)$$

which relates the Hubble constant (actually the Hubble parameter) with the scale factor, more exactly, with the rate of expansion of the universe through the Friedman's equations. Note that $H = H(t)$, while $H(t = \text{now}) = H_0$, the so called Hubble constant.

The Critical Density ρ_c : From the second Friedman equation, the density of the universe required to have a flat geometry, i.e. $k = 0$ is

$$\rho_c = \frac{3H^2}{8\pi G} \quad (2.9)$$

Note that as the Hubble parameter changes with time, then also the critical density of the universe evolves with time.

The Density Parameter Ω_0 : Because is finally the density of the universe which defines its geometry, and then, its evolution, is common to parametrize the density of the different components of the universe as a function of the critical density. We define the density parameter Ω as

$$\Omega = \frac{\rho}{\rho_c} \quad (2.10)$$

Each mass-energy component of the universe has its own value of Ω .

The Cosmological Constant Λ : The cosmological constant was first introduced by Einstein in the field equation to allow the existence of a static universe. Since then, it has appeared several times in cosmology playing different roles in the models. Currently the Λ CDM cosmology assumes, with strong support from observations of the CMB, that the matter-energy density of the universe is dominated by a strange form of vacuum energy associated with zero point fluctuations of the vacuum field. This form of energy seems to dominate the energy content in the present universe.

Quantity	Value	Estimated Error
H_0	73.0 km s ⁻¹ Mpc ⁻¹	+0.28 -0.38
Ω_0	0.23	+0.03 -0.041
Ω_R	4.63×10^{-5}	
Ω_Λ	0.758	+0.035 -0.058

Table 2.1: Recent values measured for some cosmological parameters.(Spergel et al. 2007). Remember that according to cosmological evidence $\Omega_{Tot} = 1$.

The cosmological constant could be then expressed in terms of the mass density of a new form of energy

$$\Lambda = 8\pi G\rho_v \quad (2.11)$$

where ρ_v is the mass density associated with vacuum fluctuations and where we have used the equation of state for vacuum. Also taking in to account the definition of the critical density we can find that

$$\Omega_\Lambda = \frac{8\pi G\rho_v}{3H^2}. \quad (2.12)$$

Current cosmological evidence point out to the fact that universe has a critical mass-energy density content

$$\Omega_{Tot} = \Omega_m + \Omega_R + \Omega_\Lambda = 1. \quad (2.13)$$

2.1.3 Solution to Friedman's Equations and the Evolution of the Universe

Assuming no contribution from radiation or cosmological terms, the fluid equation (for matter) can be solved to give

$$\rho = \frac{\rho_0}{a^3} \quad (2.14)$$

Where we have assumed that $a(t = now) = a_0 = 1$. Substituting in the Friedman's equation, for $k = 0$, as assumed in the Λ CDM model, we have for the scale factor

$$a(t) = \left(\frac{t}{t_0}\right)^{2/3} \quad (2.15)$$

In this case, the universe will continue expanding forever but always at a slower rate. If we choose $k > 0$ the solutions will lead to a closed geometry and finally the universe will expand until some time that expansion will stop and falls back. If $k < 0$ the universe will be open and will expand forever, but with a constant rate of expansion.

Nevertheless is important to take the exact solutions for the Friedman's equations, then is needed to take numerical solutions. Some times is better to do a change, and not solve for the scale factor but for time. If we use the substitution

$$t = \int_0^t dt = \int_0^a \frac{a}{da/dt} = \int_0^a \frac{da}{\dot{a}} \quad (2.16)$$

then the solution for the equation can be written as a function of redshift

$$t(z) = \int_z^\infty \frac{dz}{(1+z)[\Omega_0(1+z)^3 + \Omega_R(1+z)^2 + \Omega_\Lambda]^{1/2}} \quad (2.17)$$

Some numerical integrations to (2.17) are shown in figure 2.2

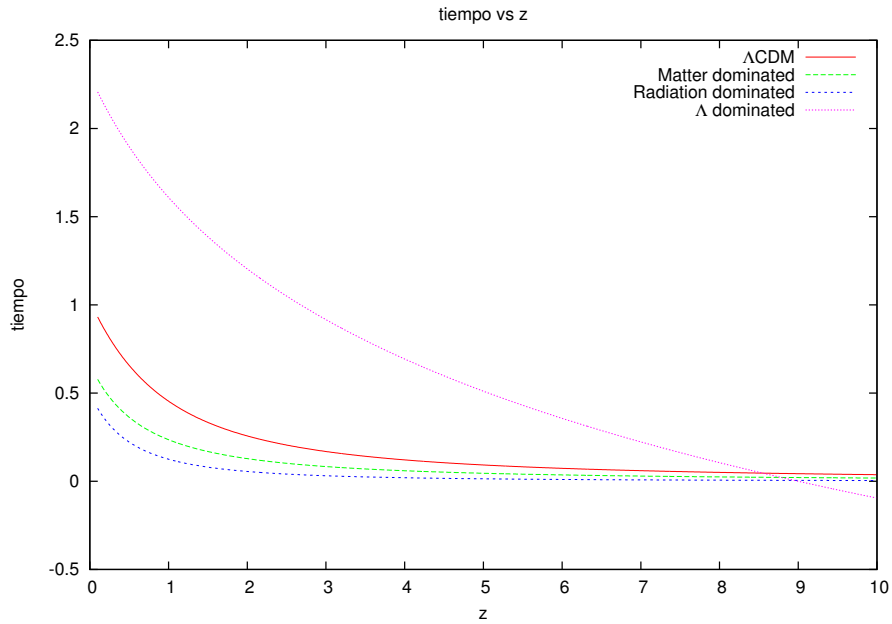


Figure 2.1: Numerical integration of Friedman's equation with different parameters to radiation dominated, matter dominated, Λ dominated and current universe

2.2 The General Framework for Structure Formation

The Λ CDM cosmology assumes that structure we observe today in the universe grows from density perturbations in a hierarchical form, that is, the first structures to form where the small ones, and then, through coalescence of this small structures, the big ones were established. If we define the density contrast as

$$\Delta(x) = \frac{\rho(x) - \bar{\rho}}{\bar{\rho}} \quad (2.18)$$

the current density contrast associated with a galaxy will be $\Delta_G \sim 10^6$, for a cluster of galaxies will be $\Delta_C \sim 10^3$ and for a super cluster of galaxies $\Delta_{SC} \sim 10$. Now, the growing of structure will be linear until $\Delta \sim 1$, then as $\rho \sim a^{-3}$, one can see that the redshift at which galaxies start to form is nearly $z \sim 100$, for a cluster $z \sim 10$ and for super clusters $z \sim 1$, in agreement with the assumption of the hierarchical formation.

Now, the objective is to write an equation for the evolution of the density contrast in the expanding universe. Starting with the fluid equations, one can arrive, before the inclusion of the expansion of the universe, at the couple of equations

$$\frac{d\Delta}{dt} = -\nabla \cdot \delta \mathbf{v} \quad (2.19)$$

$$\frac{d\delta \mathbf{v}}{dt} + (\delta \mathbf{v} \cdot \nabla) \mathbf{v}_0 = -\frac{\nabla \delta p}{\rho_0} - \nabla \delta \phi \quad (2.20)$$

$$\nabla^2 \delta \phi = 4\pi G \delta \rho \quad (2.21)$$

writing in comoving coordinates, and in the small perturbation regime, these equations drive to the general one

$$\frac{d^2 \Delta}{dt^2} + 2 \left(\frac{\dot{a}}{a} \right) \frac{d\Delta}{dt} - 4\pi G \rho_0 \Delta = 0 \quad (2.22)$$

Solutions for this equation can be obtained in the form

$$\Delta(a) = \frac{5\Omega_0}{2} \left(\frac{1}{a} \frac{da}{dt} \right) \int_0^a \frac{da'}{(da'/dt)^3} \quad (2.23)$$

or as an exact solution, in terms of Hypergeometric functions

$$\Delta(a) = a {}_2F_1 \left[-\frac{1}{3w}, \frac{w-1}{2w}, 1 - \frac{5}{6w}, -a^{-3w} \frac{1-\Omega_0}{\Omega_0} \right] \quad (2.24)$$

where w is a parameter. For a critical universe (i.e. $\Omega_{Tot} = 1$), these solutions can be reduced to

$$\Delta \propto t^{2/3} \propto a \quad (2.25)$$

$$\Delta \propto t^{-1} \propto a^{-3/2} \quad (2.26)$$

Which represent linear growing modes and decaying modes respectively. We are interested in solutions of the form (2.25), which represent growing mode in the linear regime.

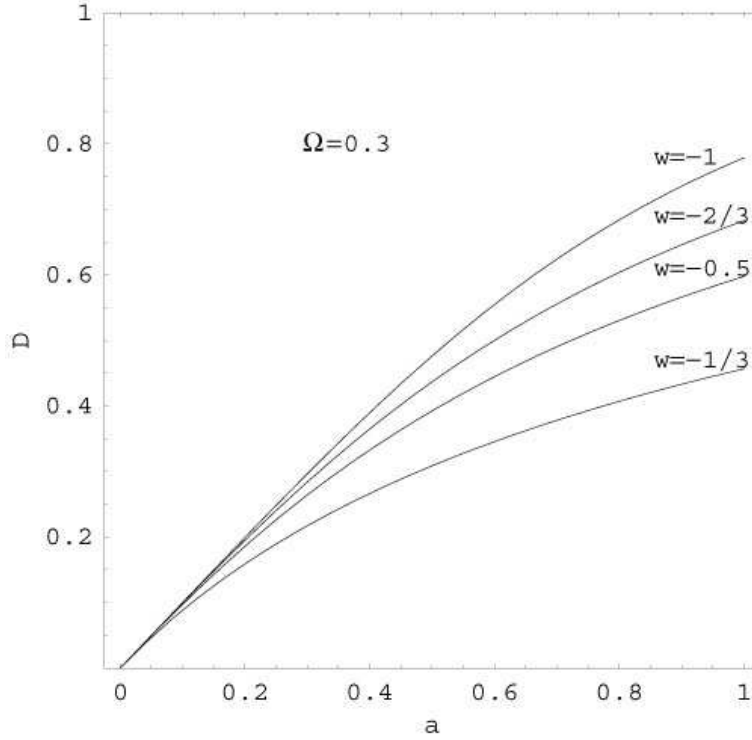


Figure 2.2: Solutions to the growth equation (also known as the growth function $D(a)$) obtained through the solution of hypergeometric functions. Curve marked with $w = -1$ corresponds to a solution with cosmological constant while $w = -1/3$ is related with an open universe.

2.3 The Zel'dovich Approximation

The nonlinear growth of structures is harder to follow analytically. Approximate solutions to the problem can be obtained through the use of Nbody simulations, but this simulations could obscure many detailed physical descriptions of the problem. One approximation that is commonly used to describe theoretically the evolution of the structures in the nonlinear regime is the Zel'dovich approximation.

In the Zel'dovich approximation the Lagrangian coordinate of a particle in an unperturbed distribution will be \mathbf{q} , then the particle trajectories could be written as

$$\mathbf{r}(t, \mathbf{q}) = a(t)\mathbf{x} = a(t)[\mathbf{q} + a(t)\mathbf{u}(\mathbf{q})] \quad (2.27)$$

where

$$\mathbf{u}(\mathbf{q}) = -\nabla\psi, \quad \text{with} \quad \psi = \frac{2}{3}H_0^{-2}\phi \quad (2.28)$$

The velocity field is obtained through derivation of the last expression, such that

$$\mathbf{v} = \frac{2a}{3t}\nabla\psi \quad (2.29)$$

and where ϕ is related to the density fluctuations in the linear regime through

$$\delta(a, \mathbf{q}) = -\frac{2}{3}H_0^{-2}\nabla^2\phi \quad (2.30)$$

Then, assuming that the undisturbed density is $\bar{\rho}$, the conservation of mass implies that

$$\rho(\mathbf{r}, t)d^3\mathbf{r} = \bar{\rho}d^3\mathbf{q} \quad (2.31)$$

Then, the perturbed density is given by

$$\rho(\mathbf{r}, t) = \frac{\bar{\rho}}{a^3(t)[1 - a(t)\lambda_1(\mathbf{q})][1 - a(t)\lambda_2(\mathbf{q})][1 - a(t)\lambda_3(\mathbf{q})]} \quad (2.32)$$

where $-\lambda_i(\mathbf{q})$ are the eigenvalues associated with the Jacobian of the transformation $\partial q_i/\partial r_j$. This equation describes the deformation effect of a cubical volume whose infinitesimal sides are given by λ_i . A positive value of λ will be associated with collapse, while a negative one will be associated with expansion of the perturbation.

Zel'dovich approximation is of common use in the generation of initial conditions for cosmological Nbody simulations.

Cosmological Nbody Simulations, Halo Identification and Properties

In order to study the properties of dark matter halos formed in cosmological Nbody simulations we realize a series of simulations of different resolution and different sample volumes. In this chapter we describe the techniques used to identify dark matter structures in those simulations and compute its properties. Such properties will be used in chapter 4 to study galaxy evolution with a semi analytical model.

3.1 Description to the Sample

Our work in this chapter and in chapter 4 is based in the results of a set of simulations we realize to study the properties of halos in those simulations, and to consider the resolution effects.

Initial conditions for simulations were generated with the software GRAFICS included in the package COSMICS (Ma & Bertschinger 1994). Simulations with names SFOF0# were ran until $z = 0$ to follow the evolution of structures in the complete volume. Simulations ZOOM0# were evolved up to $z \sim 2$ and were realized to increase the resolution of structures formed at high redshift, allowing a better study

Name	z_{init}	Npart	L (Mpc h^{-1})	ϵ (Mpc h^{-1})	m_i ($\times 10^{10} M_{\odot}$)
SFOF03	34.29950	32768000	100	0.005	0.203393
SFOF06	31.81119	16003008	100	0.0045	0.416227
SFOF05	26.95058	4913000	100	0.007	1.355770
SFOF04	20.17790	1000000	100	0.01	6.521860
ZOOM01	50.31220	16003008	10	0.0014	0.000416
ZOOM02	53.43680	4913000	10	0.0014	0.001353

Table 3.1: Table of simulations we ran for this work.

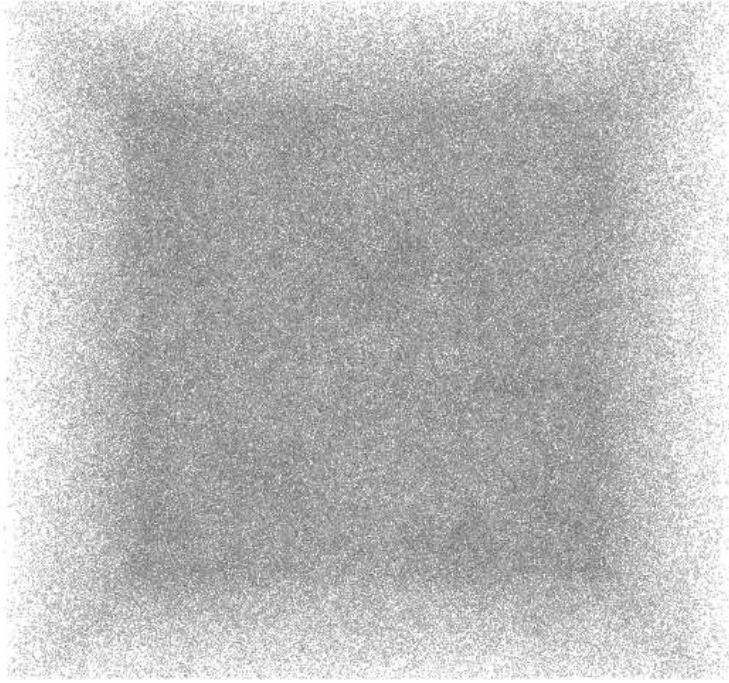


Figure 3.1: Snapshot from the simulation SFOF03 at $z=4.95$. Note how the distribution of particles appear to be very homogeneous, but actually there are many subtle inhomogeneities

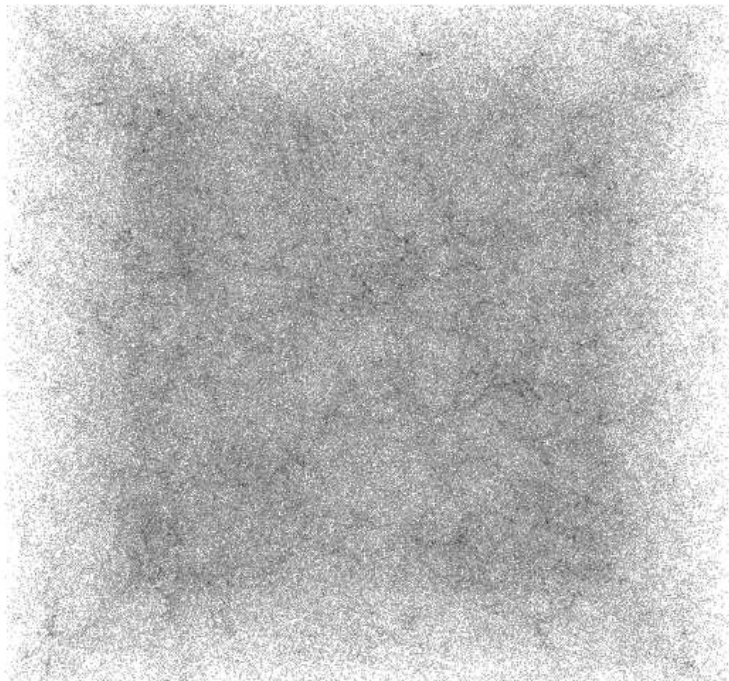


Figure 3.2: Snapshot from a simulation (as figure 3.1 and 3.3 SFOF03) at $z=1.91$. As in figures 3.1 and 3.3 the box appearance is because we are seeing the snapshot in projection

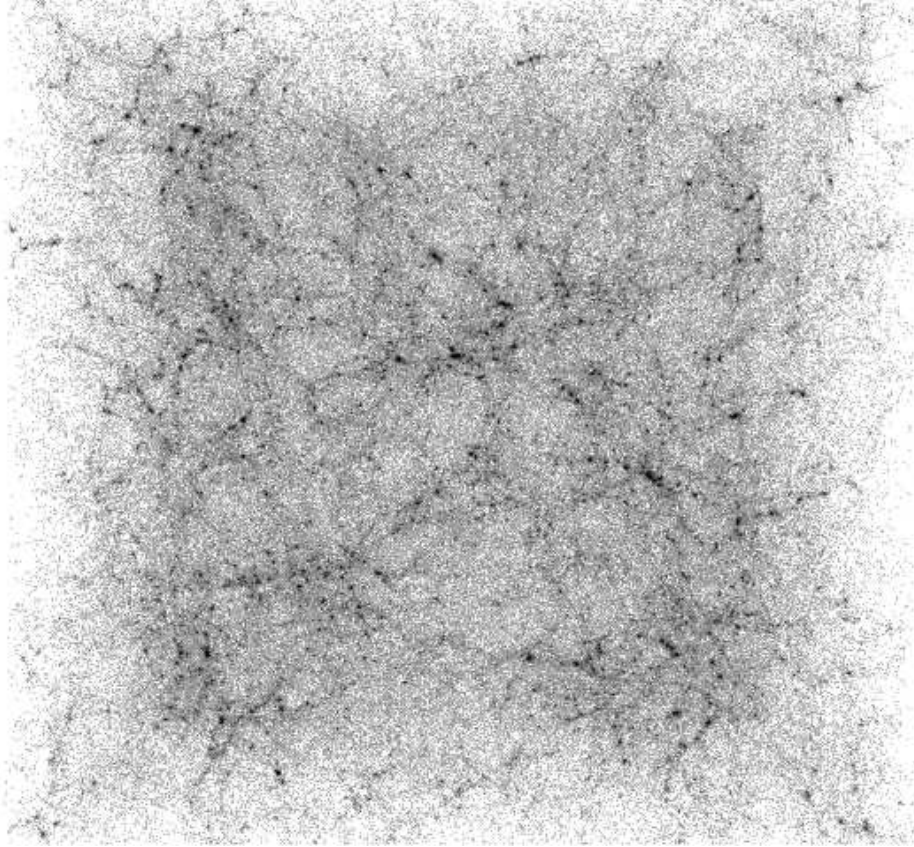


Figure 3.3: Snapshot from a simulation at $z=0$. Here we can see many structures formed and some filaments of mass in the distribution of matter, in a different way to we can see in figure 3.1 or 3.2

of properties of halos at that redshifts.

Simulations were ran using the GADGET2 code (Springel 2005), using the TreePM technique, in which we used 128 grid points for the PM approximation, and allow for an error of 0.001 in the force estimation.

3.1.1 Cosmological Initial Conditions

Here we give a brief description to the basic method used to generate cosmological initial conditions, for a most complete discussion see Bertschinger 1994 and Klypin 2000 and references therein.

One of the most common procedures used to setup cosmological initial conditions is the Zel'dovich approximation. The method consists in to suppose we know the linear growing function $D(a)$, and with this, build a comoving density field $\rho(\mathbf{x})$ from an homogeneous density field $\rho(\mathbf{q})$ evaluated in a specific cosmic epoch a .

The Zel'dovich approximation (see section 2.3) can be also written for positions as

$$\mathbf{x} = \mathbf{q} - \alpha \sum_k D_k(t) S_k(\mathbf{q}) \quad (3.1)$$

and for the momentum as

$$\mathbf{p} = -\alpha a^2 \sum_k D_k(t) \left(\frac{\dot{D}_k(t)}{D_k(t)} \right) S_k(\mathbf{q}) \quad (3.2)$$

where $D_k(t)$ is the linear growth function (see eqs. 2.23 and 2.24), $S(a)$ is the displacement vector and is related with the velocity potential and the power spectrum of primordial density fluctuations (see eqs. 2.27 to 2.29) and where α is a parameter that defines the normalization of the fluctuations.

Here quantities with subscript k are related with Fourier transformations (actually the reciprocal space), then, if we build a regular mesh enclosing all the mass distribution of the system in the physical space we will have

$$S_k(\mathbf{q}) = \sum_{k_{x,y,z}=-kmin}^{kmax} ik C_k \exp(i\mathbf{k} \cdot \mathbf{q}) \quad (3.3)$$

with

$$k_{x,y,z} = \frac{2\pi}{L} \{i, j, k\} \quad \{i, j, k\} = 0, \pm 1, \pm 2, \pm 3, \dots \pm N_p/2 \quad (3.4)$$

where L^3 is the cubic volume in the simulation (that is, the size of the grid), N_p^3 is the total number of particles in simulation, and the volume has been discretized in L^3/N_p^3 points. In these relations the number C_k is given by

$$C_k = \sqrt{P(k)} \left[\frac{G(0,1)}{k^2} - i \frac{G(0,1)}{k^2} \right] \quad (3.5)$$

where $P(k)$ is the power spectrum and $G(0,1)$ are Gaussian distributions between 0 and 1 with dispersion

$$\sigma^2 = \frac{P(k)}{k^4} \quad (3.6)$$

The general algorithm to draw the initial conditions follows these lines

- Define the total number of particles in the simulation, N_p^3 , and the box size L . That is, define the sample size and the resolution of the simulation.
- Build the grid of N_p^3 cells, such that $\Delta q = L/N_p$ and each particle is located in the center of a cell with coordinates

$$q_{i,j,k} = (ijk)\Delta q \quad \{i, j, k\} = 0, \pm 1, \pm 2, \pm 3, \dots \pm N_p/2$$

- Build the reciprocal grid with $\Delta k = 2\pi/L$, thus $k_{i,j,k} = (ijk)\Delta k$.

- Use $P(k)$ to compute C_k for every k -value.
- Compute $S_k(q)$ for every q_i .
- Using $S_k(q)$, $D(a)$ and q_i compute the comoving density field $x_i(t)$ through the use of the Zel'dovich approximation and compute the velocity field from 3.2.

In figures 3.1 to 3.3 we show an example of initial conditions drawn from these procedure, and the evolution of the system up to recent cosmic epoch.

3.2 Halo Identification

For the identification of halos in simulations we used the commonly used FOF method (Davis et al. 1994, Pfizner et al. 1997). In this method, no explicit physical considerations are assumed in the implementation.

For the FOF method one choose a particle of the sample (for example, the i th particle) and define a spherical region around this particle with radius equal to b_{link} times the mean inter-particle distance, being b_{link} a free parameter known as the linking length parameter. Once the region has been defined, every particle inside this region is found and mark it as a *friend* of the i th particle. Next, around every j th *friend* particle, the same region is identified, its *friends* particles are found. At the end one has a hierarchy of friends of friends that finally define the structures.

Groups of particles that arise from the application of the method must fulfill a final requirement. It is required that every group must have almost N_{min} members. Can be demonstrated, using spherical collapse approximation, that the method allow for the detection of density enhancements of nearly $200\rho_c$ when $b_{link} \sim 0.2$ and $N_{min} = 32$. In our implementation, we used the FOF libraries of the *Nbody Shop*¹ to generate the list of FOF groups in every snapshot.

If we not look for substructure in the FOF groups then we can proceed with the evaluation of the binding condition for the halo. We compute the total energy of every particle in the halo, and choose the center of the halo as the position of the most bound particle, defined it as the particle with the lowest potential energy. Then we compute the total energy of every particle (including Hubble flow corrections) and iteratively discard unbound particles. Every time we discard a new particle the

¹<http://www-hpcc.astro.washington.edu/>

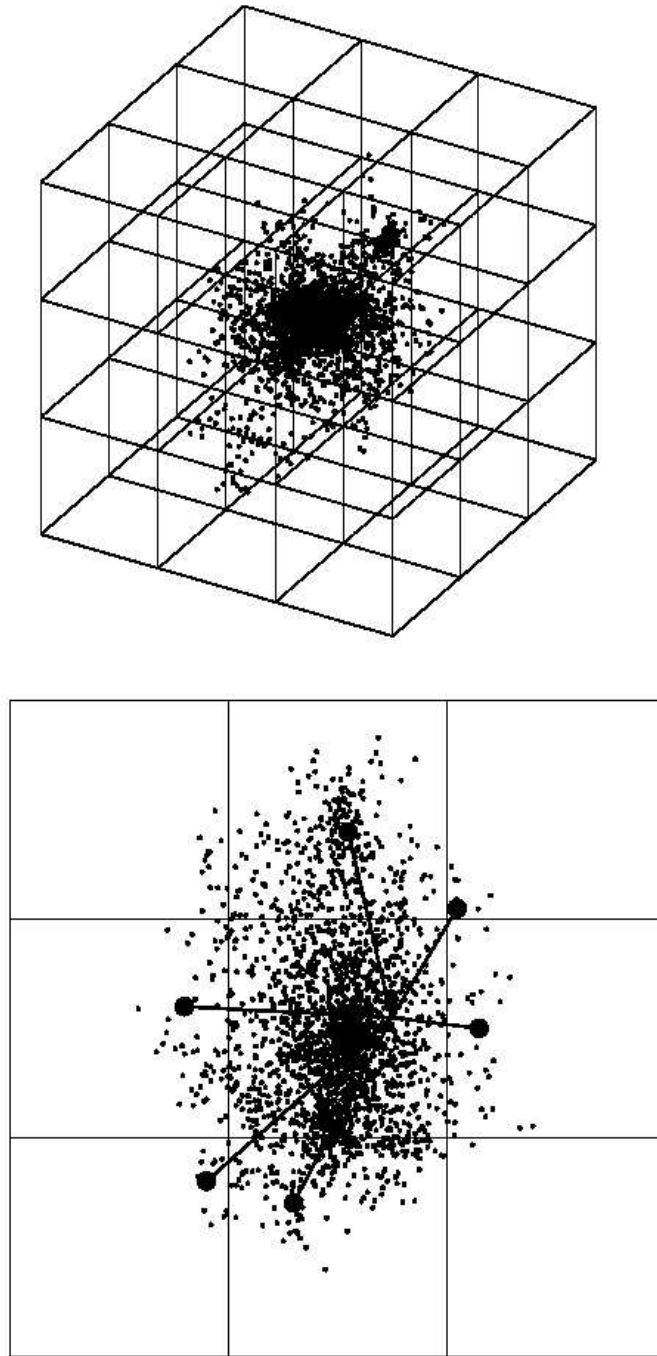


Figure 3.4: Grid operation in the computation of the potential. Up, a FOF group enclosed by a cubic box partitioned in to 27 cubic subcells (we must mention that our implementation does not necessarily uses cubic cells). Down, computing of the potential energy over a particle in the central box. P-P contributions are computed for its most neighbor particles, while particle-pseudoparticle contributions are computed for the remainder cells. Big dots marks the position of the pseudoparticles associated with every cell.

center of the halo is recomputed, and the process start again.

Because large simulations have a large number of big FOF groups, the computing of the total energy will involve many iterations, which finally will drive to a huge consumption of computational time. To overcome this inconvenient we approximate the calculation of the potential energy of particles in FOF groups through the implementation of a grid method. We used a grid method in which the overall FOF group is enclosed in a box, which is partitioned in N_c cells. Then every cell is a data structure that can register the Id of every particle inside, which can be used to compute the potential energy in a simple way.

To compute the potential energy of the j th particle, we loop over the particles that belong to the same cell, and then, compute the potential energy in a direct way for this neighbor particles. Next we loop over all cells in the box and compute the contribution to the potential from a pseudo-particle with mass equal to the total mass inside the cell located at its center of mass. Finally, we add dipole corrections to correct for errors associated with spatial distribution of matter inside the cell.

In order to increase the efficiency of the code, we eliminate fractions of the unbound particles instead of eliminating particle by particle. Following Weller et al. (2005), we eliminate one third of the free particles of the list every iteration, but when the number of free particles is lower, say ten particles, the elimination is done particle by particle in order to avoid violent fluctuations in the energy when converging to an unbound structure.

The precedent description of detection of halos in simulations applies when the resolution of the simulation is not enough to allow the formation of substructure. If the simulations has sufficient resolution, the FOF halos identified according to the last procedure will be built of many substructures, then will be needed to identify substructure in that halos. To proceed with that identification we start from the original FOF halo, without evaluate binding and we wait to evaluate binding until the substructures has been identified.

3.3 Halo Substructure

As shown by Klypin et al. 1999, when the resolution of simulations is high enough, they allows the identification of substructure, that is, small physical structures hidden in to the FOF halos. Because the FOF method has no explicit physical criterion to group particles, some times the method join neighbor structures that are connected via FOF hierarchy but are dynamically uncouneted. To overcome this problem, which is very common in intermediate-high resolution simulations, there is needed the implementation of a different method that allow the identification of bound substructure in a FOF halo.

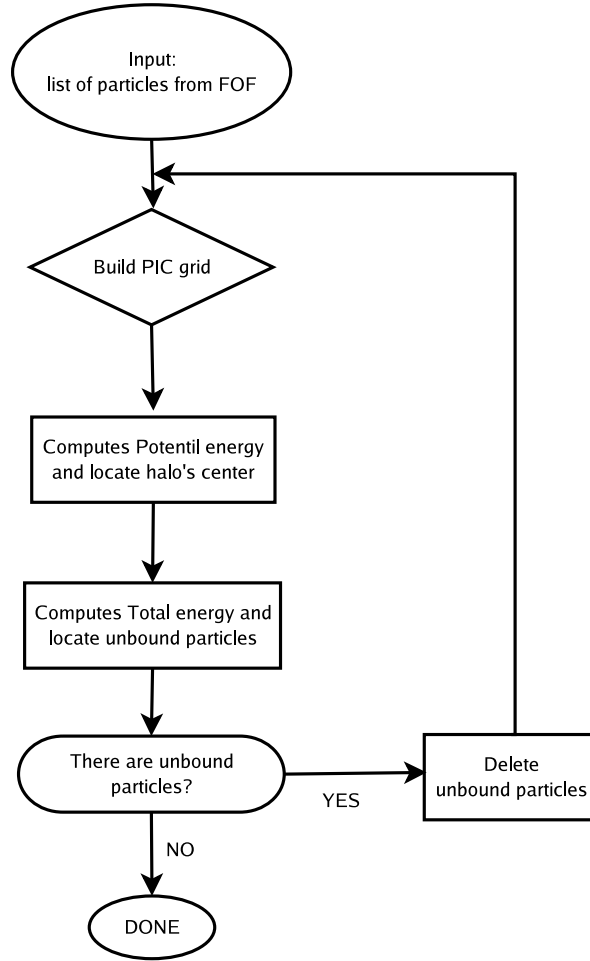


Figure 3.5: Flow chart of identification and binding a FOF halo

Different method has been proposed to this aim, (Skid, Denmax, SO, VoBoz, etc). In this work we will adopt the SUBFIND method (Springel et al. 2001), but we are going to propose a subtle modification to the method in order to reduce the number of free parameters and the computing time. Now we give a brief description for the method of subhalo identification.

3.4 The Method

We define a substructure as a bound overdense self-gravitating region immersed in a non resolved halo detected by the FOF routine. Although not complete, this definition will be enough for the purposes of this work. The idea behind the method presented here is based in the fact that density enhancements in the mass distribution of a halo are also associated with deeper potential wells. Then, basically to locate a substructure we look for those points in the mass distribution where the potential energy of particles is the lowest. At those points we locate the center of

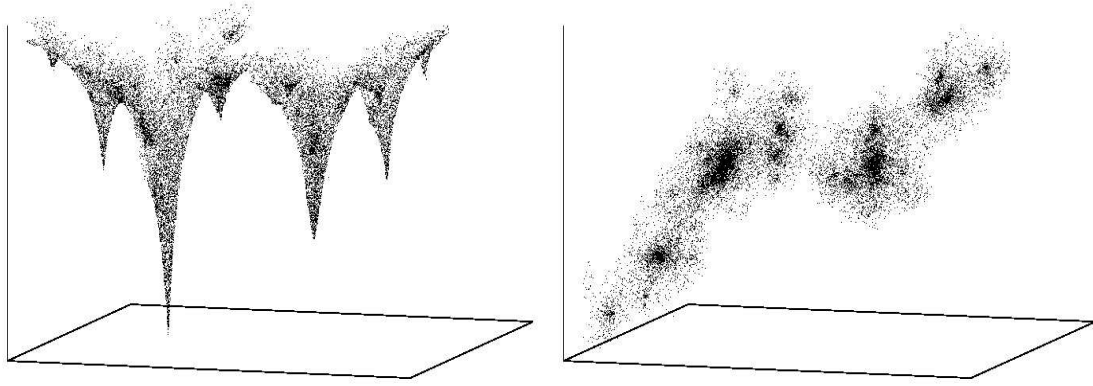


Figure 3.6: (a) Distribution of the potential energy of particles in a FOF halo identified in a simulation of 320^3 particles. (b) Projection of the halo itself.

the potential well and build up the substructure by identifying the particles enclosed by it.

In the following we give a more detailed description of the method.

3.4.1 The method for halo identification

The method we present here is based in that one described by Springel et al. (2001). The reader is referred to that work for complementary information.

We start with the identification of FOF halos. For every FOF halo identified in the simulation we compute the potential energy for every particle in that halo.

Next we sort the particles in the halo according to increasing values of potential energy and storage this order in a list, in such a way that the most bound particle in the FOF halo will be at the start of the list.

Then, starting with the most bound particle we walk the list orderly and look for the set of NGB nearest neighbors of that particle. Of that set of nearest neighbors we storage a subset with the particles that have potential energy less than that of the particle we are interested.

Finally of that subset we choose the two ones more nearest and then evaluate this three possible situations

- If the particle has no neighbors with lower potential energy, then it is the center of a potential well, that is, a substructure, therefore a new substructure is created there and we move to the next particle.
- If the particle has only one neighbor with potential energy lower than it, this means that the particle is the second most bound particle in the substructure,

and it belongs at the same substructure that its neighbor, then it is marked with the same label that its neighbor.

- If the particle has two immediate neighbors with potential energy lower than it, then we ask if the particles belong to the same substructure, if both belong to the same substructure, then the particle also belongs. If not, the particle is a saddle point in the potential and marks the “border” of the distribution. Particles that are saddle point are stored in memory to verify their parent subhalo.

Once the initial substructures has been located using the procedure described before we proceed to evaluate the boundness of each substructure, starting at the center of a subhalo, defined as the position of the most bound particle, we compute the potential energy of every particle belonging to it and eliminate the unbound ones. To increase the efficiency of our implementation we used a grid method (Hockney & Eastwood 1988) to compute the potential and to eliminate groups of unbound particles. The unbound particle elimination procedure is parametrized by two free quantities, F_{min} and N_{min} . When more than F_{min} unbound particles are found in a subhalo one third of the most unbound particles are eliminated. In order to avoid fluctuations in the potential energy when there are few unbound particles (which is the case when the number of unbound particles is less than F_{min}) the elimination is done particle by particle. Our experiments show that values for F_{min} in the range $5 < F_{min} < 10$ are rather appropriated. The center of the subhalo as well as the potential energy of the particle belonging to it is recomputed each time a particle or bunch of them are eliminated, then the procedure is iteratively repeated until all the particles in the subhalo are bound or if the number is lower than a minimum per substructure N_{min} .

3.4.2 Results

To test the method first, we perform a cosmological simulation of 320^3 particles in a cubic volume of side $L = 100\text{Mpc}h^{-1}$. Initial conditions were generated using the code GRAFICS (Ma & Bertschinger 1995) according to the concordance ΛCDM cosmology ($h = 0.73$, $n = 1$, $\sigma_8 = 0.77$, $\Omega_\Lambda = 0.76$, $\Omega_m = 0.24$). The simulation was done using GADGET2 (Springel 2005) with the TreePM feature. The evolution was followed from $z=34.3$ until $z=0$.

We used the FOF routine provided by the *Nbody Shop*² to identify halos in the simulation. Figure 3.6 shows the potential energy values of the particles in a FOF halo at $z = 0$ as a function of the (x,y) coordinates, and the 3D distribution of the same set of particles. We can clearly see the position of several local potential wells in the distribution. Every peak is at the center of a candidate subhalo. This particular halo is one of the most massive FOF halos identified in our simulation having a total

²<http://www-hpcc.astro.washington.edu/>

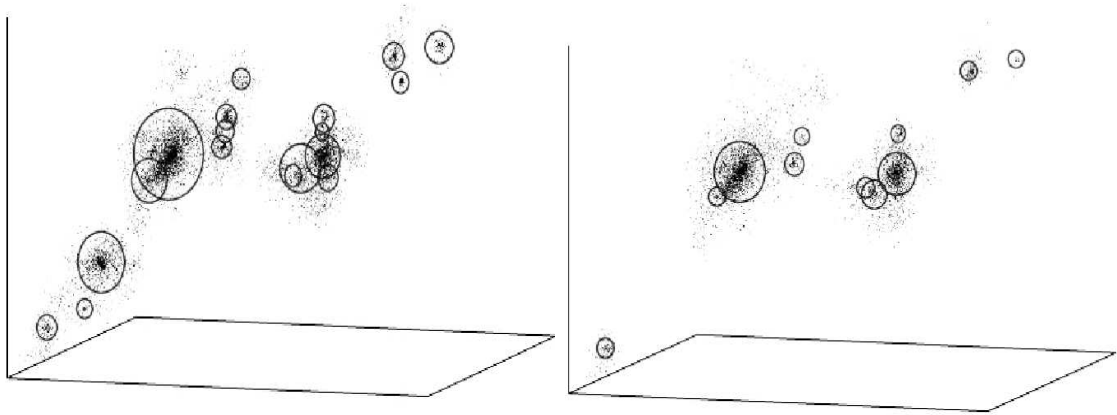


Figure 3.7: (a) Subhalos identified to grow around the potential wells of the distribution. (b) Survivor halos after the evaluation of binding of particles in every subhalo to the left. In this analysis $N_{min} = 16$

mass of $3.6 \times 10^{13} M_{\odot}$ and 17752 particles.

In figure 3.7 the subhalo candidates (a) and the survivor subhalos (b) are depicted. The survivor halos have been selected and constructed using our method. In the particular case of the halo shown here, the method initially finds 18 subhalo candidates among which only 11 survive to the binding requirement. The most massive subhalo (at the first level of the substructure hierarchy) has a mass of $8.70 \times 10^{12} M_{\odot}$ while the smallest one has a mass of $4.5 \times 10^{10} M_{\odot}$. The last value is of the order of the mass of present day galactic halos.

To test the response of the method to variations of the parameters, we ran the analysis three times on the same simulation using every time distinct number of nearest neighbors (NGB). We used values of the NGB=16, 32 and 64. When NGB=16 we perceived an increased ability of the method to resolve low mass (low number of particles) subhalos (see figure 3.8), but a decreased ability to resolve massive ones when compared with the same case for the NGB=64. In any case, because fluctuations of the potential must appear by the discrete nature of mass distribution, we recommend to use a NGB higher than 32 in order to avoid to detect anomalous fluctuations in mass density distribution and to allow a most complete search for the hierarchy of potential distribution around the potential wells. No tests were done changing the N_{min} , because it is clear that decreasing values of the N_{min} will drive an increase in the number of survivor subhalos.

Figure 3.9 shows the halo mass distribution for the simulation. As it is clear from there the use of the method for substructure identification enriches the distribution at low mass values. Clearly with higher resolution simulations this enrichment will be higher. The results in figure 3.9 show also a good agreement with the standard power law distribution of the form M^{γ} , with $\gamma = -2.066$.

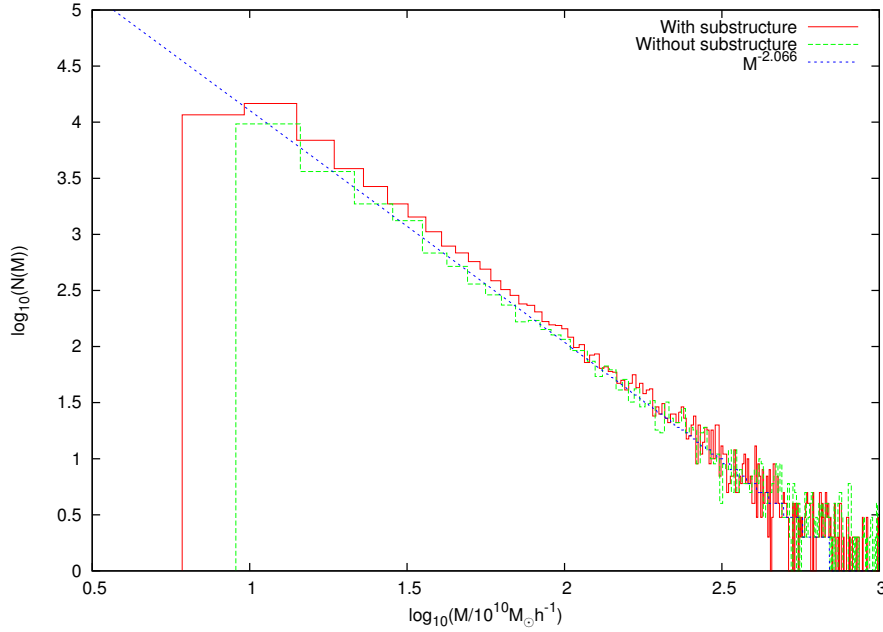


Figure 3.8: Comparison of halo mass distributions for the simulation using only FOF and including subhalos identified at first level of hierarchy of substructure. Doted diagonal line corresponds to a power law of $\gamma = -2.066$.

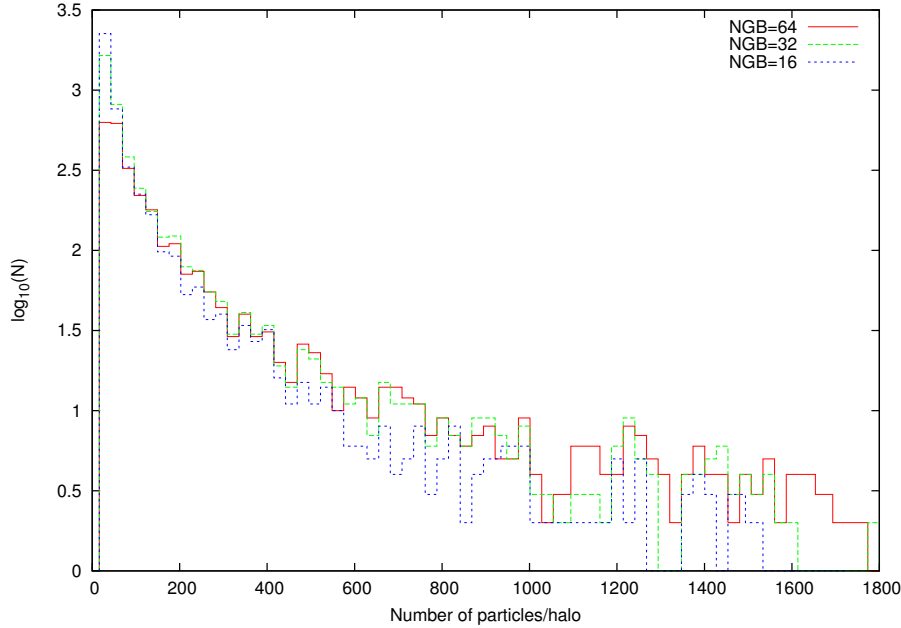


Figure 3.9: Distribution of subhalos identified as a function of the number of particles/subhalo for different values of the number of nearest neighbors used to the subhalo identification.

3.5 Physical and Statistical Properties of Halos

Once halos has been identified we compute several physical properties for them. Every quantity gives valuable information about dynamical state of the halo. These properties are also computed to be used next in the semi analytic models of galaxy

formation.

Total Halo Mass: As must be clear, properties of structures are completely dependent of halo mass. Here we compute the total mass as the sum of the mass of all particles in the halo (after the binding process).

Halo Position: As mentioned, we define the position of the center of the halo as the position of the most bound particle.

Halo Velocity: Because the center of the halo has been defined by the most bound particle, here we approximate the velocity of the halo as the velocity of that particle.

Position of the Center of Mass: This is the position of the center of mass of the halo, that in principle could be distinct to the position of the center of the halo.

Velocity of the Center of Mass: Velocity of the center of mass of the halo.

Subhalo mass fraction: To consider the fraction of mass of a halo in the form of substructure we compute this quantity as the sum of the masses of all substructures in the halo.

Total kinetic energy: During the binding process we compute the kinetic energy of every particle. The total kinetic energy of the halo is computed as the sum of kinetic energies over particles in the halo.

Total potential energy: Total potential energy computed during the binding procedure. This quantity is approximated for massive halos using a grid method.

Virial Radius: The virial radius is defined as the radius of a spherical volume within which the mass density is Δ_c times the critical density of the universe at that redshift,

$$M_{vir} = \frac{4\pi}{3} R_{vir}^3 \rho_c \delta_c \quad (3.7)$$

where (see Bryan & Norman 1998)

$$\Delta_c = 18\pi^2 + 82x - 39x^2 \quad \text{with} \quad x = \Omega(z) - 1 \quad (3.8)$$

and

$$\Omega(z) = \frac{\Omega_0(1+z)^3}{E^2(z)} \quad \text{with} \quad E^2(z) = \Omega_0(1+z)^3 + \Omega_R(1+z)^2 + \Omega_\Lambda \quad (3.9)$$

To compute R_{vir} we compute $\Delta_c \rho_c$ and evaluates the mean density of every halo from $r = 0$ to the point where the equality $\bar{\rho} = \Delta_c \rho_c$ is reached. The virial radius

will be the lower radius at which this condition is fulfilled.

Virial Mass: It is the mass that appears in equation (3.7), it is computed as the mass interior to the virial radius.

Virial velocity: The virial velocity is related with the mean velocities of particles in a virialized halo of mass M_{vir} and radius R_{vir} , and it is defined as

$$V_{vir}^2 = \frac{GM_{vir}}{R_{vir}} \quad (3.10)$$

Virial Temperature: If we suppose that the material in the halo is at a nearly isothermal state (which as been verified for the regions not affected by the cooling flows in the very center of the halo), the equation of hydrostatic equilibrium allow us to define

$$T_{vir} = 35.9 \left(\frac{V_c}{\text{kms}^{-1}} \right)^2 \quad (3.11)$$

Where V_c is the circular velocity of the halo ($V_c^2 = d\phi/dr$). V_c but can be well approximated by V_{vir} .

Spin Parameter: The spin parameter (λ) is a dimensionless quantity that quantifies the amount of angular momentum required for rotational support in a homogeneous rotating body. It is calculated as the ratio between the centrifugal to gravitational acceleration of the body.

$$\lambda = \frac{J\sqrt{|E|}}{GM^{5/2}} \quad (3.12)$$

Where J is the total angular momentum, E is the total energy and M is the total mass of the halo.

Table 3.2 summarises every quantity and describes the data structure used in our code to storage data per halo.

3.5.1 Density contrast

In order to follow the evolution of the density contrast in time in our simulations we compute the density contrast associated at every halo identified at different redshifts and study its distribution for different redshifts to see how it evolves in time. For every halo identified we compute the density contrast as

$$\Delta = \frac{\rho - \bar{\rho}}{\bar{\rho}} \quad (3.13)$$

The mean density per halo ρ is computed using one half of its total mass and the half mass radius of the halo $R_{m/2}$, which is defined it as the radius at which half

mass of the halo is contained.

In figure 3.10 we show the distribution of densities at redshifts $z=0, 0.43, 1.03, 1.91, 3.16$ and 4.94 . Figures shows a clear difference between the curves for the different resolutions. Figure 3.11 show the density distribution for the same set of simulations at different redshifts

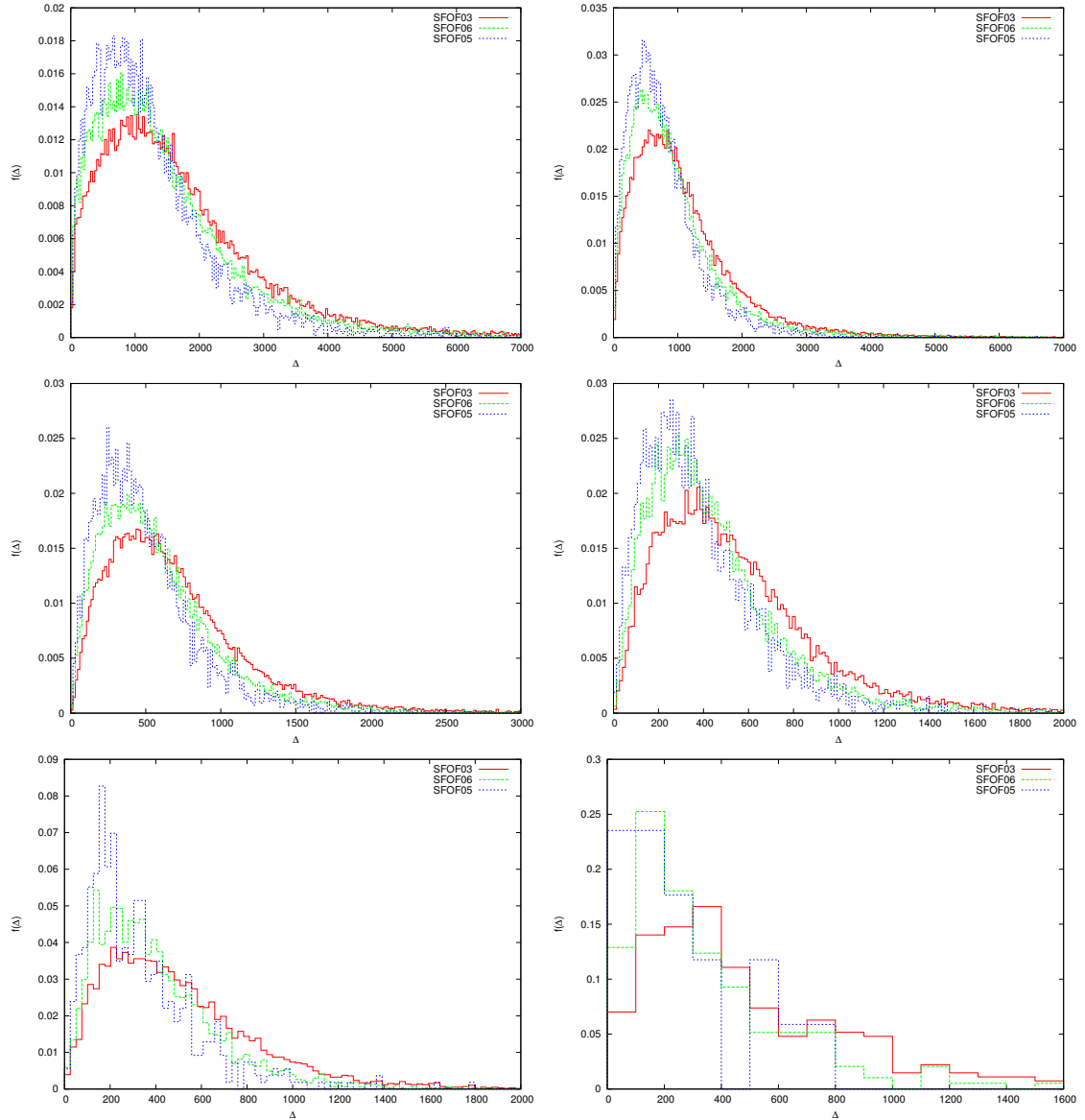


Figure 3.10: Distributions of density contrast of halos at a sequence of redshifts for every SFOF simulation. The upper left panel is at $z=0$ while the lower right is at $z=4.9$

In Figure 3.10 we can see the distribution of density contrast for the three simulations SFOF (see table 3.1) at different redshifts. Note how for the same redshift, the distribution is more peaked at the region of lower Δ for the simulations of lower resolution, as can be seen in the figure, where the blue curve is always at the left of

the green and red ones. Also, depending of the resolution, the width of the distribution is higher for high resolution simulations at every redshift.

This can be understood in terms of the resolution of the simulations. In high resolution simulations, the low mass of the particles allow the system to form more small and more clustered systems, with increased density, and finally increased Δ , while for lower resolution simulations, the high mass of the particles and the lower spatial resolution does not favour the formation of small structures with high density contrast, and allows only the formation of the big ones without detailed information about small scale structures. This decreased resolution does the distribution more concentrated near values of lower density.

Also, from $z = 4.9$ (lower right panel) until $z = 0$ (upper left panel) we can see how the distribution of Δ changes with time. Note how for $z = 4.9$ the distribution is strongly peaked at lower values of density contrast $\Delta \sim 200$, while at the subsequent panels, increasing z the peak of the distribution shifts at every time towards higher values of Δ . While the increase of the density contrast happens the distribution widens, allowing a more broad population of objects with distinct density contrast. Finally the distributions are peaked at values $\Delta \sim 1000$, the density contrast commonly associated with clusters of galaxies.

Figure 3.11 shows more detailed the temporal evolution of the Δ distribution. At high redshift (cyan curve) the distribution is thin and peaked at lower Δ values. While redshift decreases the distribution becomes more broad and the peak shifts (curves violet, blue and green). Once $z = 0$ the distribution is peaked at $\Delta \sim 1000$ and enough broad to allow the existence of structures with many different density contrasts. Clearly, in the spirit of the discussion mentioned above, if simulations of higher resolution are made, the distribution could be peaked at higher values of Δ as the result of the inclusion of many small, high density structures.

According to the linear theory, the amplitudes of the density fluctuations of mass M can be described by a Gaussian distribution

$$p(\Delta) = \frac{1}{\sqrt{2\pi}\sigma(M)} \exp \left[-\frac{\Delta^2}{2\sigma^2(M)} \right] \quad (3.14)$$

This result originally applies in the linear regime, nevertheless there is no reason to consider that this distribution still being valid at any time, even during the phases of the nonlinear collapse.

We fit the density distributions with a log-normal distribution of the form

$$p(\Delta) = \frac{1}{\Delta\sigma\sqrt{2\pi}} \exp \left[-\frac{(\ln \Delta - \mu)^2}{2\sigma^2} \right] \quad (3.15)$$

which seems to have a behavior similar to the distribution we acquired in our results.

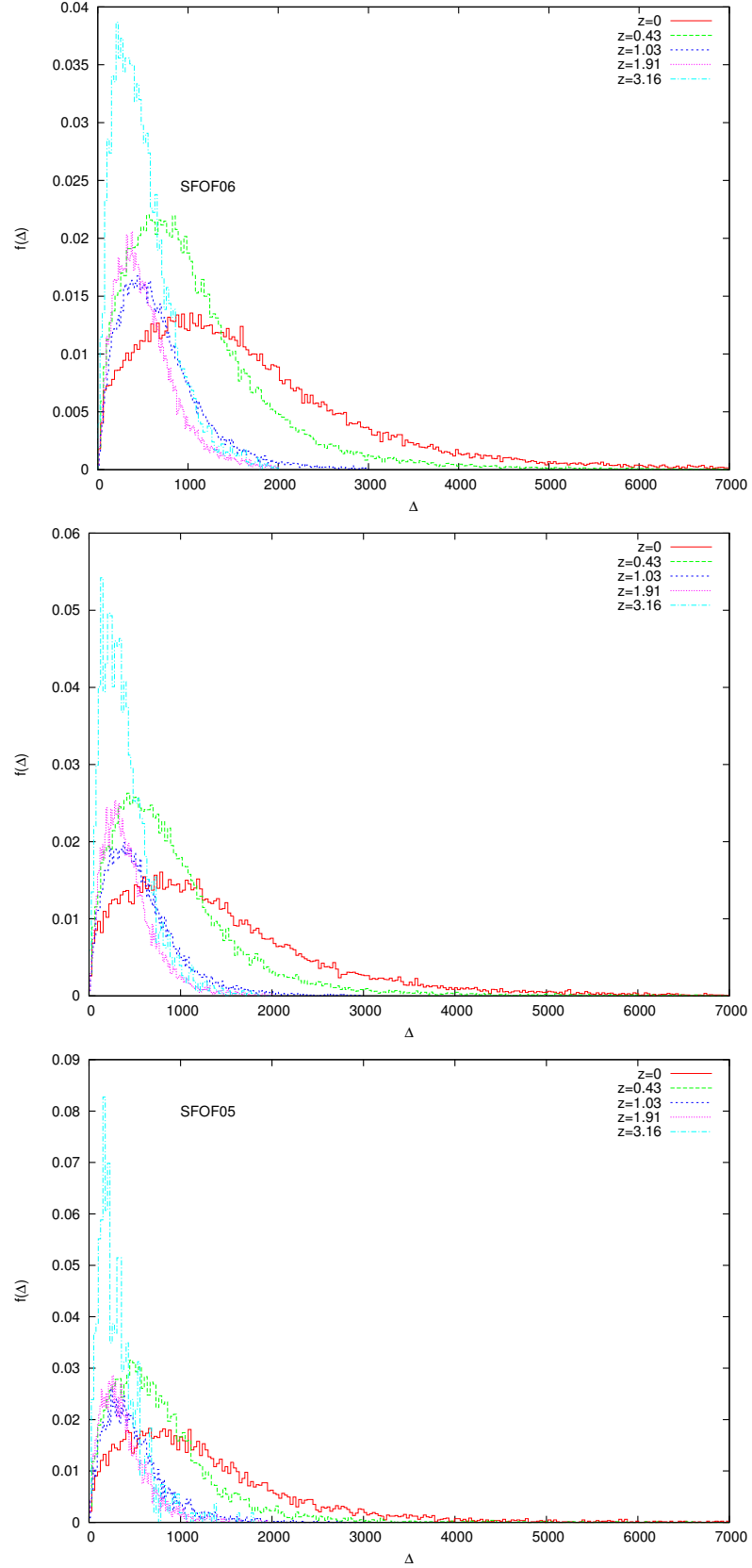


Figure 3.11: Distribution of density contrast for halos in simulations, every box has the sequence for the distribution for every simulation.

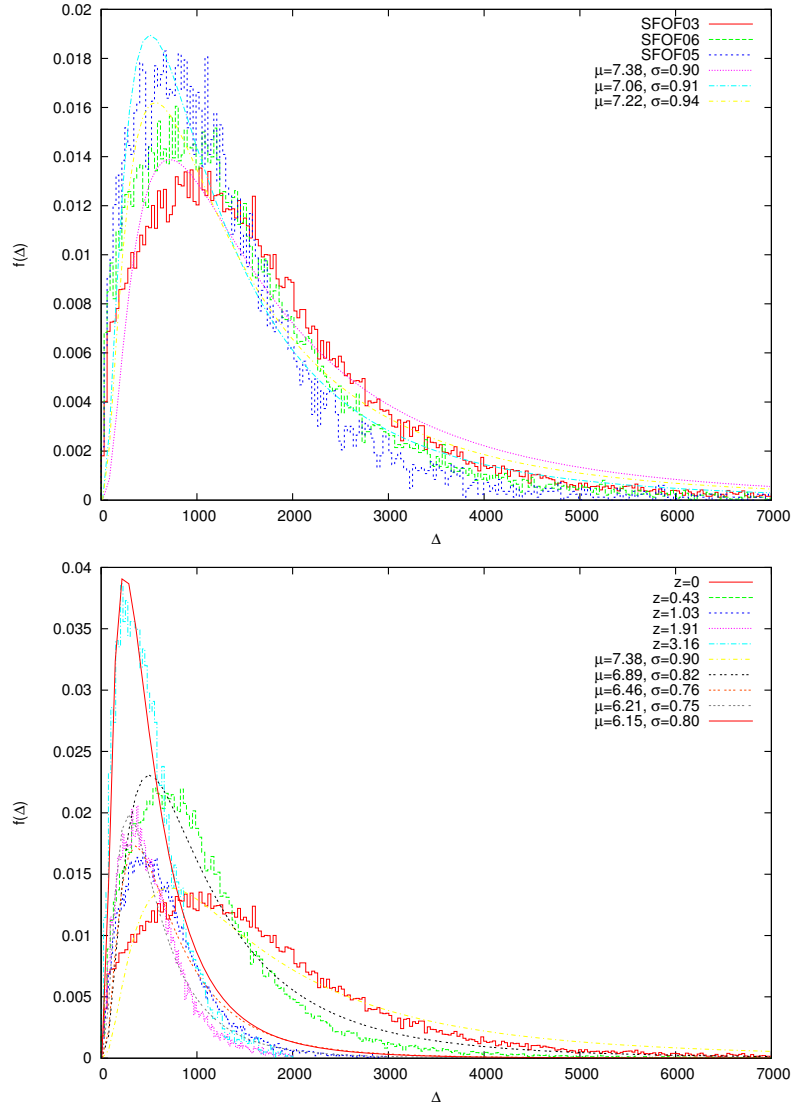


Figure 3.12: Fit of the density distribution to a log-normal function

As we can see from figure 3.12 the distribution fits quite well for redshift $z > 0.43$, nevertheless the distribution fails to describe data at $z < 0.43$. The distribution is more broad and the shape of the peak is very different at low redshifts. We did the fit also for all data at $z = 0$ in every SFOF simulation, and we find indeed that the distribution for SFOF05 gives a best fit than that for SFOF03 (lower and higher resolutions respectively), then could be some effect associated with the resolution of the simulations in the shape of the distribution of the density contrast.

3.5.2 Correlation functions and bias factor

A common practice to quantify clustering in problems related with observations and theory about the large scale structure of the universe involves the calculation of the correlation function $\xi(r)$ (or $\xi(\theta)$ if is related to observations). The correlation function $\xi(r)$ tries to quantify the clustering trough the counts of close pairs among

particles in the universe.

The three-dimensional correlation function can be defined as

$$N(r)dV = N_0[1 + \xi(r)]dV \quad (3.16)$$

where $N(r)dV$ is the number of particles in the volume element dV at distance r from any other particle and N_0 is a space average density.

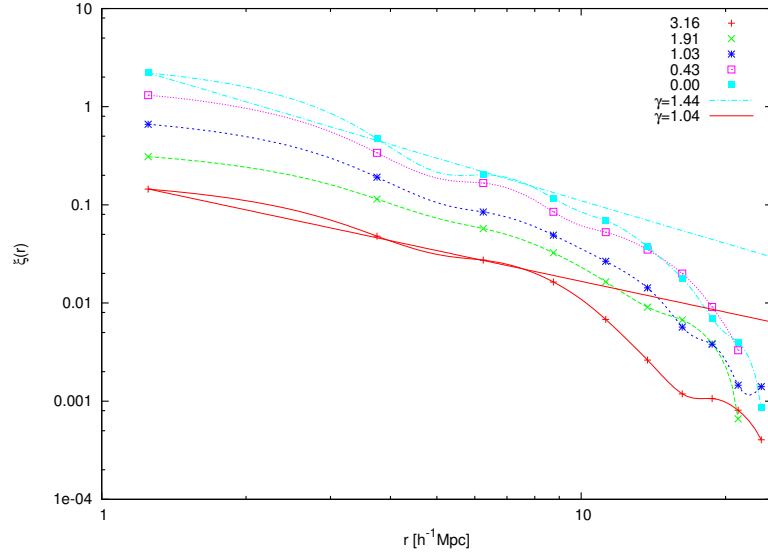


Figure 3.13: Correlation functions for dark matter in the simulation SFOF03 at different redshifts

To compute the correlation function we used the estimator

$$\xi(r) = \frac{DD(r)}{RR(r)} - 1 \quad (3.17)$$

Then we build bins around a group of particles and compute $DD(r)$ as the number of counts of particles with separations in the interval $r + dr$, and $RR(r)$ the number of counts in each bin associated with a random density distribution. Figure 3.13 shows the correlation function for dark matter computed as mentioned in the past lines. Note how the slope of the curve still being nearly the same for all curves for radius less than $10 \text{ Mpc } h^{-1}$. Straight lines show a power law

$$\xi(r) = \left(\frac{r}{r_0}\right)^\gamma \quad (3.18)$$

fitted to data in these interior radius, giving the power index $\gamma = -1.44$ (red line) and $\gamma = -1.04$ (cyan line). Figure 3.14 shows the correlation function computed for halos at different snapshots, note how the shape of the correlation function changes with time, specially from $z = 0.43$ to $z = 0.0$ where there is a strong jump in the properties of the function.

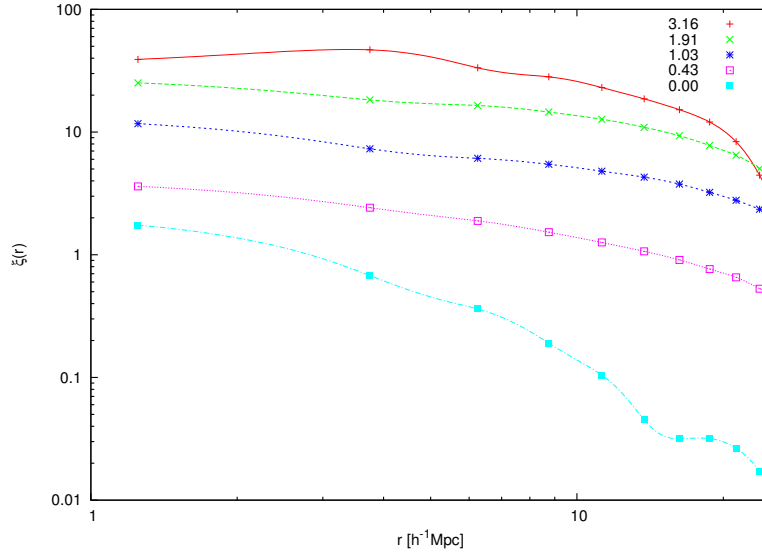


Figure 3.14: Correlation function for halos at different redshifts.

As will be the strong assumption in the next chapter, galaxies are believed to be tracers of the dark matter distribution, but sometimes there are reasons to think that not always the baryonic matter traces the distribution of matter in the universe. To quantify this deviation, the bias factor is introduced as a relation between the correlation function of the underlying dark matter distribution and the correlation function associated with galaxies through the relation

$$b^2 = \frac{\xi_{hh}(r)}{\xi_{dm}(r)} \quad (3.19)$$

where b is the bias factor and $\xi_{hh}(r)$ and $\xi_{dm}(r)$ are the correlation functions for galaxies and dark matter respectively. Figure 3.15 shows the results of the computing the ratio $\xi_{hh}(r)/\xi_{dm}(r)$ as an approximation for the bias factor at various radius and redshifts.

As in Bett et al. 2007, we compute the bias parameter as the constant normalization which minimizes

$$\chi^2 = \sum_{i=1}^n \left(\frac{\xi_{hh}(r_i) - b^2 \xi_{dm}(r_i)}{\sigma_{hh}(r_i)} \right)^2 \quad (3.20)$$

where σ_{hh} are the errors in the calculation of $\xi_{hh}(r)$ associated with poisson fluctuations, and the minimization is done in the domain for which $\xi_{hh}(r) > 0$. We did this minimization for $z = 0$ and find that for this redshift $b = 1.06$, which is in good agreement with other estimations.

3.5.3 Spin Parameter

One of the most important physical parameters computed for halos is the spin parameter λ , which quantifies the ratio between the angular velocity of the system and

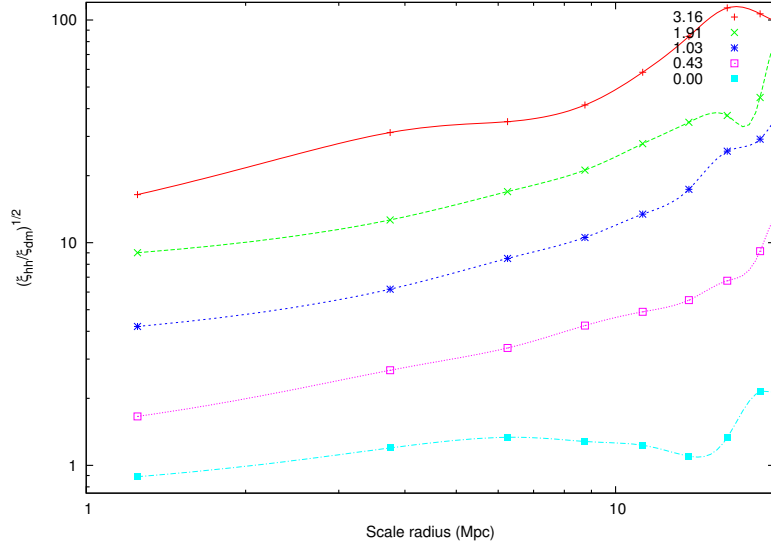


Figure 3.15: Ratio $\xi_{hh}(r)/\xi_{dm}(r)$ for different values of redshift and r

the angular velocity needed to have rotational support. As with the density contrast we used our three simulations SFOF to study the dependence of the distribution of the spin parameter with resolution and redshift.

In figure 3.17 we show the λ -distribution for halos at different redshifts and for different resolutions. Here we can see how for every resolution the shape of the distribution follows the same profile as well in redshift as in resolution. Figure 3.18 shows the distribution of the λ parameter for every simulations at different redshifts. In this figure is a little bit more clear the way in which the evolution of the distribution happens. It is interesting to note that the distribution does not evolve notably in time, in the sense that the mean value of the distribution is always nearly the same, but is interesting to note how for $z = 1.03$, 0.43 and 0 (curves blue, green and red respectively) becomes really stable, there is no a strong difference between the distributions, which does we think about some kind of equilibrium is happening to halos from $z \sim 1$ which does the distribution holds stable. Is also interesting to note that this behavior appears in all simulations, then it is a free-resolution phenomena.

In order to see in more detail what happens with the distribution of the spin parameter we investigate the evolution on time of the spin parameter for halos along time using for that the merger tree history of every halo (see section 4.1). We find that along the merger tree there is no a noticeable evolution for the spin parameter of halos. Figure 3.16 shows the distribution of spin parameters for all halos in the merger tree, note that in this graphic, not all halos are taken at the same redshift. Nevertheless the distribution of λ for halos at different redshifts still very close to the common distribution, with peak value near to $\bar{\lambda} \sim 0.05$.

According to Mo, Mao & White (1998) the spin halo distribution is given by

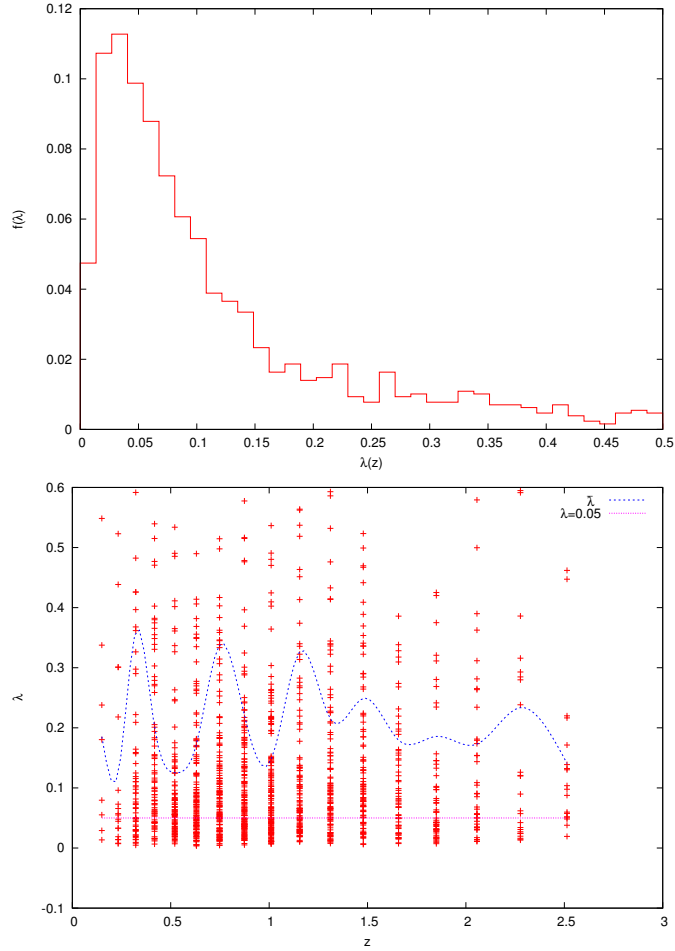


Figure 3.16: Up. Distribution of λ values for the history of a galaxy. Down. Values for λ obtained from the merger tree of one of the halos in the SFOF06 simulation. Points are values for λ at every halo at that z , blue dashed line is the arithmetic mean of these values for that redshift while the straight line marks the $\bar{\lambda} = 0.07$ value.

$$p(\lambda) = \frac{1}{\lambda \sigma_\lambda \sqrt{2\pi}} \exp \left[\frac{\ln^2 (\lambda / \bar{\lambda})}{2\sigma_\lambda^2} \right] \quad (3.21)$$

although for higher resolution other distributions has been recently proposed (Bett et al. 2007). We fit the distribution of halo spin parameter to that distribution

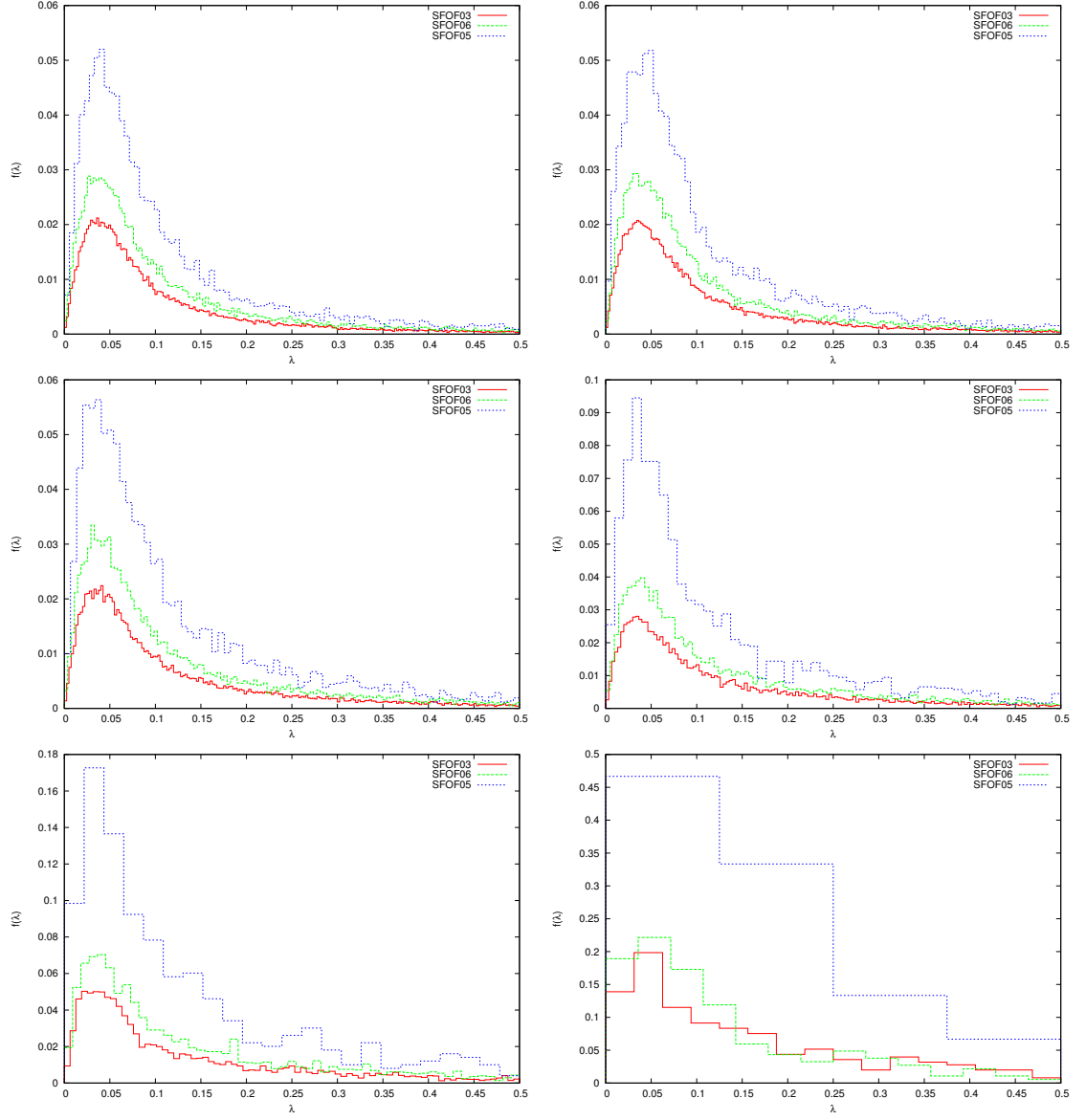


Figure 3.17: λ distributions for the three simulations at different redshifts $z=0, 0.43, 1.03, 1.91, 3.16$ and 4.94 counted from upper left to upper right panels

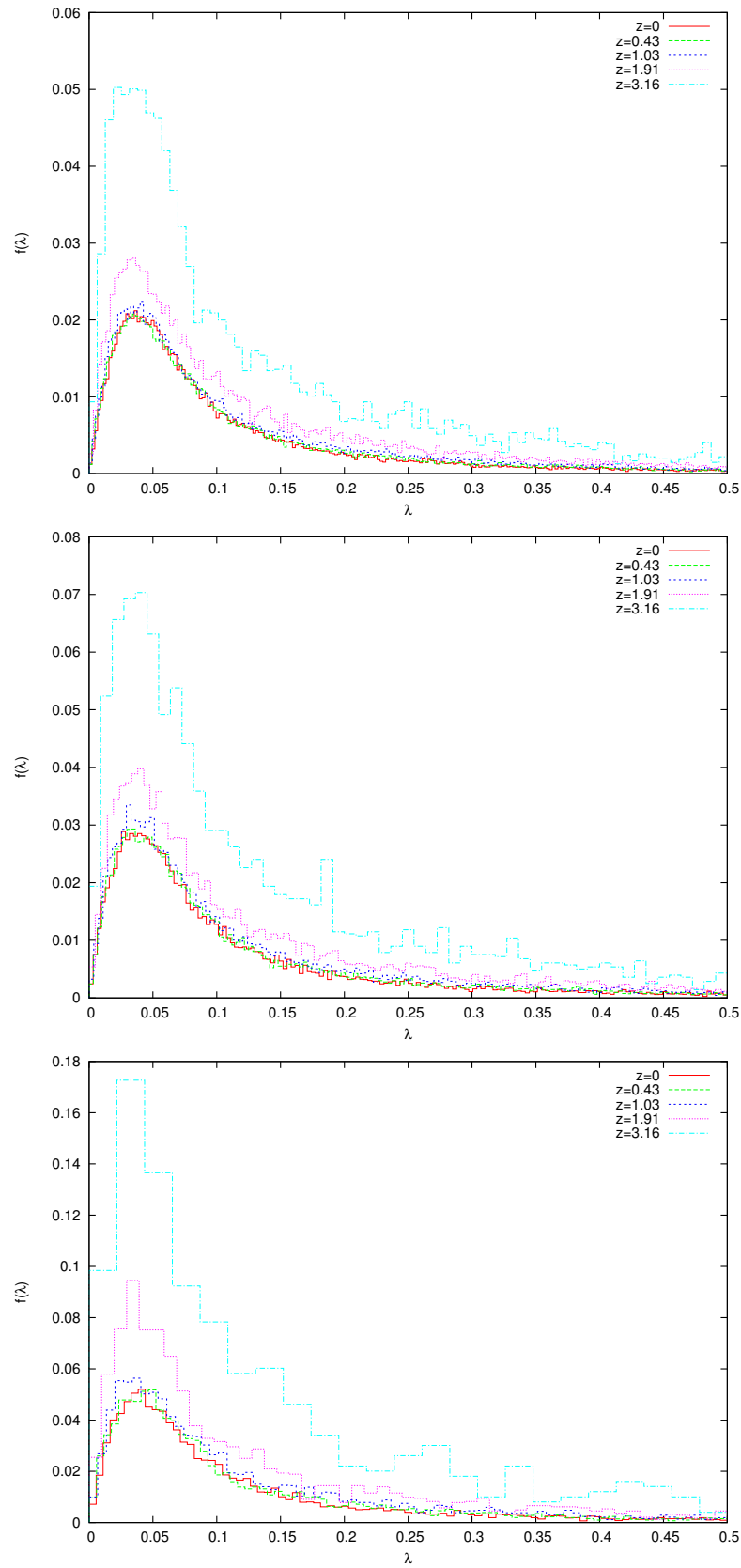


Figure 3.18: Distribution of spin parameters for halos in the three SFOF simulations for different redshifts

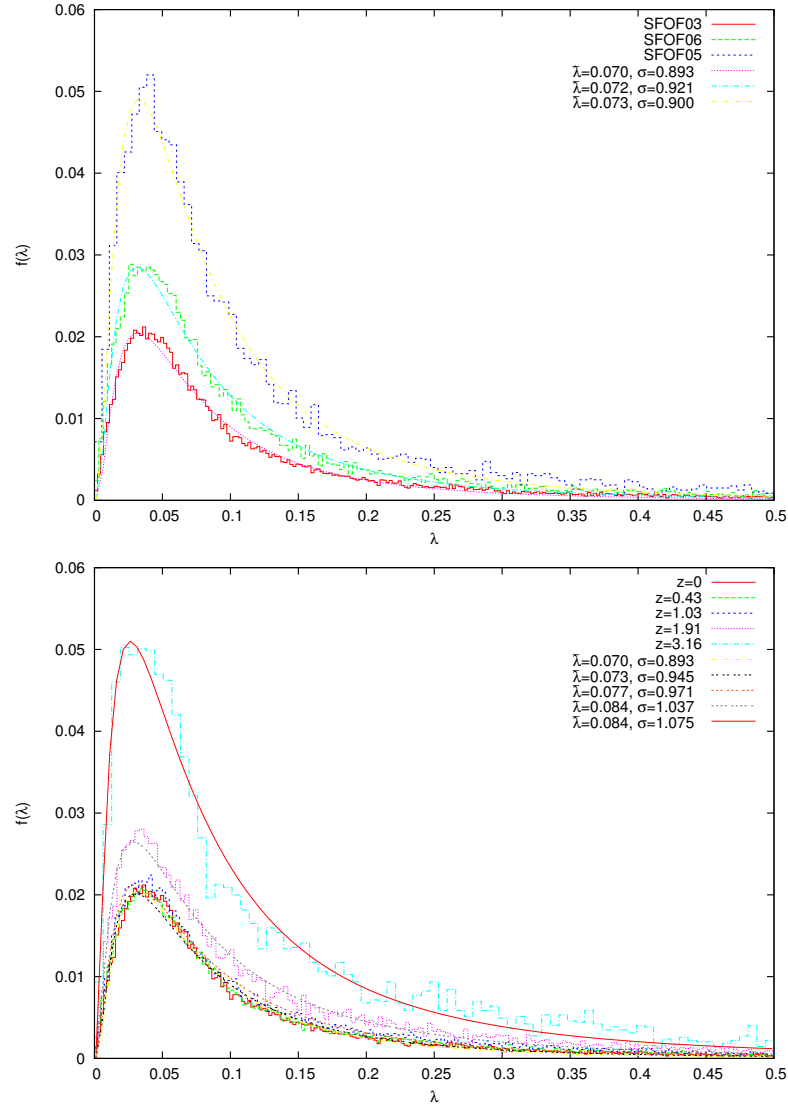


Figure 3.19: Fit of the distribution to the equation 3.21.

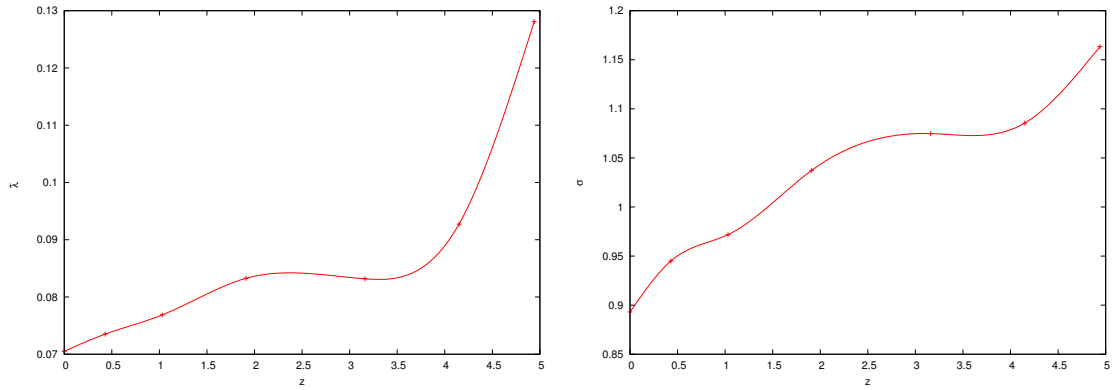


Figure 3.20: Temporal evolution of the parameters of the distribution of spin parameter for dark matter halos.

for the halos identified in the simulation SFOF03 and obtained the common mean of the distribution $\bar{\lambda} = 0.07$. In our results we observe a subtle variation in the parameters $\bar{\lambda}$ and σ_{λ} . Figure 3.19 shows a clear linear growing in σ with redshift, while the $\bar{\lambda}$ has a more complex behavior. It grows linearly from $z = 0$ to $z = 2$ and start another linear linear dependence with redshift from $z = 4$, but definitely we see increased values of $\bar{\lambda}$ with redshift.

3.5.4 Halo Mass Function

In order to describe the properties of the mass distribution of density fluctuations in the non linear regime, Prees & Schechter developed a mass function which describes that distribution for virialized halos and is in concordance with the ideas of the Λ CDM cosmology which is founded in the fact that small scale structures form at first, and then, from accretion from smaller perturbations, the big ones are formed.

Figure 3.21 shows the mass distribution for halos identified at different redshifts. Note how for the same redshift, the higher resolution simulation has richest population of low mass halos. It can be seen for example at $z = 0$, where the mass function has cut at $M \sim 2 \times 10^{11} M_{\odot}$ for the simulation SFOF05 and $M \sim 3 \times 10^{10} M_{\odot}$ for the simulations SFOF06 and SFOF03, which have a higher resolution.

An interesting thing appears in the limit of high mass (at $z = 0$ and $z = 0.43$) where all the distributions are cut at $M \sim 10^{13} M_{\odot}$. This equal cut for all simulations is related with the box size used for the simulations. Because the three simulations sample the same volume $((100 \text{ Mpc})^3)$, modes associated with density contrast are truncated by the volume of the box itself. To allow the formation of higher structures is needed the realization of simulations in boxes with higher volumes. In this case, although the SFOF06 has a higher resolution at low mass, the resolution at the high mass extreme is the same that the SFOF05 by the fact just mentioned.

Also the diagrams in figures 3.21 and 3.22 shows what we speak about the confidence of the mass distribution with the ideas of the Λ CDM model. Note how for high redshift the mass distribution is mostly dominated by low mass structures (curves for $z=4.94$ in 3.21 and yellow curves in figure 3.22), nevertheless obviously the high resolution simulation allow for a more dense population of halos at that low mass regime. Then, while z becomes more and more small (increasing cosmic time) the population of high mass structures increases, while also do that the number of low mass structures. This means that while accretion of low mass structures forms higher mass structures, the collapse of many low mass structures still happening, even at $z \sim 0$, that is, structures still forming until nearly recent cosmic times.

Press-Schechter proposal for the mass distribution is given by the function

$$N(M) = \frac{\bar{\rho}}{\sqrt{\pi}} \frac{\gamma}{M^2} \left(\frac{M}{M_*} \right)^{\gamma/2} \exp \left[\left(-\frac{M}{M_*} \right)^{\gamma} \right] \quad (3.22)$$

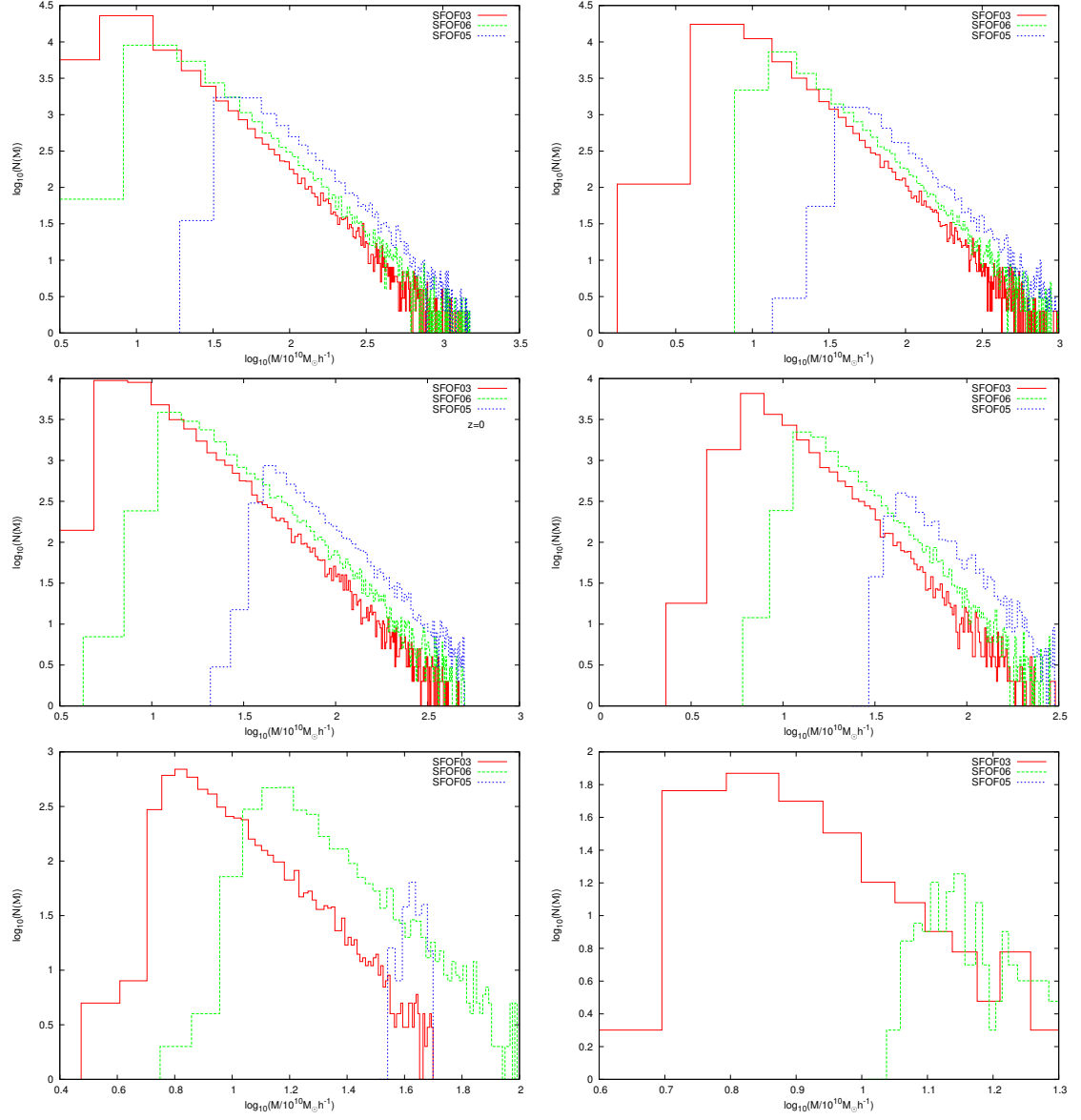


Figure 3.21: Mass distribution for the three simulations at different redshifts $z=0, 0.43, 1.03, 1.91, 3.16$ and 4.94 counted from upper left to upper right panels

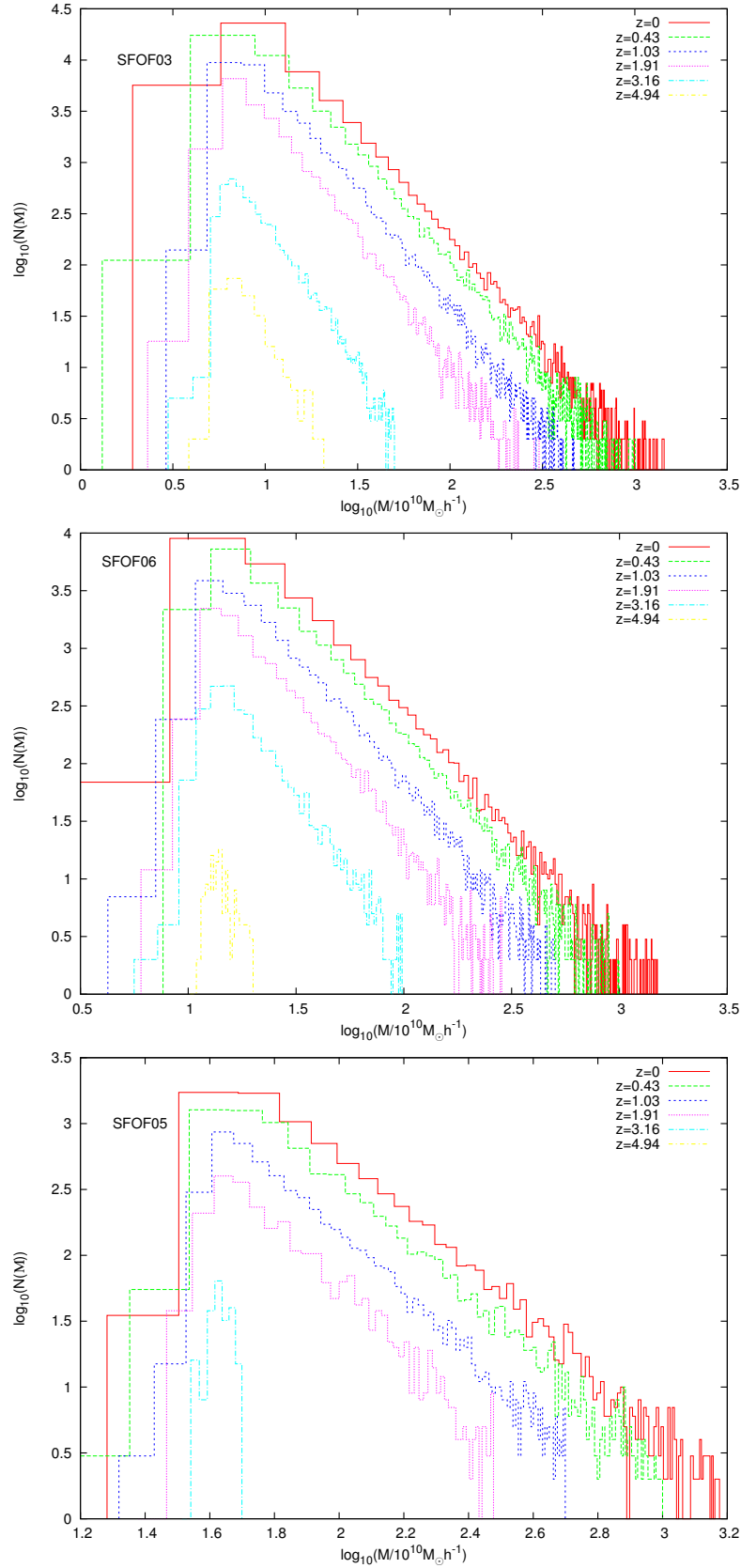


Figure 3.22: Distribution of subhalos identified as a function of the number of particles/subhalo for different values of the number of nearest neighbors used to the subhalo identification.

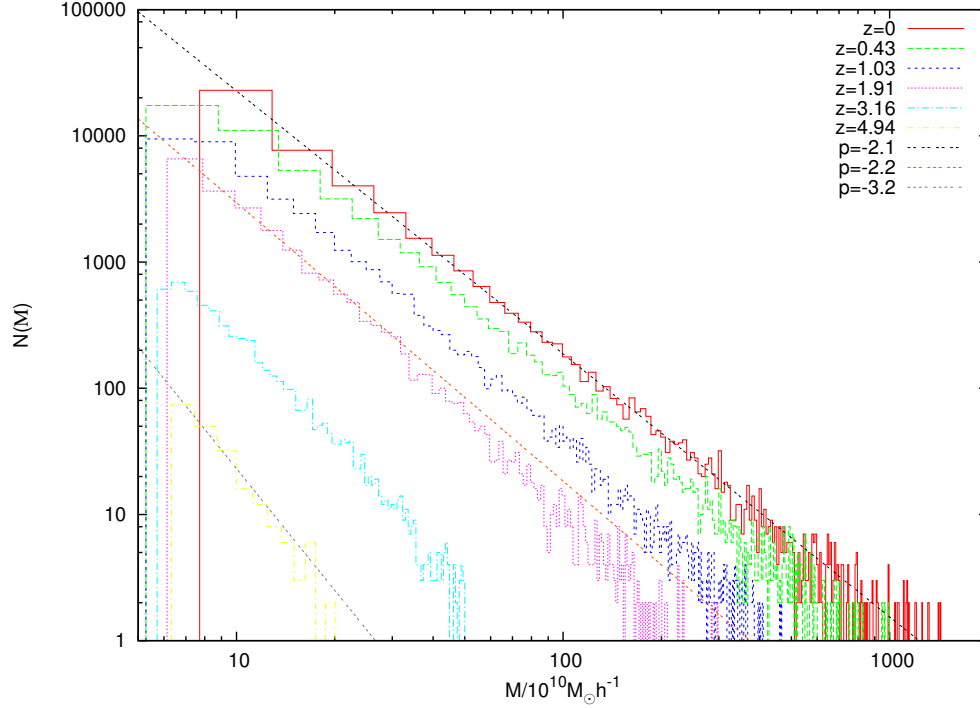


Figure 3.23: Fit to a power law function to the mass function.

Figure 3.23 shows the fit of the mass function to a power law, which correspond to the range of mass $M < M_*$, where M_* is the mass of the typical fluctuation which is collapsing at present epoch. We can see there how the slope of the lines (that is, the exponent of the power law) increases with redshift. At $z = 0$, $\gamma = -2.1$, at $z = 1.92$ $\gamma = -2.2$, while at $z = 4.94$ $\gamma = -3.2$.

3.6 Details of the Code

All we have presented in this chapter has been carried out through computational work. We start with the results of the cosmological Nbody simulations, and as input, we use every snapshot to identify FOF halos, substructures, and compute the properties of every halo. Here we give a very brief detail about the implementation of the procedures in our code **GalCos:Galaxies in Cosmology** which is a tool used to identify halos, compute its properties, build merger trees and study the evolution of galaxies in those halos through the use of semi analytic recipes. The part of the code related with this chapter is GalCos, the next chapter we will see how to implement our SAM in GalCosTree, which is the part of the GalCos code that computes merger trees and computes the evolution of galaxies.

General structure of data and the code GalCos is a serial code, part of the itself GalCos code, we used it to identify halos and compute halo properties.

We define a set of data structures to storage data of halos and particles in order to

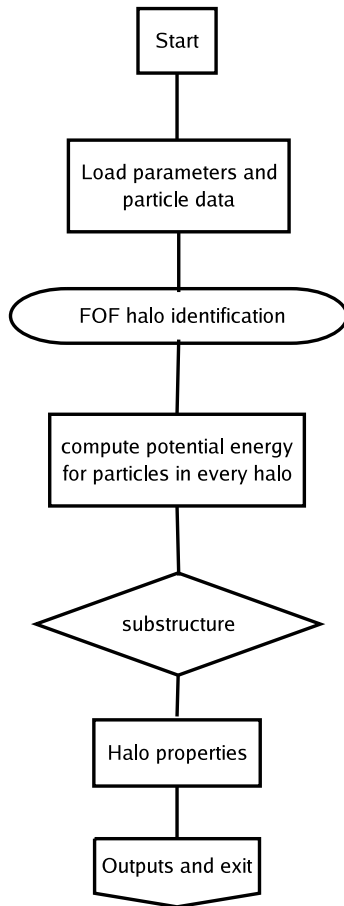


Figure 3.24: Flow chart of the GalCos halo identification and properties code.

compute the different quantities needed in the work. We basically define structures for particles and halos storage. Tables 3.3 and 3.2 detail the structures and memory required for every member of the structure.

We then load in memory data from the input snapshot, and used the FOF tool of the NbodyShop to do a first and fast FOF halo identification. Then, for every FOF halo we compute the potential energy of every particle in that halo (does not matter if it is not bound) and passes it to a routine that examines in detail the FOF halo, as mentioned in section 3.3 to identify substructure in that halo. Then we compute the properties for every halo and then write data to disk. Figure 3.24 shows a flow chart of the code.

3.7 Conclusions

We performed a series of cosmological Nbody simulations, identify structures in these simulations and compute some interesting and useful physical properties of these halos.

Quantity	size	Description
Mass	float	Total mass of the halo.
Position	float($\times 3$)	Position of the center of the halo
Velocity	float($\times 3$)	Velocity of the center of the halo
CM position	float($\times 3$)	Position of the CM
CM velocity	float($\times 3$)	Velocity of the CM
Sub halo mass fraction	float	Total Mass of subhalos
Half mass radius	float	Half mass radius of the DM halo
NumberOfSubhalos	float	Number of subhalos identified
Total kinetic energy	float	
Total potential energy	float	
Radius	float	Distance of the most external particle to the halo's center.
ID center halo	int	ID of the particle located at the center of the halo
Nmembers	int	Number of particles in the halo
ID cluster	int	Identification number of the halo
Halo particles	float($\times N$)	Array storing the ID of every particle in that halo
Rvir	float	Virial radius
Mvir	float	Virial mass
Vvir	float	
Total Energy	float	
Total angular momentum	float	
λ	float	Spin parameter
subhalos	struct halo	Array of pointer pointing to the subhalos in that halo

Table 3.2: Data structure for halo storage

Quantity	size	Description
Mass	float	Mass of the particle.
Position	float($\times 3$)	Position of the particle
Velocity	float($\times 3$)	Velocity of the particle
Kinetic energy	float	
Potential energy	float	
ID	int	ID of the particle
ID cluster	int	ID of the halo which contains the particle

Table 3.3: Data structure for particle storage

We presented a modification for the SUBFIND method for identification of substructure that uses the potential instead of the density of particles as parameter to trace substructure in FOF halos of cosmological N-Body simulations. We prove the method operates producing good results in the identification of halo substructure.

Our implementation avoids the computing of the SPH density, which some times, for large number of particles becomes a hard task, and uses the fact that potential energy must be computed in any case to evaluate binding of structures, providing a more efficient and memory cheaper method for substructure identification. Also, because we used the potential to identify substructure, the method is easily parallelisable, in spirit of the available techniques to compute gravitational effects in this way.

The method presented, like SUBFIND, allows for the hierarchical detection of substructure in substructure, allowing an appropriated map of the mass assembly hierarchy.

We showed the response of the method to variations in the parameters, where we find as a fiducial NGB value, no less than 32 particles to allow the detection of strong clustered structures and avoid fluctuations associated with the discrete mass distribution with which we work in N-Body simulations.

We can see from section 3.5.1 how the resolution of the simulations strongly affects the properties of structures that are formed in our simulations. Increased resolution simulations allow simultaneously the formation of small size high density contrast structures, but also allow the formation of a more spread population of density perturbations.

Omitting resolution effects we can see that for $z > 0.5$ the distribution of density contrasts $p(\Delta)$ could be represented by a lognormal distribution. For values $z < 0.5$ this approximation is not applicable. Also, we can see from our simulations that in fact, for high z , structures are formed preferably with low density contrast, but once

redshift start to decrease, the distribution shifts toward the region of high density contrast, then at low values of z more dense structures are formed. Once again, the value of the peak distribution associated with the highest density contrast allowed to appear in a simulation depends of the resolution of the simulation.

From section 3.5.3 we can see how the distribution of the spin parameter is independent of the resolution of the simulations. Even, when considered the distribution for different redshifts, just a subtle evolution in to the shape of the distribution can be seen (see figure 3.20) in the form of an increasing of the mean of the distribution $\bar{\lambda}$ and a broadening of the same. The reason why this parameter evolves very slowly in time could be related with the quantities involved when computed λ . Because these quantities are related with the bound nature of the halos, they must produce this slowly changing distribution. Could be possible that computing λ over not bound halos the distribution shows a different behavior in time. We did the exercise to compute this situation, and effectively, although the distribution looks like a log-normal, and the evolution is not excessive, there is a really noticeable change in the behavior of the $p(\lambda)$ with redshift for that distribution of unbound halos, which support our suggestion.

We show that in our simulations the distribution of the spin parameter fits quite well to the proposed lognormal function, and our results for the moments of that distribution are in good agreement with previous works, when the mean of the distribution is near to $\bar{\lambda} \sim 0.07$. Very interesting is the situation exhibited in figure 3.19 where we can see how for $z < 1.03$ the three curves are very coincident, suggesting some kind of convergence of the population of halos from $z = 1.03$ to a equilibrium situation.

Finally, the analysis of section 3.5.4 shows how our simulations are in good agreement whit the Press-Schechter formalism and with the entire Λ CDM cosmology, which can verified observationally. Note how, once again, the resolution affects the shape of the PS distribution. Will be better to realize high resolution simulations in order to allow the curve to grow in to the low mass range (allowing the description of low mas galaxies), but also is needed to realize simulations of higher volumes if one wants to describe in complete way the formation and properties of very large structures.

Star Formation and Semi Analytic Models of Galaxy Formation and Evolution

As mentioned before, galaxy formation is a complex process that involves a huge quantity of physics, making it a highly complex nonlinear event, which is very difficult to study analytically or numerically. Lets see why is needed the application of SAM (Semi Analytic Models) to describe the process of galaxy evolution.

Because the galaxy formation happens mostly in the nonlinear stages of the accretion of mass in the cosmic structures, we are unable to describe analytically the process of mass assembly in the galaxies. Almost, because galaxy formation does not involves only the process of mass accretion, the analytic description is very hard. For example, there are no ways to describe in detail the global effect of the luminous background in the interstellar gas in a galaxy. The effect of magnetic fields is also a difficult task to be developed under just analytic procedures. The dynamics of the gas is itself a hard work, that in real galaxies can be described with limited results under analytic procedures. And one of the most complex process describing the galaxy formation, star formation, can't be studied under detailed analytic descriptions: Astrophysics gives a detailed description of the process of formation of individual stars, even with strong observational support, making the formation process of a individual star (that is, a model!) a very complete description. But when passing to real world, when stars in galaxies form in groups, the environmental effects affect in strong way the process of star formation, making the global star formation in galaxies a hard procedure to be described in detail.

Numerical descriptions of the star formation (Springel 2000, Yepes et al. 2000) in galaxies or in cosmological simulations are also limited because the limited dynamical range of simulations. Because star formation process (and many process associated with the gas dynamics) involve spatial and mass domains that are well below the resolution level of Nbody and hydrodynamical simulations, the description of this kind of process in such simulations must be done through a series of approximations that impede the full development of a model for galaxy formation.

In order to overcome the problems involved in the description of the process of galaxy formation, two methods have been developed, the first one implies the development of full Nbody+hydrodynamical cosmological simulations, in which initial conditions are generated taking in to account the distribution of dark matter and baryonic matter in the form of gas. This kind of implementation, although being the ideal approximation, has several disadvantages. Simulations are very very expensive in terms of the computational requirements, while also are strongly limited in the range of cosmic coverage. Because this kind of simulations require a very high resolution in order to give good results in the hydrodynamical description of the process, the cosmic volumes simulated must be considerably small, which implies a problem of lost cosmological background events, and also an important lost of statistics.

The second method implies the realization of only Nbody dark matter simulations, in which the structures are assembled just as aggregations of dark matter, in which, once the Nbody simulation has ended, the baryons are located at “hand” according to cosmological mass distributions, and then, using the merger trees of halos to follow the evolution in time of the assembly history of halos, one follows the temporal evolution of galaxies in those halos, including through averaged descriptions, the evolution of those baryons, and then the evolution of the galaxy, in which is known as a semi analytic model (SAM) of galaxy formation.

We give in this chapter a brief description of our implementation of a SAM, the development of the merger tree histories of dark matter halos and results we obtain in the analysis of the star formation in galaxies according to our model.

4.1 Merger Trees

In order to build the merger tree of halos we follow an approximation similar that proposed by Haton et al. (2004). Suppose we have a halo H_a at redshift z_a and a halo H_b at redshift z_b whit $z_a < z_b$, then, halo H_b is progenitor of H_a if both halo share almost one particle. This election allows at every halo to have more than a descendant, allowing us to take in to account dynamical and numerical effects (tidal striping, evaporation, violent numerical relaxation, etc) that broke a halo at z_b into many fragments at z_a , that will be incorporated in to different halos at that redshift.

In our implementation we start at the snapshot in z_a and run over every halo in that snapshot. On each halo we loop in the snapshot at z_b over all halos in that snapshot looking for every halo which have almost one common particle with the halo in z_a , and then build the merger tree. In order to allow that every level of the halo have many branches, we used a non binary tree structure. A binary tree structure allow every node in the tree to have almost two subnodes. In a different way that with the binary tree, in a non binary tree every node can have an arbitrary number of subnodes, this will allow us to register an arbitrary number of parent halos in the

structure, although it is more complicated to use and too complicated to implement a walk, the non binary tree allow us to store the merger history in an appropriated way that next will be used to follow the evolution of galaxies in halos in that tree.

Figure 4.1 shows a merger tree for one of the halos (not the most massive) in the simulation SFOF06, $z=0$ is at the top of the tree and increase logarithmically at lower levels. Note how the hierarchy of the trees subdivides it itself, and note how some nodes just appear at some redshift, that is, not all the halos appears at the same redshift z_{start} , and even, at very low values of z there are many halos that are just joining to the tree.

4.2 Semi analytic model of galaxy formation

Our semi analytic model used to study galaxy evolution include different process:

- Baryonic mass allocation
- Radiative cooling of hot gas in the galaxy.
- Feedback from supernovae explosions
- Star formation
- Galaxy mergers
- Photometric evolution

Here we will describe in detail every approximation we use to model each physical process.

4.2.1 Hierarchical Distribution of Galaxies in Halos

Some authors gives hierarchical position at every galaxy identified in a halo according to the distribution of structures in a halo as central galaxies, halo galaxies or satellite galaxies (Kang et al. 2005, Springel et al. 2002). Because our simulations are not of an overwhelming resolution and following a more natural track of galaxy evolution, we just have two hierarchical position, central galaxies and satellite galaxies.

To us a galaxy is then associated with a node in the merger tree which is also related with a halo which has not experienced merger which has deleted it from the merger tree. A satellite galaxy is a galaxy in a halo that for the evolution of the merger tree has merged in to other, more massive halo, thus, in our prescription, satellite galaxies are not associated with any node in the merger tree. Because the nature of our description, every galaxy in our model born as a central galaxy.

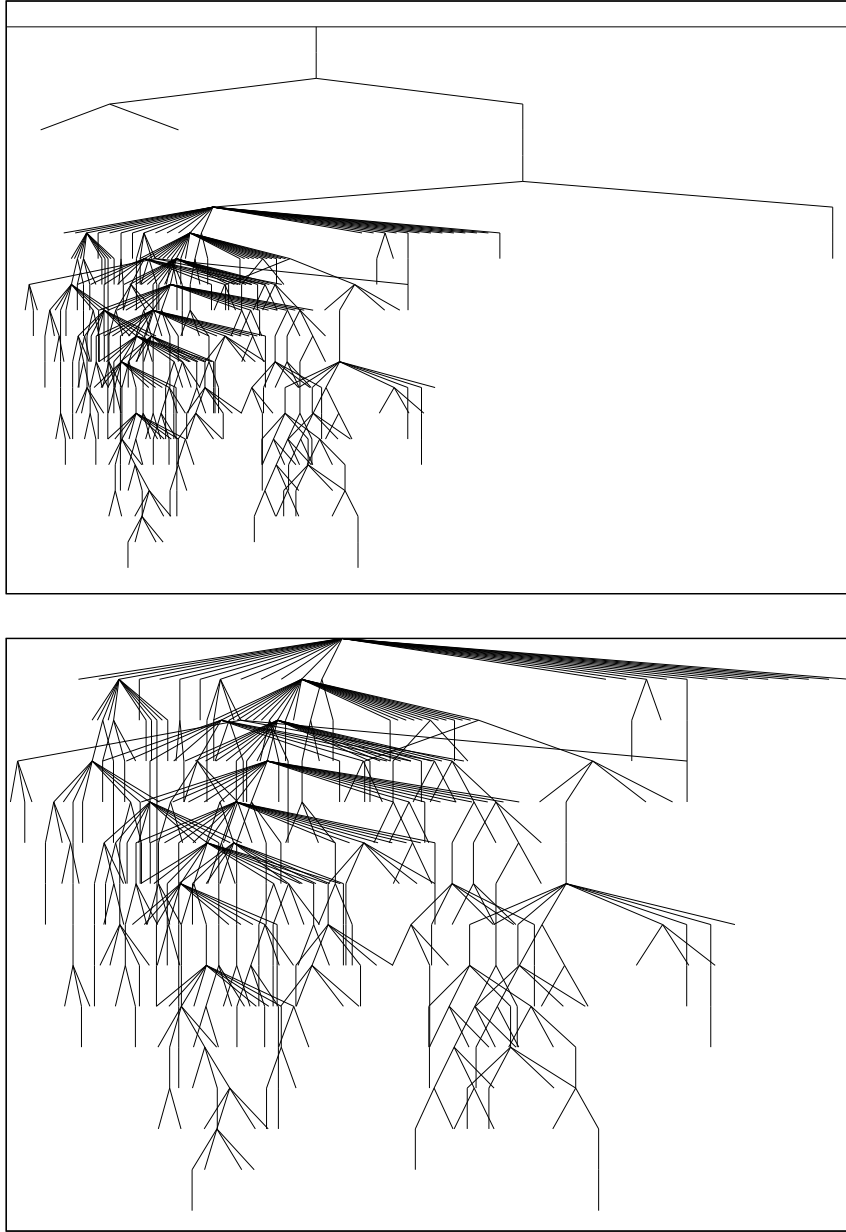


Figure 4.1: Merger tree for a halo in the simulation SFOF06. At the top is the entire tree while in the bottom an increased map of the densest branch of the tree

This stratification of galaxies along the merger tree will play a crucial role in the process of star formation in galaxies because for example satellite galaxies has not cooling enabled. Here we propose a variation to the effective definition of satellite galaxy, to us a satellite galaxy (in the sense of enablement of cooling) will be driven by mass considerations.

4.2.2 Baryonic Mass Allocation

For every halo identified in the simulation, we compute the corresponding hot gas mass as

$$m_{\text{hot}} = f_b M_{\text{vir}} - \sum_i [m_*^i + m_{\text{cold}}^i + m_{\text{eject}}^i] \quad (4.1)$$

where f_b is the fraction of baryons per halo $f_b = \Omega_b/\Omega_0$, according with cosmological parameters of mass distribution and the sum runs over all galaxies in a halo. M_{vir} is the virial mass of the halo, and m_*^i , m_{cold}^i and m_{eject}^i are the mass of stars, cold gas mass and ejected mass of the i th galaxy respectively.

4.2.3 Radiative Cooling of Hot Gas

In order to describe cooling we will follow the ideas of White & Frenk (1991) and will allow cooling of hot gas mass in a galaxy assuming that this is distributed as an isothermal sphere

$$\rho_g(r) = \frac{M_{\text{hot}}}{4\pi R_{\text{vir}} r^2} \quad (4.2)$$

Which is according with X ray observations of hot gas in clusters of galaxies. We define the local cooling time of hot gas as the ratio of the specific thermal energy of the gas and the cooling rate per unit volume

$$t_{\text{cool}}(r) = \frac{3}{2} \frac{\bar{\mu} m_p k T}{\rho_g(r) \Lambda(T, z)} \quad (4.3)$$

where $\bar{\mu} m_p$ is the mean particle mass of gas, k is the Boltzmann's constant, T is the temperature of the gas and $\Lambda(T, z)$ is the cooling function. In our implementation we don't follow chemical evolution, and used the cooling functions from Sutherland & Dopita (1993) for solar metalicity.

The cooling radius is defined as the radius at which the halo cooling time is equal to the time for which the halo has been able to cool quasi-statically, thus, as in Kang et al. (2004) (hereafter KJMB), we used this time as the cosmic time at that redshift, and as done in Kauffmann et al. (1999) (hereafter KCDW) we set

$$t_{\text{cool}}(r_{\text{cool}}) = \frac{2}{3H_0(1+z)^{3/2}} \quad (4.4)$$

Thus the cooling rate (mass of gas cooled per unit time) for our isothermal distribution of gas

$$\dot{m}_{\text{cool}} = \frac{M_{\text{hot}} r_{\text{cool}}}{2R_{\text{vir}} t_{\text{cool}}} \quad (4.5)$$

For low mass halos, or for high redshift, the cooling time could be smaller than the age of the universe, then when the cooling radius is larger than the virial radius we chose for the cooling rate

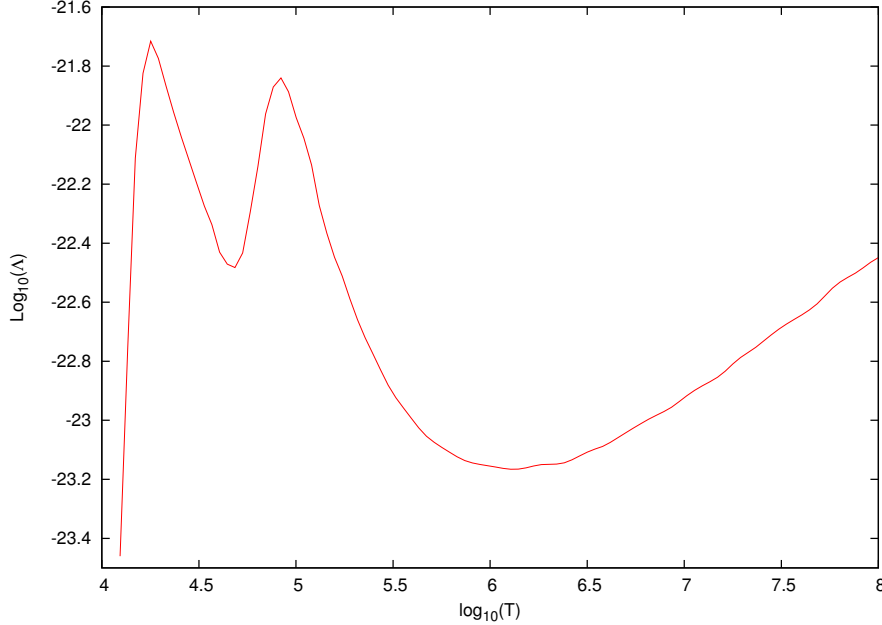


Figure 4.2: Cooling function according to Sutherland & Dopita (1993).

$$\dot{m}_{\text{cool}} = \frac{M_{\text{hot}}}{2t_{\text{cool}}} \quad (4.6)$$

Note that the first equation is related with the hot gas that can cools at twice of the cooling time, while the second one is the same that 4.5 when $r = R_{\text{vir}}$, that is, the gas takes t_{cool} to get cooled.

As shown in KCDW and KJMB, we assume that cooling in satellite galaxies is suppressed (in order to allow them still with cold gas at present redshifts), then star formation in that galaxies will happen until them gets completely depleted of cool gas.

4.2.4 Supernovae Feedback

Supernovae has prove to be an important source of energy to reheat the ISM, at the point that is one of the most important process on suppression of star formation in galaxies. Commonly, the energy released by supernovae per unit of solar mass is computed as $\eta_{\text{SN}} E_{\text{SN}}$, where η_{SN} is a factor depending of the form of the IMF assumed and E_{SN} is the mean energy released per supernovae and is assumed to be 10^{51}erg .

The energy released by supernovae explosions associated with Δm_* newly formed stars affects a fraction Δm_{eject} of the cold gas which is given by

$$\Delta m_{\text{eject}} = \frac{4}{3} \epsilon \frac{\eta_{\text{SN}} E_{\text{SN}} \Delta m_{*}}{V_{\text{vir}}^2} \quad (4.7)$$

Where ϵ is a parameter that quantifies the supernovae feedback efficiency.

This approximation gives the mass of gas reheated by supernovae explosion but not says nothing about what happens with that gas. There are commonly two different prescriptions for that final fate of the reheated gas. The first one, the *retention*, is one in which gas heated by supernovae feedback is reincorporated to the hot gas mass of the halo. The second one, the *ejection* scheme, considers that reheated gas is ejected out from the halo, to be reincorporated in to the halo past some time. As mentioned in KCDW or in Springel et al. 2001, both process are in good agreement with observations, tuning the process with the appropriated values for the parameters, then we will stay working in this work with the retention scheme.

4.2.5 Star Formation

We model star formation from cold gas as

$$\psi = \alpha_0 \frac{m_{\text{cold}}}{t_d} \quad (4.8)$$

where m_{cold} is the cold gas mass in the galaxy, t_d is the dynamical time of the galaxy, which we compute as the ten percent of the dynamical time of the halo ($0.1 R_{\text{vir}}/V_{\text{vir}}$) and the star formation efficiency, α is parametrized as

$$\alpha = \alpha_0 \left(\frac{V_{\text{vir}}}{220 \text{ km s}^{-1}} \right)^n \quad (4.9)$$

when α_0 and n are free parameters of the model that in general depends on the IMF, and this parametrization allows to control the star formation efficiency in high mass galaxies.

As mentioned in KCDW, we will suppress star formation in galaxies with $V_{\text{vir}} > 350 \text{ km s}^{-1}$ in order to match the observations of blue giant galaxies, but we will try with other values for the maximum circular velocity, while the star formation index will be assumed to be $n = 2.2$ for all our runs.

4.2.6 Galaxy Mergers

In the implementation of our SAM we follow the evolution and merger of galaxies through the merger tree. Every time a new galaxy is set up in the merger tree (that is, a node in the tree with no subnodes) it is initialized with a hot gas mass given by $f_b M_{\text{vir}}$ according with 4.1, then the accreted mass by the halo is only updated at discrete time steps. Every time a new snapshot is loaded M_{vir} , V_{vir} , R_{vir} , etc, are updated for the halo, then the hot gas mass fraction increases (or decreases) by accretion only every time a new snapshot is loaded.

When two or more halos merge in the merger tree, this not implies the immediate merger of the galaxies in these halos. When halos merge in the merger tree we then locate the most massive progenitor for the halo, such that the new galaxy (central galaxy) inherits all the properties of baryons from its most massive progenitor. Then, the remainder less massive galaxies becomes satellite galaxies. For every satellite galaxy we then compute its merger time around the central one (KCDW, KJMB, etc.) according to the dynamical friction approximation (Binney & Tremaine 1997) as

$$\tau = 0.5 \frac{f(\epsilon) V_c r_c^2}{C G m_{sat} \ln \Lambda} \quad (4.10)$$

Here $f(\epsilon)$ describes the dependence of τ with the orbital eccentricity ϵ , and following different author we will assume $\langle f(\epsilon) \rangle \sim 0.5$. V_c is the velocity of the circular orbit of the satellite which can be approximated with V_{vir} , r_c^2 is the radius of the orbit, that will be approximated by R_{vir} , C is a constant with value $C = 0.43$, m_{sat} is the mass of the satellite, that will be approximated by the virial mass of the galaxy at the last time it was a central galaxy, and $\ln \Lambda$ is the Coulomb logarithm which we approximate as $\ln \Lambda = 1 + m_{vir}/m_{sat}$.

Every time a new satellite is added in to a halo, its merger time is computed, and for old satellites in the same halo, τ is updated every time step, decreasing by Δt its value. Once $\tau \leq 0$ the galaxies merge and the properties of the remnant will depend of the nature of the merger itself. If the merger is a minor merger ($m_{sat}/m_{main} \leq 0.3$), then all the stars of the satellite are put in to the bulge of the main galaxy and the hot and cold gas are added to the main galaxy. In a major merger ($m_{sat}/m_{main} > 0.3$), following the nature of this kind of process, all the cold gas in both galaxies is instantly burned at a constant SFR to form a spheroidal component (the bulge component in this case) This result is supported by observations of violent merger and simulations of major merger of galaxies.

4.2.7 Photometric Evolution

Although we don't do mention to results related with photometric properties of galaxies in this work, we mention how to compute the photometric evolution of galaxies in the SAM.

The SED S_ν of the galaxy at a given time step is computed as

$$S_\nu = \int_0^t F_\nu(t - t') \dot{m}_*(t') dt' \quad (4.11)$$

Where we used the stellar population synthesis model of Bruzual & Charlot (2003) to interpolate F_ν .

4.2.8 Putting Everything Together

To start we divide the time between two snapshots in N_{steps} time steps, then, for every snapshot and for every halo in that snapshot we identify if the galaxy is just newly born or has a previous history. Then compute the available hot gas mas according to (4.1), and use equations (4.5), (4.7) and (4.8) to compute the properties of baryons in the galaxy. Then, for every galaxy we solve the set of equations

$$\dot{m}_* = (1 - R)\psi \quad (4.12)$$

$$\dot{m}_{cold} = \dot{m}_{cool} - \dot{m}_* - \dot{m}_{eject} \quad (4.13)$$

and

$$\dot{m}_{hot} = -\dot{m}_{cool} + \sum_i \dot{m}_{eject^i} \quad (4.14)$$

where we set $\dot{m}_{cool} = 0$ for satellite galaxies and the summation is over all the satellites around the galaxy. In these equations R is a parameter that quantifies the efficiency of the star formation process (this represents the fraction of mass recycled to the cold gas from stars through stellar winds) and is dependent of the IMF chosen in the model. $R = 0.35$ for Salpeter IMF while $R = 0.4$ for Scalo IMF.

This procedure allow us to evolve the different components of mass on baryons in every galaxy, and allow us to compute S_ν for every galaxy, while allows to follow the mergers and its effect in the evolution of galaxies.

4.3 Results of our model

4.3.1 Global Evolution of Baryons

We devote our implementation to the description of the star formation rate in galaxies, and cosmic star formation rate in galaxies. No mention of photometric results is done in this work in spirit to prove the star formation rate independently of any other factors.

We ran a set of simulations over which we change parameters related with the star formation process. We modify the velocity of truncation for the SFR V_{cut} , varying it at 300, 350 and 400 km/s, in order to see its effects on the SFR history. Then we ran the same set of parameters, but looking for the effects of this suppression factor we change in three distinct runs the value of V_{cut} , and allow the possibility to hold it as a free parameter of the model.

Also we propose a different criterion for suppress cooling in galaxies. Commonly, in many SAMs, every satellite galaxy is unable to cool gas, which in principle is not completely true, any galaxy is experiencing gas cooling, although the efficiency

Name	R	α_0	ϵ	n	η_{SN}
SFRVcut_300	0.35	0.1	0.1	2.2	6.3×10^{-3}
SFRVcut_350	0.35	0.1	0.1	2.2	6.3×10^{-3}
SFRVcut_400	0.35	0.1	0.1	2.2	6.3×10^{-3}
SFR_scalo	0.4	0.1	0.2	2.2	5.0×10^{-3}
SFR_sat	0.35	0.1	0.1	2.2	6.3×10^{-3}

Table 4.1: Table of parameters and simulations in the study of the SFR

of such cooling is subject to different factors. We tries to change this prescription and propose a criterion for gas cooling in satellites associated with the mass content in the galaxy. If the galaxy has a mass less than M_{cut} we turn off the cooling in the galaxy, does not matter if it is central or satellite galaxy. This will allow us to activate star formation in low mass galaxies, as observed in the Local Group at the Large Magellanic Cloud or the M33 galaxy, as an example.

All our runs used SFR parameters related with the Salpeter's IMF, but we choose another set of parameters associated with Scalo's IMF, which gives noticeable distinct results in the global SFR when compared with those we obtain with Salpeter.

We define in this work a global quantity as the sum of the quantity at every redshift per unit of comoving volume, then, we define the global cold gas mass function as

$$M_{cold_G}(z) = \frac{1}{V_c} \sum_i M_{cold}^i(z) \quad (4.15)$$

and every global quantity X will be then computed as

$$X_G(z) = \frac{1}{V_c} \sum_i X^i(z) \quad (4.16)$$

where V_c is the comoving volume in the simulation and the sum runs over every galaxies at that redshift.

4.3.2 Cold Gas Mass

In figure 4.3 we show results of the simulations for the evolution of the global cold gas mass (solution to eq. 4.13) for a set of simulations at the same resolution. Note the difference in the curves for the Scalo and Salpeter IMFs. All curves shows nearly the same value for $z > 2.5$, and for $z < 2.5$ we have distinct branches, every one associated with every set of parameters: The Salpeter's IMF for the distinct variations, and the other one related with the Scalo IMF. It is clear from the figure that the Scalo IMF preserves less efficiently the cold gas mass, this could be doubt to a more efficient star formation process, or as will be seen after, associated with a most efficient feedback process.

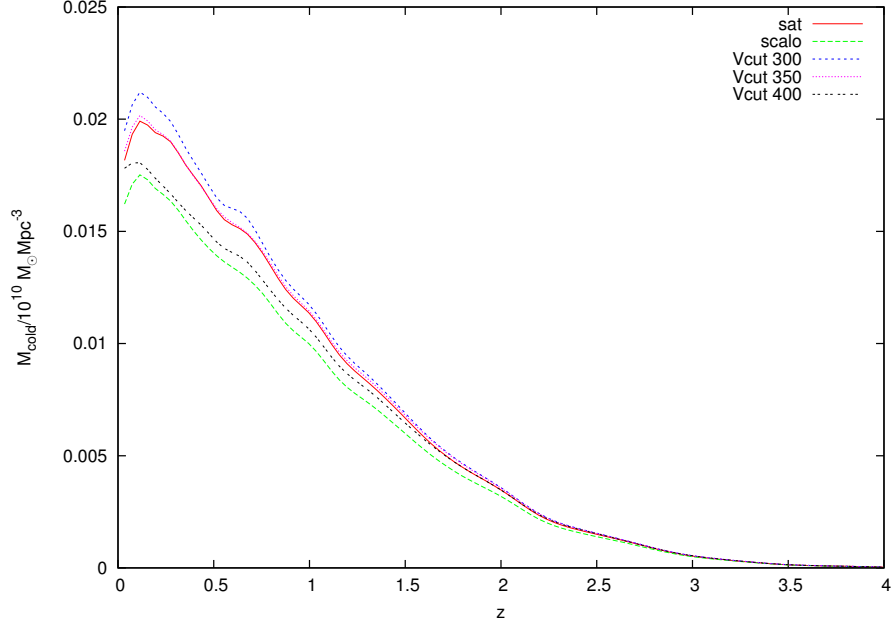


Figure 4.3: Evolution of the global cold gas mass in the simulation

Figure 4.3 also shows the variations in the global cold gas mass for different values of the V_{cut} , but it can be seen that for $V_{cut} = 300 \text{ km s}^{-1}$ there is a higher global cold gas mass content than that for $V_{cut} = 350 \text{ km s}^{-1}$ and $V_{cut} = 400 \text{ km s}^{-1}$. Also note that the differences between these three curves appears noticeably for $z < 1.5$, because the mass of structures for higher z is sufficient small to hold the circular velocity of halos below a common threshold.

It is clear that the available cold gas mass is inversely proportional to the V_{cut} parameter. The curves red and cyan are equal because they are ran with the same V_{cut} value. They are slightly different, but that differences are not very notables. That shows that in our results, the activation of cooling for galaxies more massive than M_{cut} produces not strong differences in the global cold gas mass content.

4.3.3 Cooling Rate

In our simulations the cooling rate \dot{m}_{cool} is hold constant between snapshot and snapshot, such that, nevertheless one could hope that as the cooling rate depends of the cooling time (and then of the cosmic time) and also depends of the available hot gas mass, the cooling function must change in some way in time. Figure 4.4 shows such evolution, and shows how this evolution depends of the different models we choose. Note how as was seen for the cold gas mass, the cooling rate has a maximum value near to $z \sim 0.7$. Once again note how the cooling is more efficient for the Scalo IMF, it could be surprising because the mass of cold gas available is lesser than that for Salpeter, but of course, when there is a lesser cold gas, then is a high hot gas mass fraction, then the cooling rate (which is directly proportional to M_{hot}) will be higher.

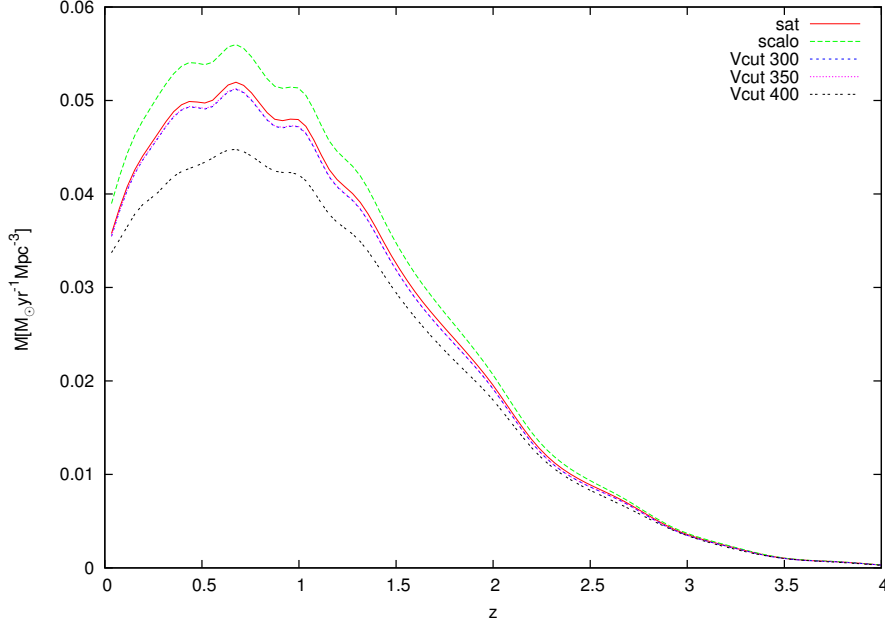


Figure 4.4: Evolution of the cooling rate with redshift

Also note that the curves are very quite coincident for the remainder models at $z > 2.5$, doing cooling independent of these parameters for that redshifts. Is interesting to note that the cooling function is equal for $V_{cut} = 300$ and $V_{cut} = 350$, which must means that the hot gas mass are equals for both simulations. This result show that for this simulations both limits operate very equivalently, such that one could work with any of the two criteria. Particularly, if resolution is increased the circular velocity of galaxies must be smaller (resolution increases the number of low mass structures most efficiently than the mass of the structures itself, doing the circular velocity distribution could decrease with resolution), then a choice of $V_{cut} = 300 \text{ km s}^{-1}$ could be justified. Once again note how the global cooling rate for the model with cooling enabled for satellites behaves in a very similar way that $V_{cut} = 300$, nevertheless this curve shows a subtle increasing in the global cooling rate when this criterion is activated, when compared with the standard one.

4.3.4 Reheated Mass by Supernovae Feedback

In our simulations $E_{SN} = 10^{56} \text{ ergs}$ was set according with previous works (KJMB, KCDW, etc) as the energy released per supernovae in to the ISM in a galaxy, note that this is a parameter independent of the IMF or other considerations (although it could depend of redshift, because the chemistry and properties of stars at higher z could drive to SN explosions with distinct feedback energy). We can see in figure 4.5 that the Scalo IMF is most efficient doing ejection of cold gas to the hot gas phase, although the supernovae energy is the same and the number of supernovae formed per solar mass η_{SN} is a little bit small than that for the Salpeter IMF. But

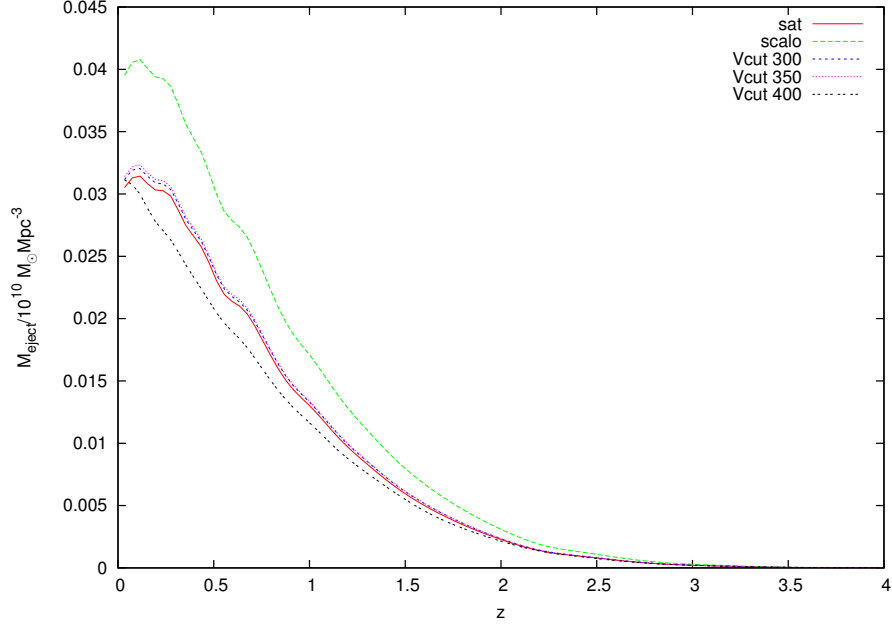


Figure 4.5: Ejected mass by supernovae feedback as a function of time

we can see in table 4.1 that the feedback efficiency ϵ_{SN} is twice the efficiency of the Salpeter’s IMF, doing the ejected mass higher.

As mentioned in past paragraphs, the global hot gas mass is larger for the Scalo IMF, which is in consonance with our previous comments about the global cooling rate and global cold gas mass for that IMF. Also note that once again, the behavior of the curve is very similar for $V_{cut} = 300$ and $V_{cut} = 350$, and also are observed some subtle difference related with the cooling enabled for satellites, as in the previous figures.

4.3.5 Hot Gas Mass

Although could be hoped that while redshift decreases the hot gas mass decreases by the increased number of stars in galaxies (and in fact, this could happen in some “isolated halos”) accretion of dark matter increases the fraction of baryonic hot gas mass in every halo, doing that the hot gas mass could grow with cosmic time. Also, as redshift increases, the number of structures identified in our simulations grows, then also the global hot gas mass fraction. That is just we are seeing in figure 4.6, which shows the global hot gas mass M_{hot} as a growing function of cosmic time. Note how in accordance with our previous paragraphs M_{hot} is larger for the Scalo IMF than that for the Salpeter models, but also note how the hot gas mass is the same for the remainder three models.

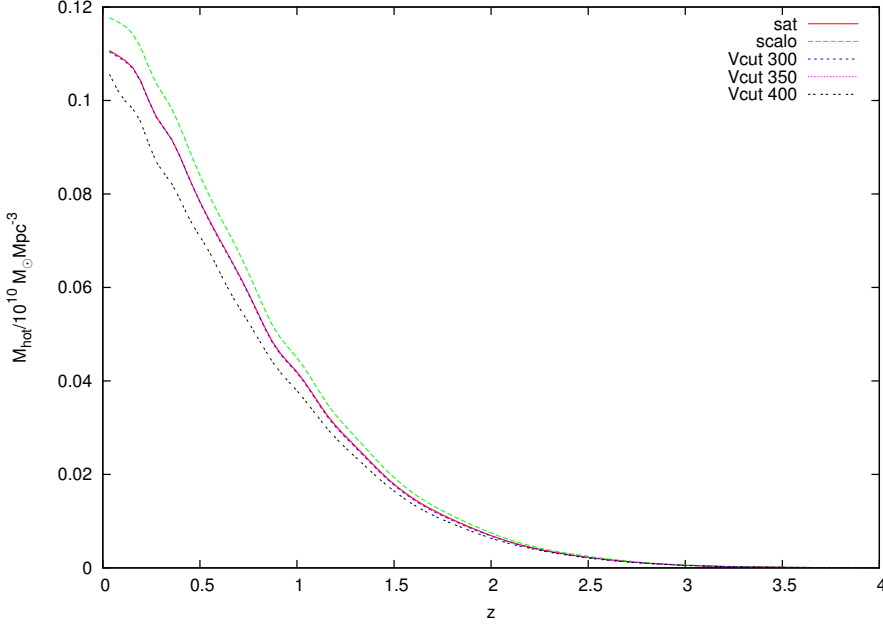


Figure 4.6: Global hot gas mass.

4.3.6 Stellar Mass

As well as in the past figures, we can see in figure 4.7 the different behavior on the global stellar mass of the curves for the two distinct IMFs. According to we observe in the previous figures, the Scalo IMF has an inferior ability to form stars, when compared with the Salpeter. As can be seen from the figure, although only subtle changes are observed for quantities related with curves $V_{cut} = 300$ and $V_{cut} = 350$ in the previous quantities, the slight differences between the curves drive finally to a noticeable difference in the global stellar mass.

Note also that in our model the stellar mass is contained in to two different regions. A peripheral region where stars are newly born (a disk) and a central region where stars are deposited after a merger happens (the bulge or the spheroid). Figure 4.7 does not take account for the mass contained in that central region, this just show the mass of newly born stars. Because this central region storages the mass associated with mergers, and as will be seen in next sessions, mergers are more frequent at low redshift, we hope that the total stellar mass (disk + spheroid) behaves like an always growing function, as must be hoped from experience.

4.3.7 Global Star Formation

Determination of observational measures of the star formation rate in the universe is a hard task. Commonly star formation is extracted from observations through the use of some spectral lines as estimators, such lines are strongly associated with the emission of light from the newly formed stars in a galaxy that have a no strong

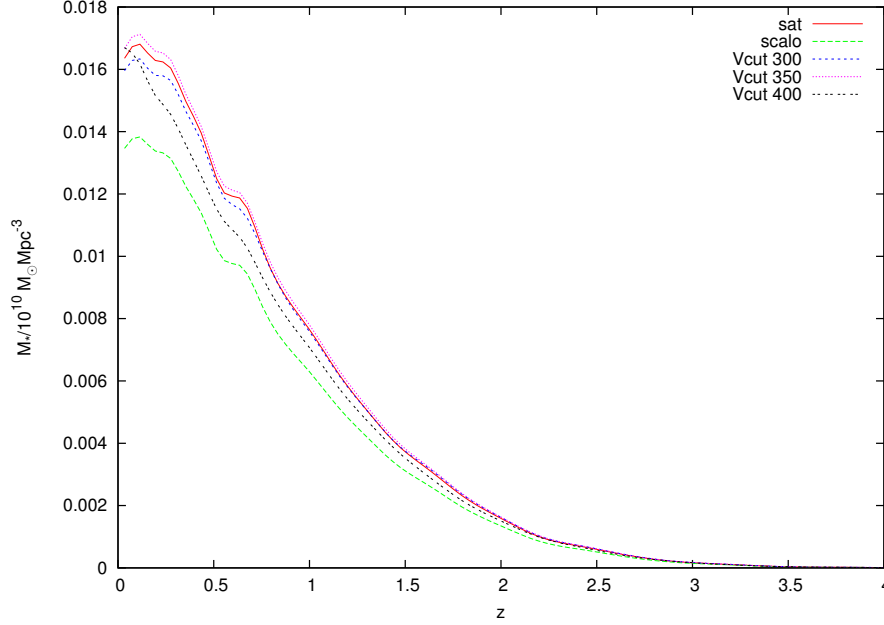


Figure 4.7: Global stellar mass as a function of redshift

influence of the environment in which they born, as some radio lines, IR lines, or $H\alpha$ lines. Using these estimators, star formation in galaxies can be computed through semi empirical relations that obey many observational trends, as for example the $H\alpha$ estimator which allow the determination of the star formation in a galaxy from the $H\alpha$ luminosity from

$$SFR = \frac{L(H_\alpha) M_\odot \text{yr}^{-1}}{9.40 \times 10^{40} \text{ ergs}^{-1}} \quad (4.17)$$

Where $L(H_\alpha)$ is the luminosity of the galaxy at $H\alpha$ line and SFR is the star formation rate indicated from that luminosity.

Along the last few ten years observations allow us to measure the star formation activity in galaxies, using many estimator spectral lines, including some ultraviolet lines, that for cosmological effects allow us to determine the star formation rate of galaxies until redshift $z > 5$ and recently deep sky surveys have observational resources to allow the determination of many well resolved spectral indicators which will enrich the data from observations for the cosmic star formation.

Observations (see references in 4.2) suggests that the cosmic star formation is a growing function from $z = 0$ until nearly $z \sim 2$ where the star formation density $\dot{\rho}_*$, and although the scatter of the data is not despicable, observations also suggest a decreasing function for $\dot{\rho}_*$ in the range $z > 2$, suggesting that there is some kind of star formation scale.

Our final objective in this part of the work was to study the conditions under which,

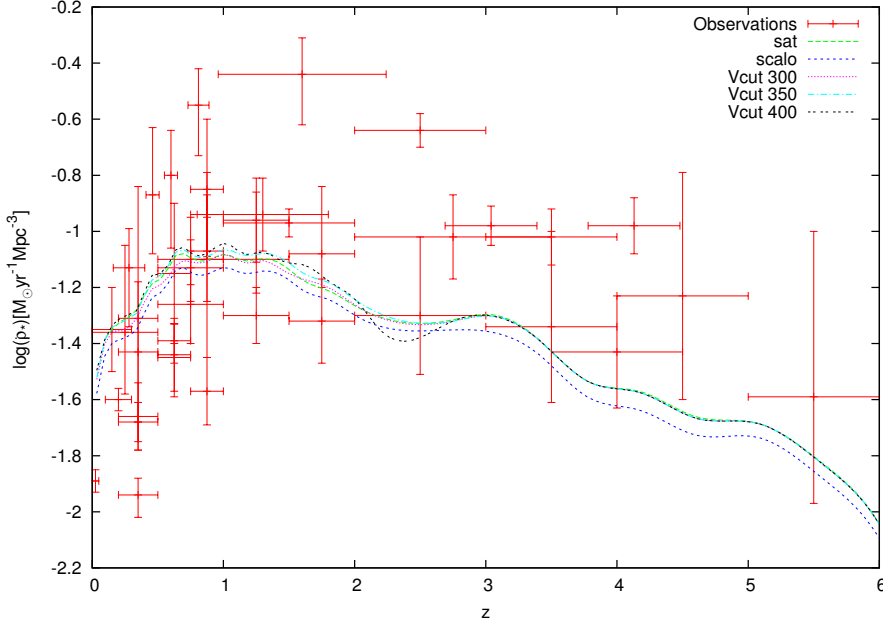


Figure 4.8: Global star formation history

using a SAM we can reproduce the cosmic star formation history of the universe, whose results are presented in figure 4.8. There we show results from observations compared with results from our model (table 4.2 shows the values and reports of such observations). In order to eliminate some resolution disadvantages we used the simulations SFOF and ZOOM mixed to build this curve. For $z \leq 2$ the graphic is built from results coming from the simulations SFOF, while for $z > 2$ the higher resolution of ZOOM simulations in those redshifts allows a best estimation of the SFR at that regime. Although we don't quantify this, in section 4.4 we give a brief discussion about this procedure.

General results

In this figure we can see how the Scalo IMF, according with all our previous comments is less efficient than Salpeter (almost with the parameters we used) to form stars along the entire domain, where the difference between both IMFs holds nearly constant along all the domain except for values of z near to zero, in which the curves try to converge to the same value. In terms of our results, although there is no strong difference between both curves ($\dot{\rho}_{*sal}/\dot{\rho}_{*sca} \sim 1.152$), the results associated with the IMF of Salpeter are in best agreement with observations than those for the Scalo, which underestimate the global star formation.

Note also how for $z > 2.8$ the curves for the global star formation associated to the three distinct models of star formation suppression and cooling by satellites (V_{cut} , and sat respectively) are quite coincident, in the case of the curves for every V_{cut}

the coincidence in the values is associated with the global threshold established by the resolution of the simulations and the mass of the halos at that redshift, which are well below the same global V_{cut} for every criterion. Which is interesting to note is that the model in which we allow gas cooling for galaxies with mass higher than M_{cut} have a similar behavior for that redshifts (although this simulations is running with the same parameters that $V_{cut}350$). This result indicates that for high redshift the enablement of cooling for satellites does not gives strong differences, while for $z > 2.8$ some subtle differences can be observed in the $\dot{\rho}_*$ for enabled/disabled cooling. Which is in agreement with the idea that the number of satellite galaxies increases with decreasing redshift (see the merger trees at the beginning of this chapter). Finally we can see that all curves converge at nearly the same value at $z = 0$ where $\dot{\rho}_*$ is a little bit higher for Salpeter than for Scalo.

Unfortunately, observational data has notably high uncertainties for redshift as many as for $\dot{\rho}_*$. Our results are in nearly good agreement with observational results for $z < 2$, nevertheless, although our results remain in the error bars of the observations, there is a noticeable failure of our model to reproduce in a better way the observations for $z > 2$. This sub-estimation in the global cosmic SFR for $z > 2$ could be associated with the resolution of the simulations. When simulations of higher resolution are used, more terms in the sum 4.16 can be included (more high redshift galaxies are identified and then a major contribution from low mass galaxies to the SFR can be observed) doing the curve moves upward, towards the region of the observational data.

It is clear, nevertheless that our model gives good approximations in the global behavior of the SFR, in the sense that we can see how the function behaves as a growing function for $0 < z < 1$. At $z \sim 1$ we can see how the star formation density reaches a maximum, even, a nearly constant value for $0.7 < z < 1.3$, and start to decrease at a more or less constant rate (in the logarithmic curve) which could suggest a power law behavior for $z > 2$.

Resolution effects

Like as been mentioned along all this work, resolution of simulations strongly affects the results we obtain for every physical quantity, then we briefly discuss here the effects of resolution in our results. How as been mentioned in chapter 3, the overmerging problem says that when resolution of simulations is not sufficiently high, structures formed will correspond to very macroscopic cosmological structures and any physical information related with substructures in these structures is lost by the low resolution of the simulations. This problem will affect notably our results, because the population of galaxies in to in a halo will depend of the resolution, then the contribution to the SFR from many galaxies is lost. This effect can be seen in figure ?? where we compare the global star formation history for two simulations of a cubic volume of side 100Mpc, one of one million particles, and the other corre-

Survey	z	$\log \dot{\rho}_*$
HDF (Pascarelle et al. 1998)	0.25 ± 0.25	$-1.36^{+0.31}_{-0.22}$
1500 Å	0.75 ± 0.25	$-1.26^{+0.23}_{-0.14}$
	1.25 ± 0.25	$-1.10^{+0.24}_{-0.12}$
	1.75 ± 0.25	$-1.08^{+0.24}_{-0.12}$
	2.50 ± 0.25	$-1.30^{+0.28}_{-0.21}$
	3.50 ± 0.25	$-1.34^{+0.34}_{-0.27}$
	4.50 ± 0.25	$-1.23^{+0.44}_{-0.37}$
	5.50 ± 0.25	$-1.59^{+0.59}_{-0.38}$
HDF (Madau et al. 1998)	2.75 ± 0.75	$-1.02^{+0.15}_{-0.15}$
1500 Å	4.00 ± 0.50	$-1.43^{+0.20}_{-0.20}$
(Steidel et al. 1999)	3.04 ± 0.35	$-0.89^{+0.07}_{-0.07}$
1700 Å	4.13 ± 0.35	$-0.98^{+0.10}_{-0.10}$
(Treyer et al. 1998) 2000 Å	0.15 ± 0.15	$-1.35^{+0.15}_{-0.15}$
CFRS (Lilly et al. 1999)	0.35 ± 0.15	$-1.68^{+0.07}_{-0.07}$
2800 Å	0.625 ± 0.125	$-1.39^{+0.08}_{-0.08}$
	0.875 ± 0.125	$-1.10^{+0.15}_{-0.15}$
HDF (Cowie et al. 1999)	0.35 ± 0.15	$-1.66^{+0.12}_{-0.12}$
2800 Å	0.625 ± 0.125	$-1.45^{+0.12}_{-0.12}$
	0.875 ± 0.125	$-1.57^{+0.12}_{-0.12}$
	1.25 ± 0.25	$-1.30^{+0.10}_{-0.10}$
HDF (Connolly et al. 1999)	0.75 ± 0.25	$-1.10^{+0.15}_{-0.15}$
2800 Å	1.25 ± 0.25	$-1.96^{+0.15}_{-0.15}$
	1.75 ± 0.25	$-1.32^{+0.15}_{-0.15}$
HDF (Sawicki et al. 1997)	0.35 ± 0.15	$-1.31^{+0.47}_{-0.47}$
3000 Å	0.75 ± 0.25	$-1.13^{+0.06}_{-0.06}$
	1.50 ± 0.50	$-0.97^{+0.05}_{-0.05}$
	2.50 ± 0.50	$-0.64^{+0.06}_{-0.06}$
	3.50 ± 0.50	$-1.02^{+0.10}_{-0.10}$
(Gallego et al. 1995) H $_{\alpha}$	0.025 ± 0.025	$-1.89^{+0.04}_{-0.04}$
CFRS (Tresse & Maddox 1998) H $_{\alpha}$	0.2 ± 0.1	$-1.6^{+0.04}_{-0.04}$
CFRS (Glazebrook et al. 1999) H $_{\alpha}$	0.875 ± 0.125	$-0.94^{+0.15}_{-0.15}$
CFRS (Hammer et al. 1999)	0.35 ± 0.15	$-1.94^{+0.06}_{-0.08}$
3727 Å	0.625 ± 0.125	$-1.44^{+0.11}_{-0.15}$
	0.875 ± 0.125	$-1.07^{+0.20}_{-0.38}$
CFRS (Flores et al. 1999)	0.35 ± 0.15	$-1.43^{+0.25}_{-0.25}$
15 μ m	0.625 ± 0.125	$-1.15^{+0.25}_{-0.25}$
	0.875 ± 0.125	$-0.85^{+0.25}_{-0.25}$
(Yan et al. 1999) H $_{\alpha}$	1.3 ± 0.5	$-0.94^{+0.13}_{-0.13}$
HDF (Hughes et al. 1998) 60 μ m	3.0 ± 1.0	-1.05
(Haarsma et al. 2000)	0.28 ± 0.12	$-1.13^{+0.14}_{-0.21}$
1.4GHz	0.46 ± 0.05	$-0.87^{+0.24}_{-0.21}$
	0.60 ± 0.05	$-0.80^{+0.16}_{-0.26}$
	0.81 ± 0.08	$-0.55^{+0.13}_{-0.18}$
	1.60 ± 0.64	$-0.44^{+0.13}_{-0.18}$

Table 4.2: Table of parameters and simulations in the study of the SFR

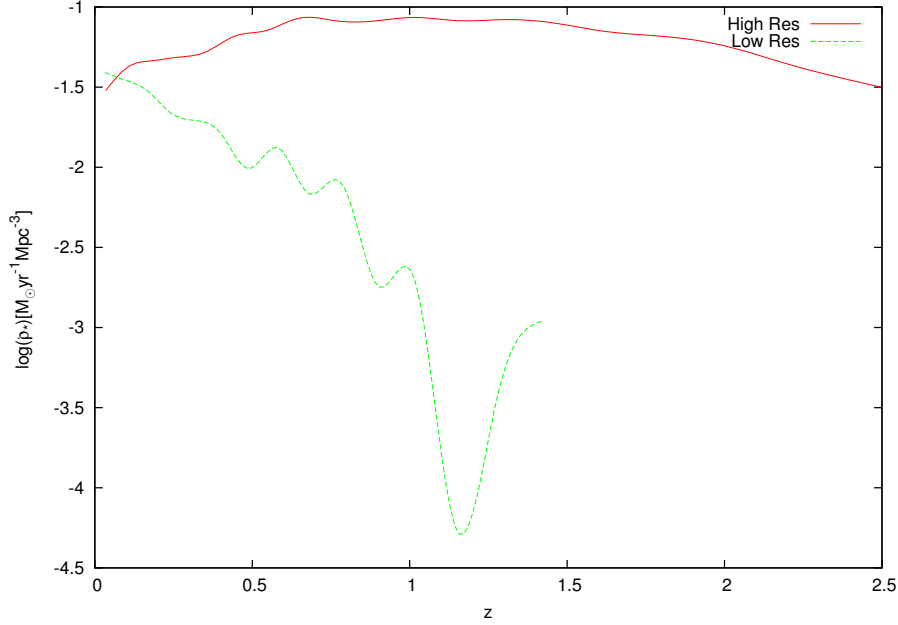


Figure 4.9: Resolution effects on the Global star formation history. This figure compares the global star formation for a SFOF05 simulations and an equivalent but of just one million particles. Note how the difference between results depends of redshift, and note how although the low resolution simulation is completely far away from the experimental data (which is traced most appropriately for SFOF05 line) the tendency to give the same value for $\dot{\rho}_*$ at $z = 0$ is notorious.

sponding to the SFOF05. In the simulation of one million particles the global star formation is completely underestimated because the lack of galaxies that contribute with its star formation to the sum of the global consolidated. While for the simulations SFOF05 the resolution allow the formation of many small structures, which will increase the number of galaxies and satellites in a snapshot, which will be more close to reality.

Figure 4.10 shows the comparison of the global star formation rate for two simulations of high and low resolution. The high resolution is a SFOF06 while the low resolution corresponds to a SFOF05. Note how the resolution of both simulations plays an important role in the increasing density of star formation at different redshifts, this increase is associated with the major number of galaxies that can form stars in the high resolution simulation which contribute to the global consolidated of star formation.

Very interesting is to observe that although there is a higher number of galaxies in the high resolution simulation, the star formation rate at $z \sim 0$ is inferior to those that for the low resolution simulation (which can be observed also in figure 4.9), and gives a best fit to the observational data for that redshifts. This decrease is related with a decreased star formation (for the simulation SFOF05) which can be observed in figure 4.7 as a decrease in the mass of newly formed stars for that redshifts, which

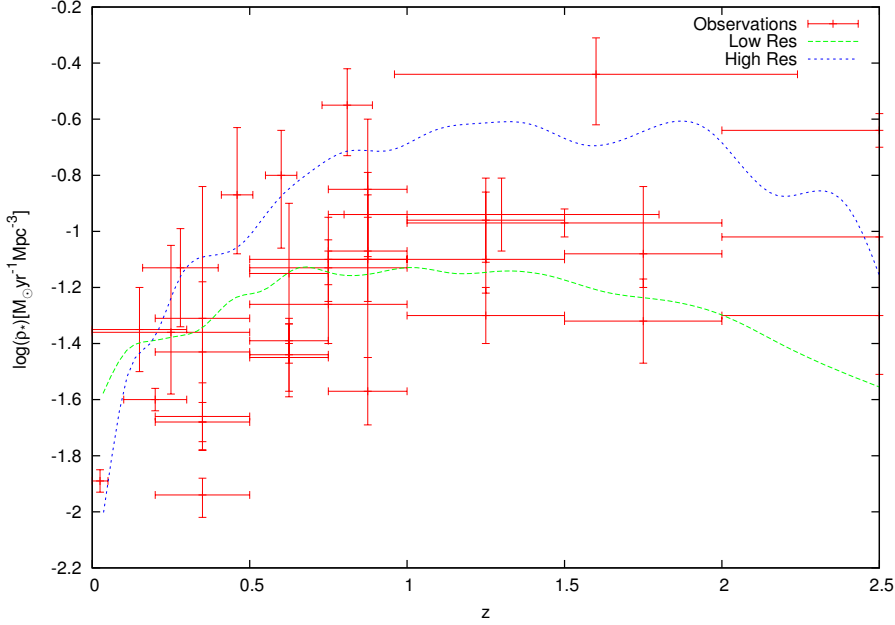


Figure 4.10: Resolution effects on the Global star formation history

could be justified in terms of the lack of cool gas in some galaxies that are not forming stars, and a suppression of the star formation in other massive galaxies according to the V_{cut} criterion, that is, halos become sufficiently massive that circular velocity exceeds the velocity threshold established to form stars in galaxies, that in this figure was of 350 km s^{-1} .

Figure shows the same effect when compared the simulations ZOOM01 and ZOOM02 (see table 3.1), there we can see that ZOOM1 is of higher resolution than ZOOM02. Note how the increased resolution helps to solve the overmerging at these redshifts, increasing the number of galaxies and therefore increasing the density of star formation, in that case, although the behavior of the curve still being decreasing, it passes through many data points giving a best fit to the experimental data.

Finally, figure 4.12 shows the comparison of both curves for the global star formation for the two resolutions we speak in the precedent paragraphs. Note how the resolution increased allows a best fit to the data, although produces a more pronounced peak for the SFR density at $z \sim 1$.

As mentioned in Ascasibar et al. 2002, one way to test the response of the simulations against resolution effects is to simulate different volumes at the same resolution, which could give insights about the response of cosmic variance to this kind of variations. As we don't realize this project, we match some of our findings with those described in its paper. We can see how the resolution increased simulations allow for a steeper curve for $z < 1$, as well as we can observe an increased SFR density for simulations of higher resolution, according to the overcooling problem (detection of

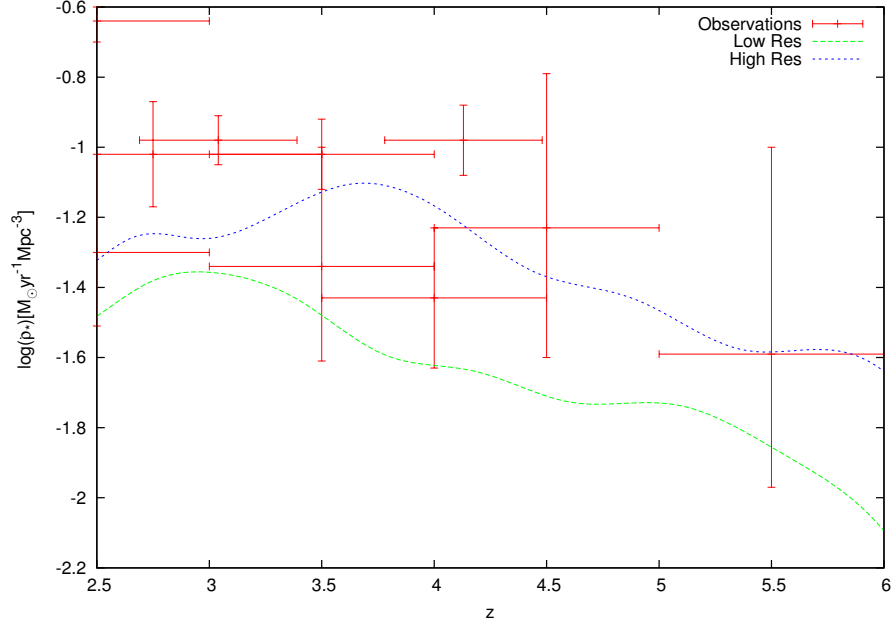


Figure 4.11: Resolution effects on the Global star formation history

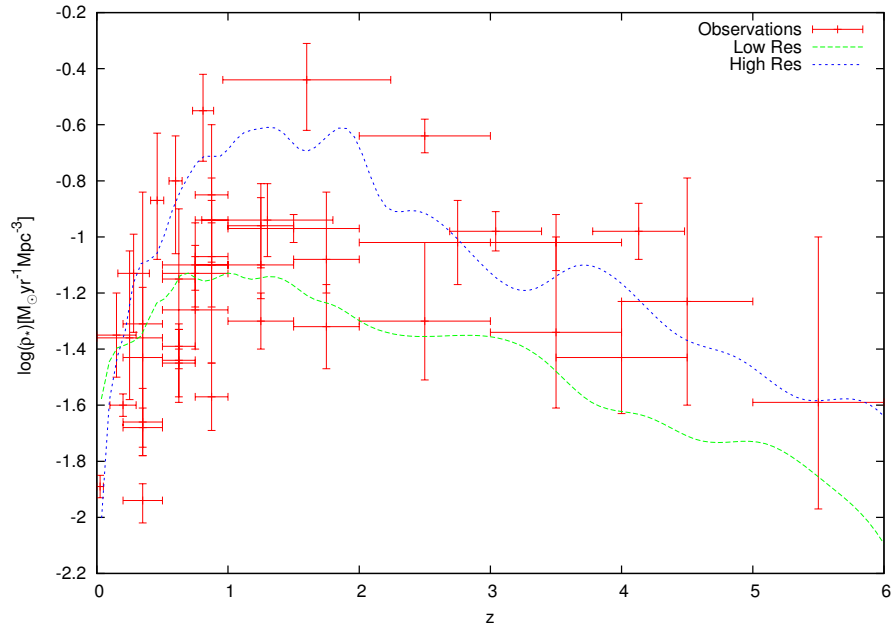


Figure 4.12: Resolution effects on the Global star formation history

more galaxies which contribute to the SFR density at higher resolutions).

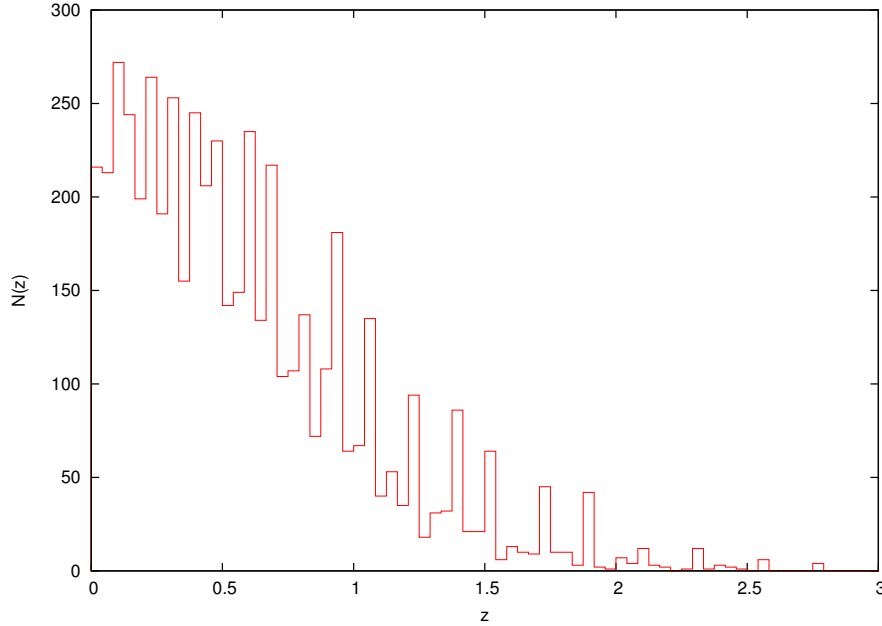


Figure 4.13: Frequency of mergers as a function of redshift

4.3.8 Mergers

Because the merger tree allow us to follow the evolution of the galaxies with redshift we explore this opportunity to study some general properties associated with mergers of galaxies. Remember that in our implementation two galaxies do not merge just at the instant in which the two halos associated are “merged” by the identification techniques in the merger tree. This situation marks the starting point for the merger, where the clocks counting the merger time computed as 4.10 are turned on and then the evolution of the merger is followed simultaneously with the evolution of every galaxy involved in that process.

Note that according to our implementation mergers could happen not just between two galaxies, there is an unlimited number of galaxies to be involved in such that process. Also note that when two galaxies merge, the properties of the most massive galaxy will drive the final remnant of the fusion, even, when two galaxies merge, there is a transfer of satellite galaxies from the merged galaxy (or the less massive) to the target galaxy, which allows a complex and semi hierarchical merger history.

According with the hierarchical Λ CDM cosmology, and in accordance with results of chapter 3, structures at recent ages of the universe where formed from the accretion of many early galaxies and proto galaxies, such that less massive structures form at first, and then mergers allow the formation of the larger ones. Then one expect that, according to the properties we observe in the halo mass distributions of section 3.3.4, the frequency of mergers decreases with increased redshift (given the less number of halos identified at higher redshift). Indeed, figure 4.13 show the frequency distribu-

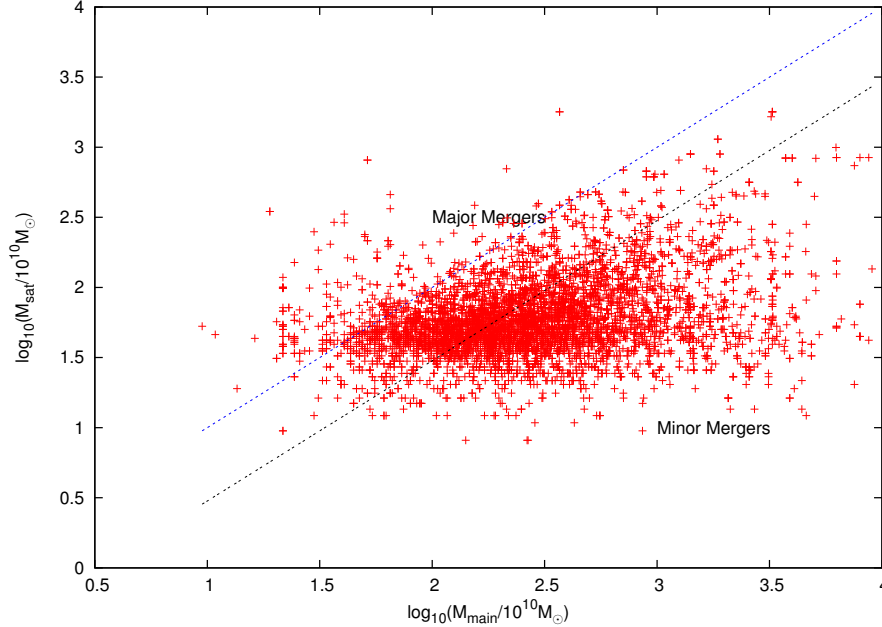


Figure 4.14: Masses of main and satellite galaxies involved in mergers. Blue line shows the line where equal mass merger are happening while black line marks the dividing line for major merger and minor merger regions.

tion of mergers as a function of redshift as obtained from the merger tree and the SAM. Note that clearly the distribution is in good agreement with the ideas we just mention. Note also that mergers do not start to happen at lower values of redshift (that is, at the first nodes of the merger tree) they start to happen time after the tree starts to be walked along its evolution, as mentioned in the precedent paragraph.

Figure 4.14 shows the distribution of masses for the satellite galaxies against the mass of the main galaxy, there we can see that the distribution is slightly oriented to the lower right side of the graph, which could implies a major frequency of minor mergers than major mergers. Diagonal blue line shows the region where equal mass mergers are happening, while the dashed black line marks the region of division between major and minor mergers. Region below this curve contain all points involved with minor mergers $M_{\text{sat}}/M_{\text{main}} \leq 0.3$, which are slightly more frequent than those for major mergers. Remember that we define major merger when $M_{\text{sat}}/M_{\text{main}} > 0.3$, that is, is refereed to mass ratio, not to mass content in to the galaxies, then a major merger could happen at high redshift when two small galaxies had a low mass but its mass ratio allow for the major merger classification.

Figure 4.15 confirms our comment, there we plot the mass ratio against the mass of the main galaxy (in logarithmic scales). Note that there is a nearly linear tendency in the distribution of points, and in fact, mostly the mergers are in the lower region of the curve, that is, they are minor mergers, although mentioned before, this density of minor mergers could be affected by the resolution of the simulations.

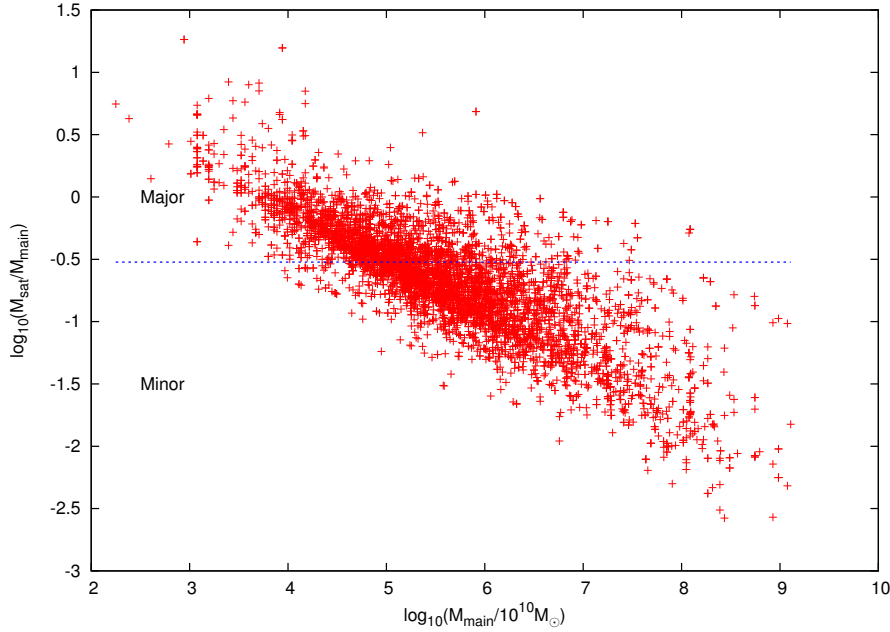


Figure 4.15: $M_{\text{sat}}/M_{\text{main}}$ ratio in galaxy mergers

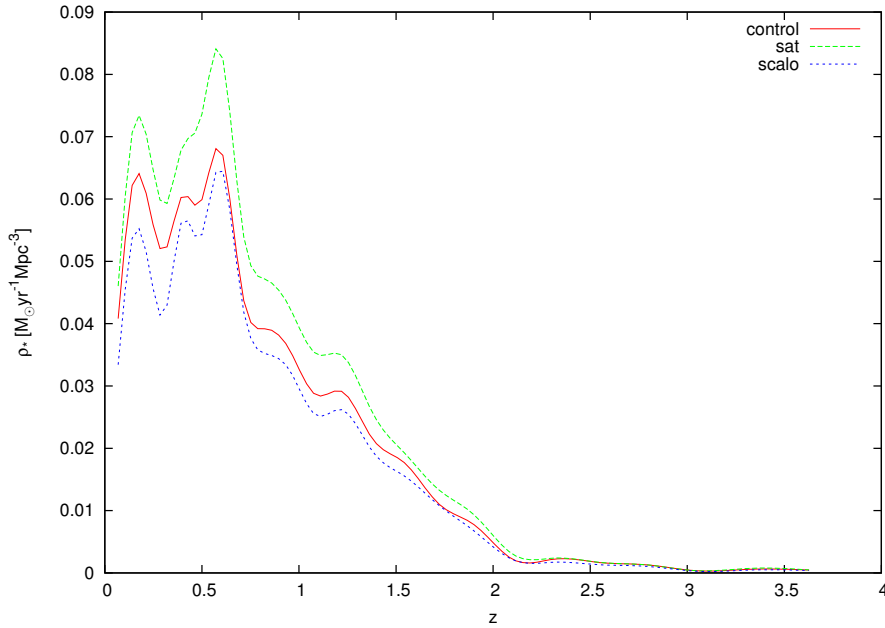


Figure 4.16: Global Star formation bursts at major mergers for three distinct parameter set

Finally, it has been discovered that major mergers drive to strong bursts of star formation, in which mostly all cold gas mass in galaxies merging is burned at time scales of 10^8yr , producing stars with a constant star formation rate. Then, in our implementation when a major merger event happens, all cold gas mass is burned to form stars instantly (note that the time scale of this burst is too small compared

with time between snapshots and comparable to a time steps of integration used to solve the gas equations which is of the order 10^8yr).

Figure 4.16 shows the global SFR associated to star formation bursts induced by major mergers of galaxies. As for the figures before, the curve associated with the cooling enabled for satellite more massive than M_{cut} (whose evolution is computed with parameters for a Salpeter IMF) shows a more efficient bursts of star formation than that one shown for the model in which cooling for satellites is disabled. There we must be careful with the interpretation of the SFR bursts. These bursts are computed independently (parametrically) of the IMFs, but how has been shown, the evolution with the Salpeter IMF allows a higher global content of cold gas mass, allowing more violent bursts of star formation once mergers happens.

4.4 Conclusions

We presented the implementation of a semi analytic model SAM to model galaxy formation in cosmological Nbody simulations. Our simulations are according to the Λ CDM concordance cosmology and where ran using Gadget2 code.

We introduced variations in the models in different ways, we change the maximum circular velocity of the halos for which star formation is enabled V_{cut} at three distinct values 300, 350 and 400 kms^{-1} . Also we introduce a novel criterion to enable/disable cooling of hot gas in satellite galaxies through a mass criterion, instead to disable it in an absolute way for any satellite galaxy, we chose to hold cooling happening in satellite galaxies massive than M_{cut} , where we used M_{cut} as two times the mass of the smallest structure (or substructure) identified in the entire simulation. All these simulations used parameters associated with the Salpeter's IMF. Finally, as a comparison, we introduce a last model, which the standard cooling for satellites and $V_{\text{cut}} = 350\text{kms}^{-1}$ but with parameters associated with the Scalo's IMF.

Our results in describe the evolution of baryonic mass in galaxies according to our prescription makes sense with one expectation and observations. Our model describes the evolution of global quantities as cold gas mass, cooling function, hot gas mass, stellar mass and reheated gas by supernovae feedback.

From the analysis of figures we can see noticeable differences between the quantities related with the Salpeter and Scalo IMF and according to our results associated with the global star formation we see that the Salpeter IMF gives more appropriated results in to the description of the global star formation.

Also we can see that of the three models we ran with variations in the V_{cut} criterion, that one associated with $V_{\text{cut}} = 400\text{kms}^{-1}$ is completely different from results we obtain for the other two choices. Also, from the behavior of the cooling rate we see that another possible choice for the maximum circular velocity could be $V_{\text{cut}} = 300\text{kms}^{-1}$,

given the comparable behavior this offers when compared with that curves related to $V_{cut} = 350 \text{ km s}^{-1}$.

Finally we can see in all figures, that the criterion to enable cooling of hot gas in satellite galaxies according to its mass offers results very compatibles with those related with the older criterion of totally disabled cooling for satellites. Nevertheless from results for SFR density, we could prefer to use this criterion in posterior simulations, because it could give a closer description to the physical process happening in satellite galaxies.

Our results model star formation in good agreement for $z < 2$ for median resolution, but for a high resolution, our model fits quite well with observations. This is another verification to the Λ CDM cosmological model, and qualifies the methods and approximations used in our semi analytic model as a good approximation in the description of galaxy formation. Also, as mentioned before, the observational data of global star formation is best described by parameters according with the Salpeter's IMF.

Our results has been tested against resolution, we saw in figures in section how the resolution of the simulations manifested as overmerging and overcooling affects the determination of the global star formation. We see how the SFR density changes at high z values with the resolution of the simulations, but more interestingly, we saw how all models, at low and high resolution tries to converge to the same value of $\dot{\rho}_*$ at $z = 0$. It suggest that a best estimation and parametrization of the global SFR as a function of redshift must be done using very high resolution simulations in order to avoid any misleading related with the matching of observations at low and median redshift.

Bibliography

- [1] Ascasibar, Y., Yepes, G., Gottlöber, S., Muller, V. 2002, APP, 387, 396
- [2] Avila-Reese, V. 2006, ArXiv Astrophysics e-prints, arXiv:astro-ph/0605212
- [3] Bagla, J. S. 2002, Journal of Astrophysics and Astronomy, 23, 185
- [4] Bett, P., Eke, V., Frenk, C. S., Jenkins, A., Helly, J., & Navarro, J. 2007, MNRAS, 376, 215
- [5] Binney, J., Tremaine, S., Galactic Dynamics, 1988, Princeton University Press.
- [6] Binney, J., Merrifield, J., Galactic Astronomy, 1997, Princeton University Press.
- [7] Bruzual, G., & Charlot, S. 2003, MNRAS, 344, 1000
- [8] Cole, S., Aragon-Salamanca, A., Frenk, C. S., Navarro, J. F., & Zepf, S. E. 1994, MNRAS, 271, 781
- [9] Cowan G., Statistical Data Analysis, 1998, Oxford Science Publications.
- [10] Crain, R. A., Eke, V. R., Frenk, C. S., Jenkins, A., McCarthy, I. G., Navarro, J. F., & Pearce, F. R. 2007, MNRAS, 377, 41
- [11] De Lucia, G., Kauffmann, G., Springel, V., White, S. D. M., Lanzoni, B., Stoehr, F., Tormen, G., & Yoshida, N. 2004, MNRAS, 348, 333
- [12] Diaferio, A., Kauffmann, G., Colberg, J. M., & White, S. D. M. 1999, MNRAS, 307, 537
- [13] Frenk, C. S., et al. 1999, ApJ, 525, 554
- [14] Gao, L., Springel, V., & White, S. D. M. 2005, MNRAS, 363, L66
- [15] Gill, S. P. D., Knebe, A., & Gibson, B. K. 2004, MNRAS, 351, 399
- [16] Hetzner, H., & Burkert, A. 2006, MNRAS, 370, 1905
- [17] Hatton, S., Devriendt, J. E. G., Ninin, S., Bouchet, F. R., Guiderdoni, B., & Vibert, D. 2003, MNRAS, 343, 75

- [18] Kang, X., Jing, Y. P., Mo, H. J., Bolrner, G. 2005, ApJ, 631, 21
- [19] Klypin, A. 2000, ArXiv Astrophysics e-prints, arXiv:astro-ph/0005502
- [20] Longair, M. S., Galaxy Formation, 2000, Springer-Verlag
- [21] Liddle, A., An Introduction to Modern Cosmology, 1998, John Wiley & Sons.
- [22] Nagashima, M., Yahagi, H., Enoki, M., Yoshii, Y., & Gouda, N. 2005, ApJ, 634, 26
- [23] Neyrinck, M. C., Gnedin, N. Y., & Hamilton, A. J. S. 2005, MNRAS, 356, 1222
- [24] Padmadabhan, T., 2002, Theoretical Astrophysics: Galaxies and Cosmology, Cambridge University Press
- [25] Sirko, E. 2005, ApJ, 634, 728
- [26] Spergel, D. N., et al. 2007, ApJs, 170, 377
- [27] Shaw, L. D., Weller, J., Ostriker, J. P., & Bode, P. 2006, ApJ, 646, 815
- [28] Springel, V., White, S. D. M., Tormen, G., & Kauffmann, G. 2001, MNRAS, 328, 726
- [29] Springel, V., Frenk, C. S., & White, S. D. M. 2006, Nat, 440, 1137
- [30] Springel, V., et al. 2005, Nat, 435, 629
- [31] Springel, V. 2005, MNRAS, 364, 1105
- [32] Yoshida, N., Springel, V., White, S. D. M., & Tormen, G. 2000, ApJl, 544, L87
- [33] Wall, J. V., Jenkins, C. R., 2003, Practical Statistics For Astronomers, Cambridge University Press